Modifications of graphene nanosheets to utilize as photocatalyst

By

Zameela Yousaf

(79-FBAS/PHDPHY/F16)

Department of physics

Faculty of basic and applied sciences,

International Islamic University,

Islamabad

(2022)

Optical properties

Nanosheets

Photocatalyst

Modifications of graphene nanosheets to utilize as photocatalyst

By

Zameela Yousaf
(79-FBAS/PHDPHY/F16)

Supervisor

Dr. Shamaila Sajjad (IIUI)

A thesis is submitted for degree of Doctor of Philosophy

Dated: 31-08-2022

FINAL APPROVAL

It is certified that the work presented in this thesis entitled 'Modifications of graphene nanosheets to utilize as photocatalyst' by **Ms. Zameela Yousaf** bearing **Registration No. 79-FBAS/PHDPHY/F16** is of sufficient standard in scope and quality for the award of degree of PhD from International Islamic University, Islamabad.

COMMITTEE

External Examiner 1
Dr.Zafar Iqbal
Professor,
Riphah International University

External Examiner 2
Dr. Qurat ul Ain
Assistant Professor
NUST

Quratulain

Internal Examiner
Dr. Imran Murtaza
Associate Professor
Department of Physics, FBAS, IIUI

DR. IMRAN MURTAZA
Associate Professor
Department of Phy[illegible]
International Islamic University
Islamabad [illegible]

Supervisor
Dr. Shamaila Sajjad
Associate Professor
[illegible], FBAS, IIUI

Dr. Shamaila Sajjad
Associate Professor
Department of Physics, FBAS, IIUI

Chairperson
Dr. Shaista Shahzada
Associate Professor
Department of Physics, FBAS, IIUI

Dr. Shaista Shahzada
Chairperson
Department of Physics
Faculty of Basic and Applied Sciences
International Islamic University
Islamabad

Modifications of graphene nanosheets to utilize as photocatalyst

By

Zameela Yousaf

(Registration No. 79-FBAS/PHDPHY/F16)

A thesis submitted to

Department of physics

For the award of the degree of

Ph.D physics

Dr. Shaista Shahzada
Chairperson
Department of Physics
Faculty of Basic and Applied Sciences
International Islamic University
Islamabad

Signature: ______________________

(Chairman, Department of Physics)

Signature: ______________________

(Dean FBAS, IIU, Islamabad)

Department of physics

Faculty of basic and applied sciences,

International Islamic University,

Islamabad

(2022)

A thesis submitted to

Department of Physics

International Islamic University Islamabad

As a partial fulfilment for the award of the degree of

Doctor of Philosophy

Certificate

It is certificated that Ms. Zameela Yousaf (Registration No.79-FBAS/PHDPHY/F16) has carried out the research work related to this thesis having title **"Modifiations of graphene nanosheets to utilize as photocatalyst"** under my supervision. Most of experimental work was carried out in Nano photocatalysis laboratory of interntional Islamic University Islamabad (IIUI), Pakistan Atomic Energy Comission (PAEC). It is certificated that chapter No. 4-6 of present work are based on Ms. Zameela Yousaf's researh conttributions and have been published in international journals. The present work fulfills all the reuirments for the award of degree of dotor of philosophy.

Supervisor

Dr. Shamaila Sajjad
Associate Prof.
Department of

Dr. Shamaila Sajjad (IIUI)

Associate professor (TTS)

CIRBS

International Islamic University, Islamabad.

Declaration

I hereby declare that this thesis work 'Modifiations of graphene nanosheets to utilize as photocatalyst' neither as a whole nor a part of it has been copied out from any source. Further work presented in this dissertation has not been submitted in support of any application for any other degree or qualification to any other university or institute and is considerable under the plagiarism rules of Higher Education Commission (HEC). It is affirmed that Chapter No.4-6 of present work are based on my own research contributions and Chapter No. 4 and chapter No. 5 have been published in international journals. The plagiarism test was done by using Turnitin via ID: 1749124695 and similarity index is found that lies in accepted range allowed by Higher Education Commission (HEC) Pakistan.

Zameela Yousaf

(79-FBAS/PHDPHY/F16)

DEDICATED

To

My Parents, Brothers

&

Sister

Acknowledgement

First, I would like to thank the most gracious, Almighty Allah, for giving me strength and determination to carry my research work. He bestowed me with wellness, understanding and persistence to accomplish this thesis. Alhamdulillah!

I would like to thank and express my deep and sincere gratitude to my motivational supervisor **Dr. Shamaila Sajjad** (Associate professor, Department of Physics, IIUI) for their patience, support, immense knowledge, guidance, and· encouragement. Her doors were always open for worthy discussions and suggestions during whole research. Her benevolence will be ever appreciated.

I would also like to thank my Lab fellows at IIUI **Anum Iqbal, Maria, Yumna, Aatika, Saima Noor, and Ayesha Kanwal** for their continuous support. I would also like to thank my colleagues for encouraging me. My research is really the fruit of my sincere family members, parents, and respected teachers.

It fills my heart with joy unspeakable to express my gratitude to everybody who contributed to the successful accomplishment of my PhD thesis.

List of Publications

1. **Yousaf, Z.**, Sajjad, S., Leghari, S. A. K., Noor, S., Kanwal, A., Bhatti, S. H., ... & ElBahy, Z. M. (2021). Influence of integrated nitrogen functionalities in nitrogen doped graphene modified WO3 functional visible photocatalyst. *Journal of Environmental Chemical Engineering*, 106746. **(IF.7.96)**
2. **Yousaf, Z.**, Sajjad, S., Leghari, S. A. K., Mehboob, M., Kanwal, A., & Uzair, B. (2020). Interfacial charge transfer via 2D-NiO and 2D-graphene nanosheets combination for significant visible photocatalysis. *Journal of Solid-State Chemistry*, *291*, 121606. **(IF.3.498)**
3. Kanwal, A., Sajjad, S., Leghari, S. A. K., & **Yousaf, Z.** (2021). Cascade electron transfer in ternary CuO/α-Fe2O3/γ-Al2O3 nanocomposite as an effective visible photocatalyst. *Journal of Physics and Chemistry of Solids*, *151*, 109899. **(IF: 3.99)**
4. Naz, Y., Sajjad, S., Leghari, S. A. K., Masood, M., Malik, A., **Yousaf, Z.**, & Uzair, B. (2020). Development of eco-friendly green and chemical routes for exfoliation of graphite as effective antibacterial agent. *Materials Research Express*, *6*(12), 125620. **(IF: 1.6)**

Research papers under process

1. Carbon qauantum dots modified 2D/2D MgO@G nanocomposites as an visible photocatalyst.

Journal of [illegible] Environmental Chemical Engineering [illegible] (202[illegible]) [illegible]

Contents lists available at ScienceDirect

Journal of Environmental Chemical Engineering

journal homepage: www.elsevier.com/locate/jece

Influence of integrated nitrogen functionalities in nitrogen doped graphene modified WO_3 functional visible photocatalyst

Zameela Yousaf, Shamaila Sajjad, Sajjad Ahmed Khan Leghari, Saima Noor, Aisha Kanwal, Sajjad Hussain Bhatti, Khaled H. Mahmoud, Zeinhom M. El-Bahy

International Islamic University, H-10, Islamabad, Pakistan
NPU-NCP Joint International Research Centre on Advanced Nanomaterials and Defects Engineering, Northwestern Polytechnic University, China
Pakistan Institute of Engineering and Applied Sciences, Islamabad, Pakistan
Department of Physics, Quaid-e-Azam University, Islamabad, Pakistan
Department of Physics, College of Khurma University College, Taif University, P.O. Box 11099, Taif 21944, Saudi Arabia
Department of Chemistry, Faculty of Science, AL Azhar University, Nasr City, 11884 Cairo, Egypt

ARTICLE INFO

Editor: Dr. G.L. Dotto

Keywords:
Nitrogen doped graphene
2,4-dichlorophenol
WO_3
Methyl orange
Heterogeneous photocatalysis

ABSTRACT

Nitrogen doped graphene modified WO_3 nanocomposites were synthesized through an effective methodology. The prepared photocatalysts were employed as active candidates for degradation of highly toxic organics i.e., 2, 4 dichloro phenol (2, 4-DCP) and methyl orange (MO). XRD profile of N-graphene showed complete reduction of GO into N-graphene. All diffraction peaks of WO_3 along with N-graphene indicated monoclinic phase of WO_3. SEM and TEM images of 3.0% N-graphene/WO_3 have demonstrated the mixed morphology of irregular massive rod like blocks and round shaped particles of WO_3 distributed on cracked sheets of N-graphene. Nitrogen defects in graphene altered zero band gap semi-metallic graphene to semiconducting material and increased the absorption edge of N-graphene/WO_3 nanocomposites towards visible region as studied in DRS analysis. FTIR and Raman studies showed the strong connection between N-graphene and WO_3 by making W – O – C surface linkage. The noticeable reduction in PL emission peaks of 3.0% N-graphene/WO_3 indicated obvious separation of photo induced charge carriers. The study of radical scavengers suggested that holes (h^+) and •OH are the main elements for the decontamination of both MO and 2, 4-DCP. XPS analysis shows all possible C – N bonding configurations in 3.0% N-graphene/WO_3. 3.0% N-graphene/WO_3 composite showed the maximum photo degradation of MO (~ 94.0%) and 2, 4-DCP (~ 81.0%). The synergism between N-graphene and WO_3 results into more spotty sites on catalyst and restoring of sp^2 structural defects in N-graphene lattice improve the transportation of charge carriers during photocatalysis. This work provides innovative strategies for designing the N-graphene/semiconductor nanosystems with enhanced photocatalytic phenomena in the environmental cleanup remedies.

1. Introduction

Semiconductor based photocatalysts have gained much attraction on account of high energy demand and rising environmental problems [1]. Past few years, numerous semiconductors such as oxynitride, sulfides and metal oxides have been fabricated to derive their photocatalytic response under visible light [illegible]. However, fast recombination rate of photogenerated charge carriers and low usage of visible light limits their application towards environmental remediation [illegible]. Subsequently, visible light responsive photocatalytic materials have been fabricated to tackle the challenges regarding energy production and environmental contamination. Among all of them, WO_3 (n-type semiconductor) is considered a potential material owing to their tunable optical and electronic properties. WO_3 has been attained intrigued attention in photocatalytic applications due to long term stable physiochemical properties, photocorrosion and visible light absorption resilience [illegible]. Unfortunately, high rate of recombination process of photo induced charge-carriers and agitation in oxygen reduction on account of narrow band gap and low-potential respectively makes WO_3 less effective in photocatalysis [8].

To overcome these issues, many techniques have been applied to boost the photocatalytic activities of WO_3 through incorporation of

---

* Correspondence to: Faculty of Basic and Applied Sciences, International Islamic University, H-10, Islamabad 44000, Pakistan.
E-mail addresses: [illegible] (S. Sajjad).

[illegible]
Received 11 July 2021; Received in revised form 31 October 2021; Accepted 3 November 2021

Journal of Solid State Chemistry 291 (2020) [illegible]

Contents lists available at ScienceDirect

Journal of Solid State Chemistry

journal homepage: www.elsevier.com/locate/jssc

Interfacial charge transfer via 2D-NiO and 2D-graphene nanosheets combination for significant visible photocatalysis

Zameela Yousaf [a], Shamaila Sajjad [a,*], Sajjad Ahmed Khan Leghari [b], Maria Mehboob [a], Aisha Kanwal [a], Bushra Uzair [a]

[a] International Islamic University, H-10, Islamabad, Pakistan
[b] Pakistan Institute of Engineering and Applied Sciences, Islamabad, Pakistan

ARTICLE INFO

Handling Editor: Qichun Zhang

Keywords:
NiO nanosheets
Graphene
2D materials
Interfacial charge
2D-2D interaction
Photocatalysis

ABSTRACT

Two dimensional (2D) heterostructures in combination with other 2D materials play a vital role to boost photocatalytic efficiency owing to increase in interfacial charge separation/transferring rate. Graphene modified NiO 2D-2D nanocomposites were prepared via wet impregnation method and confirmed by various spectroscopic and analytical techniques. XRD patterns of pure and composites confirmed the characteristic peaks of NiO and graphene. NiO nanosheets are uniformly dispersed on graphene sheets which facilitate interfacial coupling between them as observed in SEM images. UV–Vis spectra of composite showed band gap reduction from 3.3 to 2.3 eV owing to incorporation of graphene sheets. Further, suppression of charge carriers was confirmed by photoluminescence spectra. Consequently, 10.0% graphene/NiO composite exhibits increased photocatalytic activity towards MO degradation under visible light due to strong interfacial coupling and 2D-2D surface morphologies of photocatalysts which are beneficial to suppress the charge recombination and provide massive reactive sites.

1. Introduction

Environmental technology and science are facing some serious issues based on increasing water and air pollution [1]. A large amount of pollutants (heavy metals, dyes etc.) is produced due to industrial effluent which intensely effect environmental and aquatic life while their hostile effect depends on their complex molecular structure [2,3]. It is crucial to develop an effective technique to tackle these intricate environmental problems. Photocatalytic degradation is most efficient technique to deal with environmental challenges (to eradicate the hazardous contaminations from environment) and sustainability with light irradiation [4,5]. In photocatalytic process, excited electrons move from valence to conduction band of semiconductor materials to generate electron (e^-)–hole (h^+) pairs under light irradiation. These photoexcited charge carriers are responsible for oxidation reduction process with oxygen and water to degrade the organic pollutants and subsequently mineralize it to CO_2 and H_2O [illegible].

2D nanomaterials have been gaining tremendous attention in environmental remediation owing to their fascinating physiochemical properties like mechanical flexibility, large specific surface area and numerous active sites on their surface etc. [8,9]. Among various 2D materials, NiO (P-type semiconductor) possesses excellent conductance feature, low cost, elevated chemical and long-term catalytic stability which make it appropriate as photocatalyst under visible light irradiation [10,11]. However, quick recombination of charge carriers, minimum harvesting of light, less selective absorption etc. are the considerable major limitations of NiO semiconductor to impend photocatalytic performance [12]. To overcome these obstacles, literature have shown that 2D-2D heterostructures endow electronic coupling and enhanced interfacial contact area between them. Thus, physical and electronic coupling effect between semiconductor sheets and graphene is favorable to increase the transportation rate of electron/hole pairs and boost the photocatalytic efficiency [13–15]. Because highly conductive graphene sheet acts as an electron acceptor for shuttling electrons due to delocalized electronic network over the carbon sheets, leading to an effective charge separation rate at junction interface [16]. Recently, Sun et al. demonstrated that fabrication of 2D-2D $BiVO_4$/reduced graphene sheets via solvothermal method exhibited high photocatalytic efficiency as compared to 1D-2D and 0D-2D heterojunctions. The results clearly indicates the fast electrons shuttling in 2D-2D $BiVO_4$/reduced graphene sheets at interfacial junction, leading to augment the separation rate of charge carriers and enhance photocatalytic efficiency [17]. Therefore,

---

* Corresponding author. Faculty of Basic and Applied Sciences, International Islamic University, Islamabad, 44000, Pakistan.
E-mail addresses: [illegible] (S. Sajjad).

https://doi.org/10.1016/j.jssc.2020.[illegible]
Received 2 June 2020; Received in revised form 16 July 2020; Accepted 22 July 2020

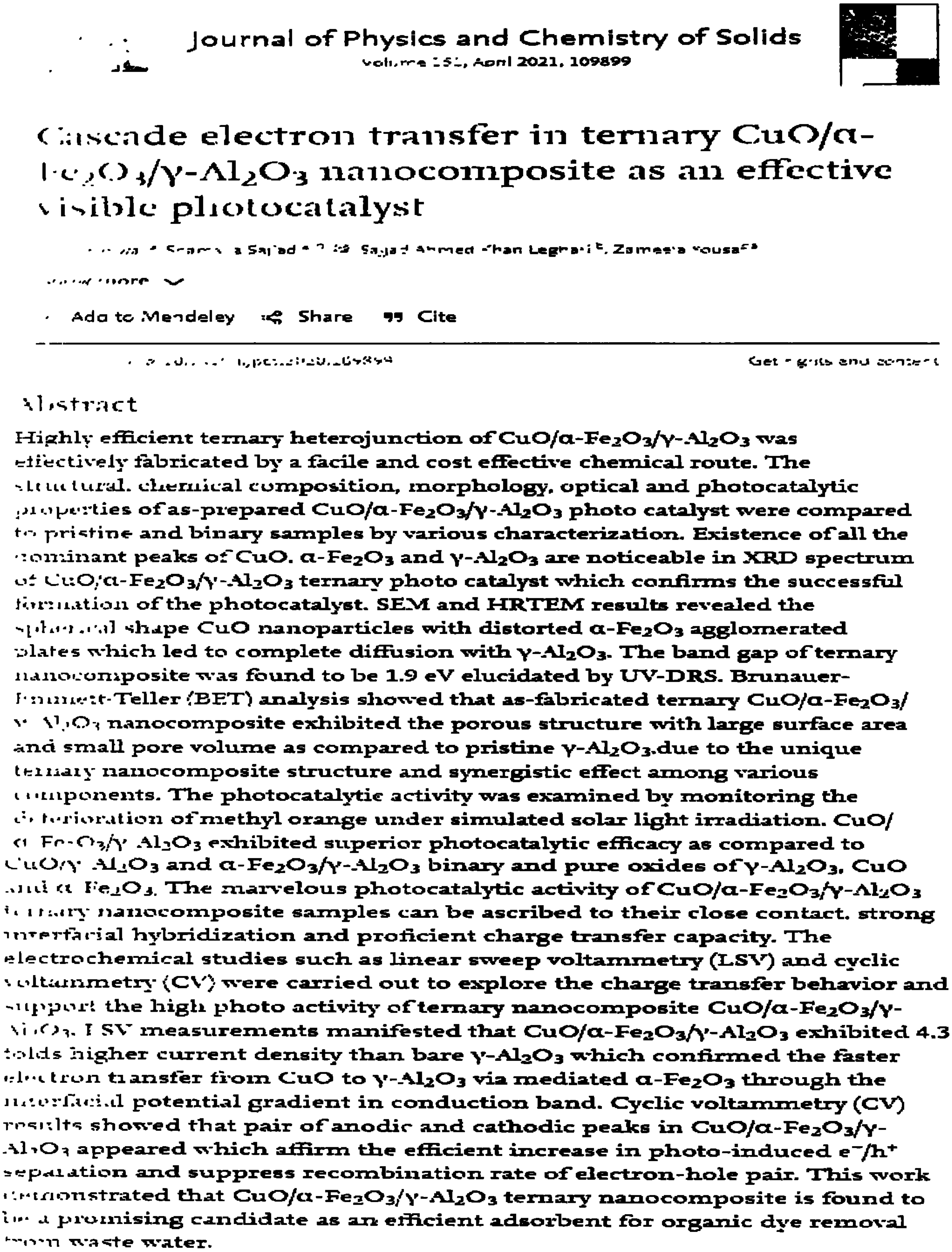

Journal of Physics and Chemistry of Solids
Volume 15[illegible], April 2021, 109899

Cascade electron transfer in ternary CuO/α-Fe_2O_3/γ-Al_2O_3 nanocomposite as an effective visible photocatalyst

[illegible] Shamsa Sajjad, Sajjad Ahmed Khan Leghari, Zameera Yousaf

[illegible]

Abstract

Highly efficient ternary heterojunction of CuO/α-Fe_2O_3/γ-Al_2O_3 was effectively fabricated by a facile and cost effective chemical route. The structural, chemical composition, morphology, optical and photocatalytic properties of as-prepared CuO/α-Fe_2O_3/γ-Al_2O_3 photo catalyst were compared to pristine and binary samples by various characterization. Existence of all the dominant peaks of CuO, α-Fe_2O_3 and γ-Al_2O_3 are noticeable in XRD spectrum of CuO/α-Fe_2O_3/γ-Al_2O_3 ternary photo catalyst which confirms the successful formation of the photocatalyst. SEM and HRTEM results revealed the spherical shape CuO nanoparticles with distorted α-Fe_2O_3 agglomerated plates which led to complete diffusion with γ-Al_2O_3. The band gap of ternary nanocomposite was found to be 1.9 eV elucidated by UV-DRS. Brunauer-Emmett-Teller (BET) analysis showed that as-fabricated ternary CuO/α-Fe_2O_3/γ-Al_2O_3 nanocomposite exhibited the porous structure with large surface area and small pore volume as compared to pristine γ-Al_2O_3.due to the unique ternary nanocomposite structure and synergistic effect among various components. The photocatalytic activity was examined by monitoring the deterioration of methyl orange under simulated solar light irradiation. CuO/α-Fe_2O_3/γ-Al_2O_3 exhibited superior photocatalytic efficacy as compared to CuO/γ-Al_2O_3 and α-Fe_2O_3/γ-Al_2O_3 binary and pure oxides of γ-Al_2O_3, CuO and α-Fe_2O_3. The marvelous photocatalytic activity of CuO/α-Fe_2O_3/γ-Al_2O_3 ternary nanocomposite samples can be ascribed to their close contact, strong interfacial hybridization and proficient charge transfer capacity. The electrochemical studies such as linear sweep voltammetry (LSV) and cyclic voltammetry (CV) were carried out to explore the charge transfer behavior and support the high photo activity of ternary nanocomposite CuO/α-Fe_2O_3/γ-Al_2O_3. LSV measurements manifested that CuO/α-Fe_2O_3/γ-Al_2O_3 exhibited 4.3 folds higher current density than bare γ-Al_2O_3 which confirmed the faster electron transfer from CuO to γ-Al_2O_3 via mediated α-Fe_2O_3 through the interfacial potential gradient in conduction band. Cyclic voltammetry (CV) results showed that pair of anodic and cathodic peaks in CuO/α-Fe_2O_3/γ-Al_2O_3 appeared which affirm the efficient increase in photo-induced e^-/h^+ separation and suppress recombination rate of electron-hole pair. This work demonstrated that CuO/α-Fe_2O_3/γ-Al_2O_3 ternary nanocomposite is found to be a promising candidate as an efficient adsorbent for organic dye removal from waste water.

Materials Research Express

PAPER

Development of eco-friendly green and chemical routes for exfoliation of graphite as effective antibacterial agent

Youmna Naz[1], Shamaila Sajjad[1], Sajjad Ahmed Khan Leghari[2], Maria Masood[1], Attika Malik[1],
Zaneela Yousaf[1] and Bushra Uzair[1]

Published 9 January 2020 • © 2020 IOP Publishing Ltd
Materials Research Express, Volume 6, Number 12
Citation Youmna Naz *et al* 2019 *Mater. Res. Express* **6** 125620

Abstract

Liquid phase exfoliation (LPE) has emerged as an effective technique for producing large scale 2D nano-sheets. In present study, graphite has been exfoliated by using chemical and green routes. The adopted methods are cost effective, eco-friendly, time saving and utilize less toxic solvents for producing high quality exfoliated graphite (EG). Herein, graphite exfoliation has been achieved by using NaOH, HCl, natural acids (lemon juice) and plant extract (mint extract). In chemical route, exfoliation of graphite using NaOH has given excellent results as compared to HCl. By using NaOH, d-spacing value has been increased from 3.30 to 3.37 nm and sheets with average thickness of 14.8 nm have been achieved. In green route, mint extract gives better result as compared to lemon juice. The bioactive constituents of plant extracts penetrate between graphitic layers results in weakening of van der waals forces which facilitates exfoliation. Using mint extract, d-spacing value has been increased from 3.30 to 3.36 nm. Thin sheets with average thickness of 10.79 nm has been obtained. Overall exfoliation using NaOH and mint extract gives excellent result. The higher I_D/I_G ratio for exfoliated graphite using NaOH and mint extract is 0.77 and 0.88, respectively as compared to pure graphite which confirmed the degree of exfoliation. Exfoliation of graphite enhances the surface properties of nano-sheets leading to the enhanced antibacterial activity against Pseudomonas Aeruginosa as compared to pure graphite. The exfoliated graphite using mint extract showed the best antibacterial activity.

Abstract

Environmental pollution and energy crises are the main contests in worldwide. Over a past decade, the development in natural abundant, cost effective and more efficient material has made them as competent candidate for versatile applications.

In this research work, high-quality graphene with controllable layers and 2D semiconductors materials have been fabricated via chemical synthetic routes. The graphene based modified semiconductors (2D NiO, WO_3 and 2D MgO) have been syntehsized to enhance the photocatalytic activity under visible light irradiation by tailoring their optical properties. Moreover, the incorporation graphene sheets offer large surface area and active site for photocatalytic activity. The prepared photocatalysts were applied for the degradation of organic pollutants (MO, 2,4 DCP and Congo red).

In my present work, 2D/2D graphene/NiO composites with various concentration of graphene was synthesized to enhance the photocatalytic efficiency under visible light irradiation. The synthesized 2D NiO sheet via effective chemical method clearly seen in SEM images. Moreover, the band gap of 2D NiO was tailored by inducing the optimum contents of graphene sheets as studied in UV-vis apbsorption spectra. The large surface area and strong interfacial interaction between 2D/2D graphene/NiO retard the recombination rate of electron/hole pairs as examined through PL spectra led to excellent photocatalytic performance against MO.

N-graphene/WO_3 nanocomposites as active photocatalysts with optimum content of N-graphene were fabricated through wet chemical method. The effect of N-graphene on WO_3 was investigated through different characterization technique such as RAMAN, XPS, PL, FTIR, etc. In N-graphene/WO_3 nano structure the interconnected network of N-graphene allow dispersion of WO_3 and improved the light harvesting ability of WO_3 photocatalyst confirmed by UV-vis spectra.

Therefore, the N-graphene/WO_3 nanocomposite exhibited superior degradation performance against mixture of strong pollutants (2,4 DCP, MO) than pure WO_3 attributed to increase charge separation ability through z-scheme photocatalysis owing to nitrogen functionalities in N-graphene.

2D MgO sheets was prepared through co-precipitation method. The 2D MgO is poor visible light responsive photocatalyst due to large band gap. The photocatalytic efficiency of 2D MgO was improved by synthesizing binary composite 2D/2D MgO@G (seen in SEM images). 2D/2D MgO@G strong interfacial interaction boost the photocatalytic activity of MgO towards Congo red under visible light. Moreover, incorporation of CQDs in 2D/2D MgO@G composite scavenge the electrons and increased the roughness of surface which promotes the enhanced photocatalytic degradation of CQDs/MgO@G (99%) than binary 2D/2D MgO@G composite and pure MgO.

List of abbrevations and symbols

CQDs	Carbon quantum dots
N-graphene	Nitrogen doped graphene
GO	Graphene Oxide
NiO	Nikel oxide
MgO	Magnesium oxide
WO3	Tungsten trioxide
VB	Valence band
CB	Conduction band
MO	Methyl orange
2,4 DCP	2,4 Dichlorophenol
SEM	Scanning electron microscopy
HRTEM	High resolution transmission electron microscopy
FTIR	Fourier transform infrared spectroscopy
PL	Photoluminescence
XRD	X-ray Diffraction
EDX	Energy dispersive X-ray analysis
XPS	X-ray photoelectron spectroscopy
DRS	Diffuse reflectance spectra

Contents

List of Figures

List of Tables

CHAPTER 1

Introduction

1.1 Background of Photocatalysis

Environmental technology is facing some critical issues based on increasing air and water pollution. Industrial, agriculture and domestic activities, accidental spillage, sewage and storm water, other global and environmental changes are the main sources of water pollution [1,2]. The numerous pollutants present in contaminated water depends on the nature of agricultural, industrial, and municipal wastewater releasing activities. There is various type of water pollutants such as organic, inorganic is biological in nature. The inorganic water pollutants are composed of heavy carcinogenic and toxic metal. [3]. While the organic pollutants that greatly affect the human life as well as environment and their effective tendency depends on their structure. As a result, organic pollutants are further classified into three types based on their chemical composition (1) organometallic compounds (2) hydrocarbons (3) oxygen, phosphorus, and nitrogen compounds [4].

The first category consists organometallic compounds with metals like tin and lead. Industrial discharge materials and agriculture activities are major source of organometallic compounds. The second category is consist of hydrocarbon and their related compounds such as PAHs (polycyclic aromatic hydrocarbons), dioxins and DDT (dichloro-diphenyl-tri chloroethane). These compounds have less solubility in water and more in fats owing to low polarity. Consequently, they persevere in the environment through agglomeration in the fatty tissues of organisms. The third group is consisting of heteroatoms like oxygen, nitrogen, and phosphorus in the hydrocarbon structure. The abovementioned atoms are responsible for high polarity of related compounds which make them fat insoluble and more water soluble. As such, heteroatoms related compounds are less persistent because they dissolve easily through the environmental activities [4-5]. Moreover, dyes are also stable organic molecules owing to complex structure have extensive use in food, rubber, plastic, paper, textile, and printing industries. These stable organic dyes are carcinogenic and poisonous in nature which are not easily affected by light, temperature, and microbial attacks. Only 15 % dyes are extinct during dyeing activity. Consequently, the elimination of them is an imperative issue. As a result, shortage and increasing demand of clean water sources account of rapid population growth, industrialization and long-term droughts have become a worldwide problem. Numerous practical schemes have been applied to produce possible water resources. To store rainwater for regular activities and enhancing the catchment capability for water are the scarce techniques to solve the short-term water problems. To suppress the deteriorating of sanitary water shortage, it is essential to develop an effective, highly efficient, and cheap water treatment techniques to clean the wastewater. For this purpose, generally used techniques can be divide into two categories: chemical and physical methods. Screening, distillation, sedimentation, filtration etc. are included in Physical method while Chemical methods are contained adsorption, coagulation, and chlorination [2].

The major drawback of all other above mention high-cost techniques to produced hazards secondary pollutants as a by-product which are harmful for human health [6,7]. In modern era, it is imperative to develop most effective, inexpensive, and minimum time-consuming technique to attain safe water. AOP (advance oxidation process) is advanced technology that has the capability to oxidize pollutants rapidly. In advance oxidation process the reactive radicals are created with the help of energy sources (sun), one or more oxidants (hydrogen peroxide, ozone, oxygen etc) and catalyst, which can oxidize the contamination present in water [8]. Therefore, photocatalysis is an efficient method for numerous purpose (i) production of hydrogen (ii) for degrading both aquatic and atmospheric organic pollutants (iii) and antibacterial activity [8,9]. In Recent era, the photocatalysis has been gaining tremendous attention in wastewater treatment to acquire complete mineralization of the contaminations [6].

1.2 Nanoscale photocatalyst

Nanotechnology has motivated the researchers to explore the research, where the intriguing and unique properties of nano-scale materials provide more sustainable and effective solutions of prevailing effluent-water problems that leads to environmental toxicity. In the nanomaterials, surface properties and quantum effects become more dominant because their large surface area offer more active sites to promote surface dependent properties. So, nanomaterials are good adsorbents owing to their fascinating physiochemical properties to boost the photocatalytic efficiency by decreasing the diffusion length of charge carriers [10-12].

1.2.1 Semiconductor photocatalyst

Over a past decades, the researchers have been paying more attention on photocatalytic reaction that occurs on semiconductor oxides, selenides, and sulfides surface. Metal selenides and sulfides are not suitable for photocatalytic activity because they are unstable, photo-corrosive, and poisonous. Whereas the nano-size semiconductor such as CeO_2, TiO_2, ZnO, Cu_2O, NiO, WO_3 etc have been found more effective photocatalyst on account of their less toxicity, high physiochemical stability and photo-catalytic efficiency, specially having strong capability to completely degrade the organic contaminants into innocuous products (CO_2 and H_2O) [12].

1.2.2 Properties of photocatalyst

The points that are given below should be taken under consideration while choosing photocatalyst for outstanding photo-catalytic activity:

- Band gap is an important feature of photocatalyst. The light irradiation must have energy equal or greater than the band gap energy of catalyst to proceed the reaction.
- The photon absorption capacity of the catalysts should be as high as possible to generate more electron–hole pairs.
- The recombination process of electron–hole pairs must be prevented as much as possible to enhance the quantum efficiency of the photo-generated electron–hole pairs.
- The surface area of the catalysts should be large to provide more reaction sites; and
- The chemical and physical structures of photocatalysts must be stable and be beneficial for the mass transfer in water.
- High crystalline photocatalyst is essential for photocatalytic activity because the defects on the material surface behave as recombination centers for the charge carriers, decreasing the catalysis rate. Furthermore, Lifetime and transferring rate of charge carriers also rely on the crystallinity of materials. In highly crystalline photocatalyst, transferring and lifetime of the charge carriers are also enhanced to leads efficient photocatalytic activity.

1.3 Photocatalysis

It is chemical reaction accelerated by the absorption of light irradiation (photons) via photocatalyst. There is no changes occur in photocatalyst before and after chemical reaction. Thus, photocatalytic materials used as a catalyst during catalytic reaction.

1.3.1 Types of Photocatalysis

(a) Homogenous Photocatalysis

If the medium and catalyst have the same phase, then it is known as homogeneous photocatalysis. Homogeneous photocatalysis contains soluble molecular catalyst's assembly including catalytic sites for reduction and oxidation chemical process and light absorbing system on a single form. Transition-metal complexes are most suitable photocatalysts for homogenous photocatalysis owing to their suitable band gap and good stability. The production of $^{\bullet}OH$ radial is fundamental parameter in homogeneous photocatalysis. During this process, the Photo-Fenton reaction produces $^{\bullet}OH$ radials under light irradiation causes the reduction of photocatalysts. Under this state, regeneration of Fe^{2+} is allowed by Fe^{3+}, Fenton reaction take place owing to existence of H_2O_2 and iron act as a catalyst as depicted in given below equations.

$$Fe^{2+} + H_2O_2 \longrightarrow Fe^{3+} + OH^- + {}^{\bullet}OH \quad (1.1)$$

$$Fe^{3+} + H_2O + HV \longrightarrow Fe^{2+} + H^+ + {}^{\bullet}OH \quad (1.2)$$

$$[Fe^{3+} L_n] + HV \longrightarrow [Fe^{2+} L_{n-1}] + L^{\bullet} \quad (1.3)$$

In equation 1.3, L (organic ligand) is more effective than oxidation of organic substrate through $^{\bullet}OH$. Thus, the efficient pollutant degradation during chemical reaction is due to substances containing many carboxyl and hydroxyl groups produced by the oxidation of inert hydrocarbons via $^{\bullet}OH$ can contribute to afterward reactions [13,14].

(b) Heterogeneous Photocatalysis and its mechanism

If the reaction medium and catalyst are not in the same phase, then it is known as heterogeneous photocatalysis. Heterogeneous photocatalysis is the most useful method for water treatment because catalyst material can easily be separated after the application. Generally, solid phase semiconductor based photocatalyst on which liquid phase targeted molecules get adsorbed where degradation phenomenon take place.

Photocatalytic process mainly depends upon the light energy or wavelength. Photocatalyst are used as catalyst which stimulates the redox reaction under light irradiation owing to their electronic feature. Under light irradiation, the holes produced in valence band of photocatalyst oxidize the water molecules to form hydroxyl radicals (having strong oxidizing power) as well as electrons in conduction band react with oxygen molecules to produced $O_2^{\bullet-}$. Subsequently, these OH· and $O_2^{\bullet-}$ radials undergo redox reaction that completely degrade the pollutants into water and carbon dioxide. [15,16]. The photocatalytic phenomenon take place in photocatalyst is described below by the following equations [17].

$$\text{Photocatalyst} \rightarrow \nu\ e^-_{CB} + h^+_{VB} \qquad (1.4)$$

$$\text{Photocatalyst}\ (e^-_{CB}) + O_2 \rightarrow O_2^{\bullet-} \qquad (1.5)$$

$$\text{Photocatalyst}\ (h^+_{VB}) + H_2O \rightarrow H^+ + {}^{\bullet}OH \qquad (1.6)$$

$$\text{Pollutants} + {}^{\bullet}OH + O2^{\bullet-} \rightarrow \text{Degradation products} \qquad (1.7)$$

Photocatalytic mechanism strongly depends on redox potential. In addition, the transferring and recombination rate also rely on the position of valence and conduction band.

Based on band alignment, it has been divided into three groups.

Straddling gap

In this type of hetero-junction, both n and p type semiconductors are directly connected, generating p-n junction at the interface due to transferring of holes and electrons which is responsible for forming electrical potential that leads to movement of holes and electrons in same direction. For example, excited electrons from conduction band of semi-conductor A to move another semiconductor B and holes also migrate from valence band of semiconductor A to semiconductor B (as shown in fig.1.1a) causes the retardation of recombination rate and improve the photo-catalytic efficiency. But this type of heretojunction doesn't exhibit excellent photocatalytic activity due to accumulation of charge carriers in one semiconductor.

Staggered Gap

Two semiconductors having appropriate band gap relate to each other in such a way that excited electron from one semiconductor's (A) conduction band moves toward the other semiconductor (B) of low energy conduction band under light irradiation. The valence band of the semiconductors are aligned in this way that that the holes travels in opposite direction of electrons, causing increased charge separation rate to enhance the photo-catalytic activity (fig.1.1b).

Broken Gap

This kind of hetero junction is like staggered gap except that the band gaps don't overlap (fig.1.1c). Consequently, the separation and migration of charge carriers between the semiconductors doesn't occur, making it unfavorable for enhancing photocatalytic performance [18,19].

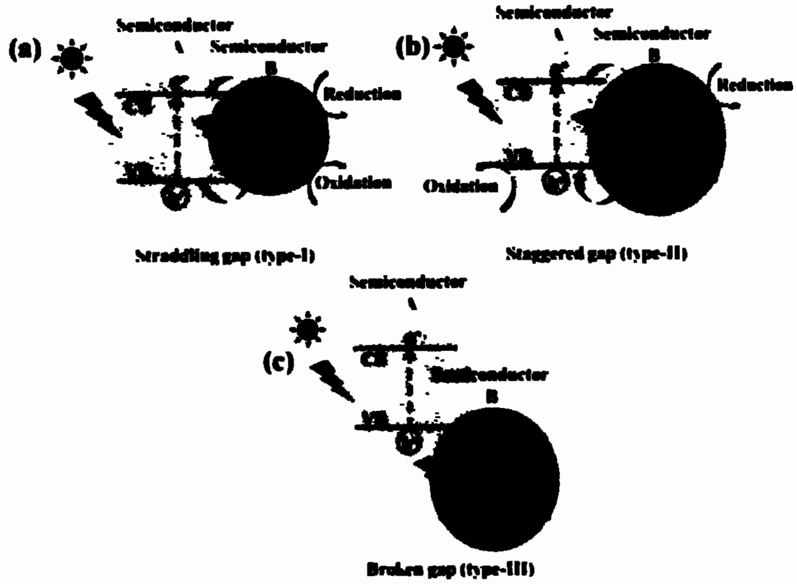

Figure 1.1. Band alignment of different herojunction (a) Straddlig gap (b) Staggered gap (c) Broken gap [20]

© Z-scheme photocatalysis

There are two main drawbacks of hetero photocatalysis. (i) Photocatalytic mechanism strongly depends on redox potential. In addition, the transferring and recombination rate also rely on the position of valence and conduction band. Redox reaction will be accomplished if the valence band and conduction band have more positive and negative potential, respectively than potential of surface reaction. Under light irradiation, exited electrons will migrate to the conduction band of another semiconductor having low negative potential whereas the holes will move to valence band of anther semiconductor also have low positive potential as shown in above fig. cause to reduce the redox capability of charge carriers which decrease photo catalytic efficiency.

(ii) The recombination of charge carriers and redox potential effected by electrostatic repulsion force in hole-hole and electron–electron.

Therefore, it is necessary to design and explore new photocatalytic systems to solve these problems. Z-scheme is superior to hetero photocatalysis. In Z-scheme, excited electrons having low potential will move towards the valence band (holes) of semiconductor II while the conduction and valence band of semiconductor I and II having strong reductive electrons and oxidative holes which not only increase the charge separation rate but also maintain the strong redox potential to take part in photo catalytic process [21].

1.3.2 Classification of Z-scheme photocatalyst

(i)Traditional Z-scheme (ii) Solid state Z-scheme (iii) Direct Z-scheme

(i) Traditional Z-scheme

The concept of z-scheme has been proposed in 1979. This system consists of two different semiconductors with appropriate electron mediator i-e IO^{3-}/I^{-}, Fe^{3+}/Fe^{2+}. Under light irradiation, both semiconductors are excited, resulting in photo-generated holes and electrons in their valence and conduction band respectively. The electrons in conduction band of semiconductor-I will migrate to the valence band of semiconductor-II through redox mediator. In redox mediator, the holes in valence band of Semiconductor-II interact with electron acceptor, producing the corresponding electron donor and electron in conduction band of semiconductor-II react with electron donor, engendering electron acceptor. Thus, the retain holes and electron in valence and conduction band of semiconductor-I and II have strong redox to participate in chemical reaction (fig.1.2a).

Drawbacks of traditional Z-scheme

The light shielding due to strong absorb redox mediator, pH sensitivity, transfer rate of photo-generated charge carriers decreased due to diffusion of ion pairs are the few issues of traditional z-sheme leads to limit their board applications. In addition, mostly electron mediators are unstable causes to reduce/suppress the chemical reaction rate [22-24].

(ii) Solid state Z-scheme

In solid state Z-scheme, the conductor such as Ir, Ag, Au, and Cu etc inserted between two different photo catalysts forms an ohmic contact with minimum contact resistance. The Noble metals act as solid mediator are high stable play an imperative role to increase the transferring rate of charge carriers and stability of photocatalysts. Due to effectively improve transferring of charge carriers by the insertion of conductor, the solid-state Z-sheme can work in gas as well as in liquid phase. The photogenerated charge carriers simultaneously in valence and conduction band of two photocatalysts under light irradiation. The electron from conduction band of photo-catalyst -A to valence band of other photo-catalyst B via ohmic contact which leads to increase in charge separation. Moreover, the reserved electrons and holes in photocatalysts (fig.1.2b) takes part in strong reduction and oxidation reaction respectively to degrade the pollutants [24-26].

Drawback of Solid-state Z-scheme

- Though, some solid conductors are very expensive, causes the shielding effect because it can absorb light itself which effectively reduce the utilization of light irradiation efficiency for photo-catalyst reaction to some extent [22].
- Synthetic point of view, it is very difficult that the precisely synthesized nano-size solid conductor lies between the two photocatalysts. Mostly, the solid conductor distributed randomly on the photo catalysts' surface which behave as a co-catalyst rather than electron mediator [23].

(iii) Direct Z-Scheme

To resolve the above-mentioned issues in Solid state Z-sheme, Cheng and coworkers proposed the direct Z-scheme in 2010 and Yu and coworkers experimental approved this proposed Z-sheme in 2013. This consist of two different suitable narrow band gap photocatalysts. The heterojuntion between two photocatalyst is based on their band position and Fermi level. In this Z-sheme, the Fermi level of reductive photocatalyst will be less negative than oxidative photocatalyst. Therefore, electrons oxidative photocatalyst interact with holes in reductive photocatalyst without redox mediator and noble metals to attain Fermi level equilibrium at heterojunction. This transferring of charge carriers builds an internal electric filed at contact interface (fig.1.2c). The electron/hole pairs are migrated due to presence of built-in electric field [27-29]. As a result, when light falls on the photocatalysts, the photogenerated electron on oxidative photocatalyst combine with hole on reductive photo catalyst due to presence of electrostatic force leads to elimination of photo generated inactive electron and holes. In addition, highly reactive preserved electrons and holes effectively used for photo-chemical reaction. Besides, the separation of reactive reduction and oxidation sites increased via direct Z-scheme which is more favorable for efficient photo catalytic performance. Thus, the formation of direction Z-scheme photocatalyst have great potential for board practical applications [29].

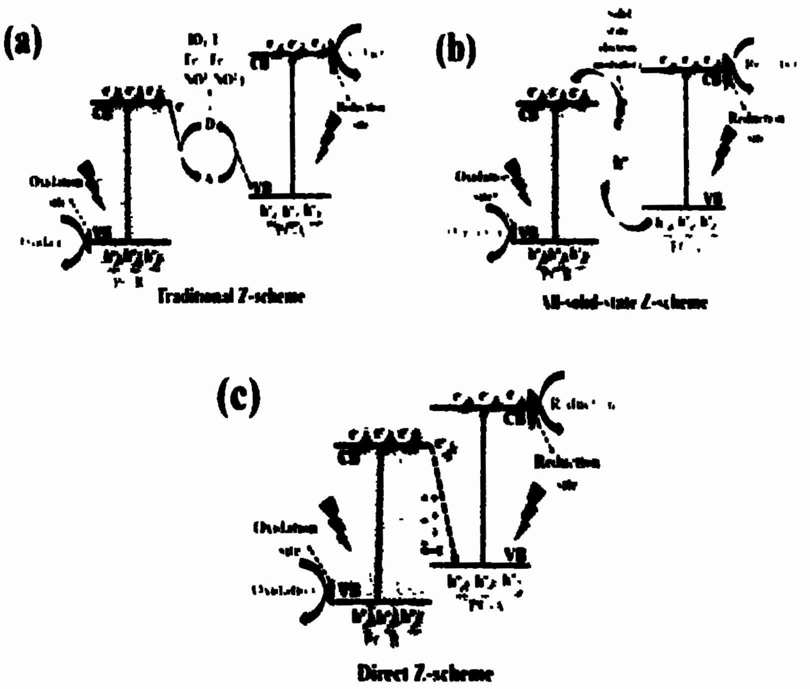

Figure 1.2: Different types of Z-schemes photocatalysis (a) Taditional Z-scheme (b) All-solid-state Z-scheme (c) Diret Z-scheme [30]

1.4 Factors affecting the degradation performance

(a) Morphology of catalyst

The surface morphology such as, porosity, particle size, and surface area play a vital role to attain excellent photocatalytic performance. Morphology of nanomaterials having small particle size and large surface area effectively exhibits higher photocatalytic efficiency. Because large number of atoms are agglomerated on the catalyst surface to promotes high surface to volume ratio which increase the transfer rate of photogenerated charge carriers and provide more active sites. Consequently, the surface morphology of catalyst significantly affects the photocatalytic activity because oxidation and reduction process occur on their surface.

(b) Effect of pH

The pH of the solution is another imperative factor for determining the percentage degradation of organic pollutants. The degradation process is very sensitive to the pH of photocatalytic reaction [31-33]. So, the adsorption of pollutant's molecule on the surface of photocatalyst mainly control by the pH of the reaction solution. Therefore, the degradation phenomenon depends on the ionization and charge on catalyst surface and the contaminants. In acidic solution, when pH value is less than zero-point charge of photocatalyst causes the positive charge on photocatalyst leads to rapid adsorption of anionic organic molecules while in reverse conditions (alkaline solution), the cationic molecules are absorbed by negatively charged surface of photocatalyst. Meanwhile, the photodegradation of pollutants is retarded at higher pH (pH >12) because massive production of hydroxyl radicals competes with the organic molecules for adsorption on photocatalyst's surface [34,10].

(c) Light Intensity

The degradation of pollutants is foremost relied on the intensity of light irradiation absorbed by the photocatalysts [11] For a substance to be photoactive, it is necessary for it to absorb light with a threshold wavelength for electronic excitation from the valance band to the conduction band, so that the electrons and holes can migrate onto the catalyst surface [35]. In photocatalytic reaction, the degradation rate will be different under the light irradiation having different wavelength. The reaction rate increases linearly as the light intensity increases because the light irradiation is received by photocatalyst is also increase which stimulate the electrons and enhance photo catalytic activity. Moreover, there is no significant effect on degradation rate on further increasing in intensity because optimum number of photons are required to excite all photocatalyst's particle. Therefore, further increasing light intensity doesn't affect the degradation rate [36,37].

(d) Catalyst loading

The amount of photocatalyst is one the significant factor to control the photocatalytic degradation. The high concentration of photocatalyst enhance the degrading efficiency of pollutants an account off more active sites which leads to the formation of hydroxyl radials. At lower catalyst concentration, maximum light is transmitted via reactor and remaining fewer light radiation is utilized during photocatalytic reaction causes the reduce degradation efficiency. Moreover, increased catalyst loading than optimum value leads to blocking of light penetration on the surface of photocatalyst to proceed the reaction. Because the accumulation of particles increases as the concentration of photocatalyst enhance causing the reduction of surface area to absorb light irradiation thereby abatement formation of electron/hole pairs greatly affect the photocatalytic performance [38-41].

(e) Concentration of pollutants

The concentration of pollutants plays a significant role to attain tremendous photocatalytic performance. The degradation efficiency of pollutants enhanced as the concentration of catalyst increase up to suitable value and reduce as the pollutants' concentration increases beyond the limit. Because the high concentration of pollutants causes more absorption on photocatalyst surface which hinder the reaction between reactive species and absorbed molecules and screening the light penetration to the surface of the photocatalyst. So, the amount of photocatalyst should be adjusted based on pollutant's concentration for efficient degradation rate. [42].

(f) Oxygen

Oxygen acts as an electron acceptor because pre-adsorbed oxygen molecules on catalyst surface capture the photo-generated electrons to suppress the recombination rate of charge carriers which enhance the degradation rate. So, the photocatalysis reaction rate increases as the oxygen increases [43].

1.5 Applications of photocatalysis

In recent years, the environmental and energy issues arise due to stimulation of industrialization cause the water and air pollution that directly affect the human life. Photocatalysis is ecofriendly technique due to simple oxidation equipment, excellent oxidizing ability, production of harmless by-products. Therefore, photocatalysis technology is widely used in various fields such as sterilization, hydrogen production via water splitting, air purification, the decomposition of sewage and carbon dioxide photo-reduction etc. Moreover, this is also extensively used in automobiles, agriculture, roads, buildings, and household appliances. Subsequently, researchers still fabricating stable visible light driven photocatalyst to boost up their photocatalytic activity and to promote the board applications of photocatalytic technique.

1.6 Semiconductor

1.6.1 Nickel oxide (NiO)

The NiO semiconductor composed of Nickel (78.55%) and oxygen (21.40%) [44]. NiO has rock salt fcc crystal structure shows the feature of p-type semiconductor due to nickel vacancies [45-47]. In NiO crystal structure, at octahedral coordinate, nickel cations have valence state of 2+ ($3d^8$) leads to strong interaction between electrons in 3d orbitals cause optical band gap in the range of 3.4-4.0 eV [48]. 2D NiO semiconductor has large surface area, high chemical stability, excellent electrical conductivity as well as optical properties. Moreover, its low toxicity, quantum size confinement, highly reactive and ecofriendly nature making it as a promising candidate for multiple applications. NiO also act as photocatalyst to degrade the strong organic pollutants into harmless products [46,49,50].

1.6.2 Tungsten Trioxide (WO_3)

Thermally stable N-type WO_3 semiconductor with band gap (2.4-2.9) have complicated crystal structure in which WO_6 regular octahedral structure based on shared corners and edges connected with other through weak van der waals force. Furthermore, oxygen atoms are attached at the corner of each octahedron [51-53]. Owing to their unique crystal structure and feature such as nontoxic, excellent electron mobility, active both in UV and visible light region due to narrow band gap (2.4-2.9eV) making it promising material in various fields (de sensitized solar cells, sensing of toxic gases, photoeletrocatalysis, photo catalysis, and water splitting photocatalyst) [54, 55].

1.6.3 Magnesium oxide (MgO)

MgO is an insulator having a rock-salt like structure. In rock-salt structure each cation is associated with six neighbor anions making it neutral and stable material. So, each magnesium ions Mg^{2+} is linked with octahedral oxygen ions ($\dot{O}^{2-}$ anions) as shown in fig.1.3. The magnesium is in 2p state because it donates two electrons to neighbor oxygen atom. MgO has been widely used in multiple applications owing to its tremendous properties such as non-toxicity, high hardness and temperature resistance, low cost, and optical transmittance. But its applications are limited due to wide energy band gap which can be modified by an effective method (nanocomposites) [56,57].

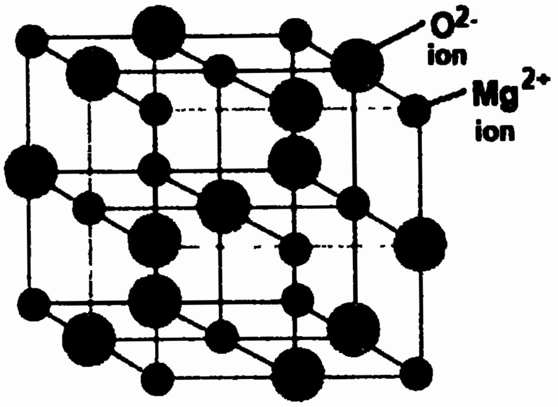

Figure.1.3: Crystal structure of MgO [58]

1.7 Limitation of semiconductor photocatalysts

The photocatalytic efficiency of semiconductors has the following limitations.

- Minimum interfacial photo-generated charge transferring and separation rate
- Quick recombination of photo-generated charge carriers
- Having minimum visible-light response
- Relatively low surface area
- Most semiconductors having minimum visible-light response owing to their large band gap which make them less effective over a wide solar photocatalysis applications [59,60].

1.8 Semiconductor/ graphene sheets

In present era, 2D carbon-based nanomaterials have been gaining more attention as an excellent photo catalyst for wider potential in photo catalytic applications owing to fascinating properties. 2D carbonaceous materials such as carbon nitride, graphene oxide and graphene etc offer a niche for tailoring their physiochemical properties, which assist to suppress the charge recombination rate which is favorable for photodegrdation of pollutants. Among all other carbonaceous materials, exfoliation of graphene (2D carbon allotropy) in 2004 has gained substantial attraction for hosting numerous intriguing properties which attributed to its novel electronic band feature. The fascinating electronic structure, high conductive surface, light absorption of wide range of wavelengths and the large surface area due to 2D crystal lattice (sp^2 carbon network), making it an ideal candidate to enhance the photocatalytic efficiency. [59, 61-63] Besides, graphene sheets allow ballistic transport making itself an ideal electron transfer media or electron acceptor. Therefore, Graphene base semiconductor photo catalyst is more valuable/suitable to boost the photo degradation of pollutants because incorporation of graphene delays the agglomeration of nanomaterial and increase large surface area of synthesized sample for adsorption of pollutants [59].

1.9 Graphene sheets

1.9.1 Structure and electronic properties of graphene

In graphene, outer orbitals of carbon atom are comprised of three sigma bonds separated through 120 and one $2p_z$ remaining orbital aligned perpendicular to the graphene surface. The two corresponding carbon sub lattices a, b per unit cell forms the hexagonal lattice structure of graphene sheets. The pi-electrons between two adjacent carbon atoms having $2p_z$ orbitals relate to π^* and π bands that form empty CB (conduction band) and filled VB (valence band) respectively. The π and π^*bands meet at six points known as direct points (fig.1.4. Ref. 63). The two independent point (K' and K) exhibits linear dispersion of orthogonal π^* and π states owing to symmetrical structure of graphene sheets. The two bands (π and π^*) touch at Dirac pints show that the graphene is a semiconductor with zero band gap or semimetal.

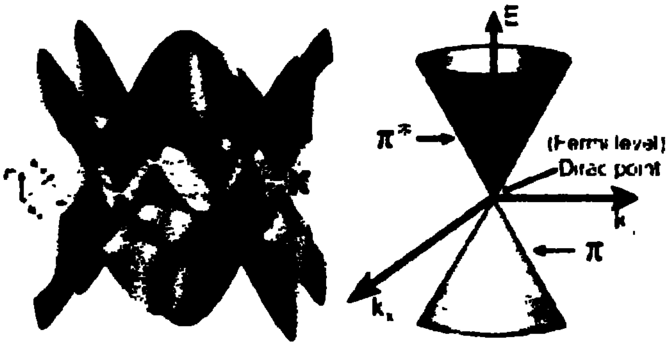

Figure.1.4. Band position of graphene sheet [63]

1.9.2 Role of graphene sheet in photocatalysis

Graphene base nanomaterials an effectively remove the pollutants through two was adsorption and photo-degration. Graphene has tremendous properties (e.g large specific surface area, hydrophobic nature) which make it excellent adsorbent for organic molecules than other carbonaceous materials like AC (activated carbon), CNTs (carbon nanotube) and GO (graphene oxide).

The most essential adsorption reaction between graphene and organic molecules is pi-pi interaction. Because the graphene contains pi-electrons, perpendicular to the surface, actively interact with pi- electron of organic compounds to form pi-pi bond. For maximum adsorption of organic pollutants, the graphene exhibits strong pi-pi interaction due to presences massive, delocalized pi electrons on its surface. This interaction greatly affected by relative position and number of aromatic rings exist in the organic molecules and carbon-carbon double bond of molecules to hexagon graphene. It is noteworthy that graphene surface has resilient tendency to adsorb pollutants due to massive pi electrons and flat conformation. In contrast, graphene oxide is not favorable to process the pi-pi interaction between aromatic ring and p-orbitals (graphenee oxide) owing to present of less p electrons. Therefore, the graphene is considered is an ideal material for the degradation of organic pollutants that comprised of benzene rings or C=C double bonds.

1.9.3 N-doped graphene sheets

Graphene is a promising candidate for photo catalytic performance, however there are few drawbacks of ggraphene. In pristine graphene, the unpaired pi- electrons are tightly bonded in it delocalized conjugate system making it chemically inert which retard its reactivity and absorptivity. Though these pi-electrons cause the adsorption of pollutants via pi-pi interaction, but this interaction is minimal and weak. Luckily, the incorporation of heteroatoms with a various electronegativity will break their crystal lattice leads to formation of unbalance charge distribution which assist as massive active sites. Therefore, formation of abundant active sites making grpahene chemically rich for strong interaction assist to boost the photocatalytic activity. Furthermore, doping of heteroatom in graphene sheets open a band gap of graphene (change metallic to semiconductor) due to formation of additional electronic states caused to explore its nano-range features. Consequently, this is most desirable practical technique for low- cost and metal free photocatalyst making it catalytically capable for its own [63,64]

1.9.4 Structural of NG

Incorporation of heteroatoms like O, F, H, N, etc modify the electronic properties of graphene sheets. Tailoring the charge distribution of graphene surface by introduction with various elements effectively modify their physiochemical features. The dopant elements act as acceptors or donor based on their electronegativity. As compared to other heteroatoms, nitrogen doped atoms exhibit the excellent results because N 1s orbit have higher energy level which is responsible for rising the energy level of hybridized orbital. N-graphene have four types of N-bonding configuration (i) N pyrrolic, (ii) pyridinic N-oxide, (iii) N quaternary or N graphitic and (iv) N pyridinic. In pyridinic nitrogen, the N-atom (N_1) swaps the carbon atom at edge or vacancy of hexagonal ring of graphene sheets. Second, Quaternary nitrogen also known as graphite nitrogen which maintain the hexagonal ring structure by introducing the nitrogen atom in non-vacant place of sheets as shown in Fig. lastly, the substitution of N-atoms forms the five member ring with carbon atom in sheet called pyrrolic nitrogen. (fig.1.5). [63-66].

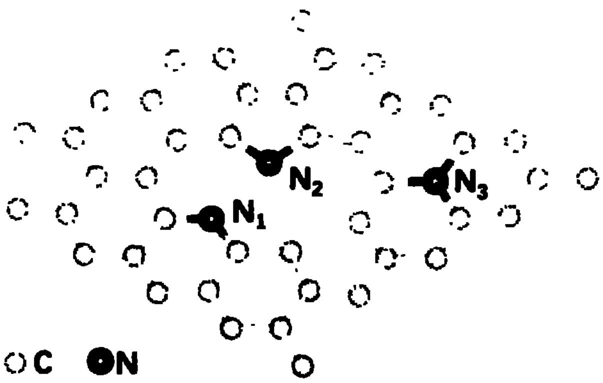

Figure. 1.5: Structure of nitrogen doped graphene: N1 (pyridinic), N2 (pyrrollic) and N3 (Quaternary) nitrogen atoms [67]

1.9.5 Band structure of NG

Pristine graphene is a zero-band gap semimetal in which pi- and pi * band of sheets symmetrically touch at Dirac cone where the Fermi level lies (Fig.1.6a). Doped N-atom tailored the band structure of graphene sheets. N-atom has one extra electron than C–atom cause the excessive pi-electron to occupy the π^*-state conduction band (Fig.1.6b) leads to open the band gap. The concentration of nitrogen atoms plays an imperative role to tune the band gap of N-graphene to fulfill the desired demand. Subsequently, the modified band and atomic structure of N-graphene brings major advantages in photocatalytic applications.

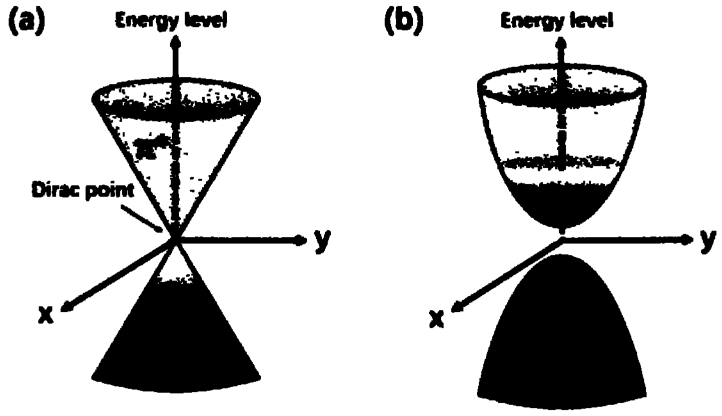

Figure.1.6: Band position of graphene (a) and N-graphene (b) [67]

1.9.6 Advantages of N-doped Graphene

- Generally, the N-graphene sheets have thickness in the range of nanometer. The doping of NG in semiconductor provides the short path for photo-generated charge carriers, assisting the transfer of electrons from semiconductor to NG surface (comprise of massive active sites) for chemical reaction. As a result, NG retards the recombination rate of charge carriers and enhance photo catalytic activity.
- The charge distribution and spin density of C–atoms are affected by N-doped atoms, creating active areas on graphene sheet surface. These "activated areas" are conductive to hosting reactive species. Therefore, N-atoms facilitate to boost the activation and adsorption of reactants and directly contribute to chemical creation.

Morover, N-graphene shows strong interfacial interaction with other semiconductors photo-catalysts leads to increase photo-catalytic performance. Thus, Tunable band gap and structure properties of N- graphene open its potential in versatile applications [68,69].

1.10 Carbon quantum dots

Carbon quantum dots have quasi spherical shape (zero dimension) with a diameter less than10nm and consist of oxygen, nitrogen, carbon, hydrogen etc [70,71]. Due to their intriguing properties non-toxic, photo-stability, chemically inert, wavelength dependent photoluminescence and their hydrophilic nature making it an ideal candidate for environmental applications [71,72].

CHAPTER 2

Literature Review

2.1 Photocatalysis

From last two decades, nontoxic, cheap, and ecofriendly photocatalysis approach have been gaining tremendous attention for environmental remediation and researchers still working to fabricate an efficient visible light active photocatalyst for energy applications to fulfill the desire energy growing demands of mankind. First Berzelius introduced the word "catalysis" and later (1910) the term "photocatalysis" was coined in a book by the Russian scientist J. Plotnikow. Besides the environmental remediation through photocatalysis, the researcher offered an innovative idea to generate the fuel from water splitting process. To proceed the purpose of my research, here I will briefly explain the review of different research groups worked on the different semiconductors and graphene base materials to utilize in environmental remediation.

2.2 Semiconductors and graphene base semiconductor as photocatalyst

The semiconductors are considered as a component material in photocatalytic applications such as (hydrogen production through photocatalytic water splitting and decomposition of pollutants etc) owing their fascinating charge transport ability and electronic features. Different semiconductors (WO_3, NiO, MgO etc) have been used in various environmental applications not only itself used as photocatalyst but also fabricated different nanocomposites by introducing other materials into semiconductor via different synthetic routes.

Among all other arbon 2D Graphene nanosheet with intriguing intrinsic properties such as light gathering, high electron mobility making it an ideal candidate as photocatalyst. Therefore, the graphene-based materials are deigned to effectively utilize in multiple environmental applications.

In below section, the brief review covers the role of Semiconductors and graphene base semiconductors photocatalysts in photocatalytic applications.

2.2.1 Nickel oxide (NiO)

Motahari, F. *et al* synthesized the NiO nanoparticles through thermal decomposition process using β-Ni $(OH)_2$ as a precursor. The photocatalytic efficiency of NiO was evaluated to examine the different parameters such as pH, irradiation time, concentration of dye and photocatalyst to decompose the organic dye (Rhodamine B). The results indicate that the NiO is an effect material for photocatalytic activity under visible light [73]. Haider, A.J. et al Prepared NiO NPs via sol gel process using nickel acetate as a reagent material and then formed a NiO thin film through spin-coating method. They studied their photo-catalytic activity using $KMnO_4$ as a pollutant and the effect of particles weight and size was also analyzed for photo-degradation efficiency under visible light region [74]. Khairnar, S. D. et al, evaluated the photo-degradation of Rhodamine B and methylene blue with NiO NPs. They applied facile chemical method to prepare NiO nanoparticles using $NaHCO_3$ and $NiCl_2$ as starting a starting material. The prepared NiO was used as competent material due to low band gap and photo-stability to expose in visible light source. The photo-degradation performance was evaluated to analyze the effect of numerous factors such as concentration of NiO, radiation time, initial amount of de and pH. Thus, the results indicate that NiO exhibited excellent photocatalytic performance for both organic dye Rhodamine B and methylene blue at different pH value 7 and 2, respectively. Besides, NiO NPs was also used as antimicrobial activity against the gram-negative and positive microorganisms [75]. Maniammal,

K. et al adopted the two-step method to fabricate the semiconductor mesoporous NiO with average particle size 2-3nm which confirmed by the structural and surface and DC electrical conductivity techniques. The mesoporous NiO was found to be an excellent photocatalyst for the decomposition of organic pollutant (methylene blue) in aqueous solution in both visible and UV region owing to large surface area and presence of O^{2-} and Ni^{2+} vacancies. [76]. Chaudhary, S. *et al* examined the antibacterial, seed germination and photocatalytic activity of synthesized NiO nanodisks. The photocatalytic experiment exposed that the NiO nanodisks exhibit good photo-degradation (methylene blue 98.7%) and high photo stability. Morever, NiO nanodisks was also test for antibacterial activity against Escherichia coli *and* Staphylococcus aureus [77].

Thampy, U.U. et al, synthesized the ZnO/NiO nanocomposites to enhance the photocatalytic efficiency of ZnO. The experimental results revealed that the ZnO/NiO nanoomposites exhibit better degradation efficiency for MB than pure ZnO under solar irradiation owing to internal electric field create at interface of ZnO/NiO [78]. Chen, C. J. et al, purposed that the synthesizing NiO/TiO nanocomposites improved the photo-activity owing to P-N junction that leads to suppress the recombination of photo-generated charge carriers [79]. Vidya, J and Balamurugan, P. prepared the PANi—NiO composites through oxidative polymerization process. The photo catalytic experiment results indicate that that the prepared sample decomposed the methylene blue up to 76% under visible light illumination [80]. Faisal, M. et al, purposed that the synthesis of NiO/TiO nanoomposites with different of NiO showed excellent photo catalytic performance towards the methylene blue and gemifloxacin mesylate than pure NiO and TiO due to synergistic effect at the interface of NiO/TiO nanoomposites, porous structure, large surface area and low energy band gap [81]. Santos, R.K. *et al*, synthesized the Ag_3PO_4/NiO nanoomposites with various quantity of Ag_3PO_4 via precipitation process to improve their photocatalytic activity for environmental remediation. They employed the prepared nanoomposites for decomposition of organic dye (rhodamine B). The results suggested that the Ag_3PO_4/NiO photocatalyst showed the enhanced degradation efficiency than pure Ag_3PO_4 due to strong interaction between the phases [82]. Ding, M. et al investigate the photocatalytic performance of prepared ZnO@NiO by measuring the degradation percentage of both organic dyes (methyl orange and rohdamine B) under ultraviolet light source. The photocatalytic assessment revealed that P-N junction play an imperative role to increase the degradation efficiency of ZnO@NiO core–shell photocatalyst than pure NiO sheets and ZnO nanorods [83]. Chen J.Z.et al synthesized NiO/ TiO_2 omposites nanostructure on a film surface of TiO2. Their photo catalytic properties were analyzed by degradation the methylene blue in aeuous solution. The performed degradation experiment result revealed that the strong internal electric field effectively reduce the recombination rate of eletron/hole pairs. Besides, the minimum thickness of NiO also beneficial to transfer the photoengraved charge carriers on the surface to degrade the dyes [84].

Soofivand, F and Salavati-Niasari, M. evaluated the photocatalytic activity for degradation of methyl orange under both UV and visible light illumination with NiO/graphene photocatalyst. The performed photocatalytic assessment exposed that the large surface area of NiO/graphene composites (due to incorporation of graphene) is beneficial to reduce the recombination of charge carriers that led to improve degradation efficiency [85]. Rahimi, K. et al, Prepared rGO/NiO composites with optimum amount of reduce graphene oxide via thermal decomposition method. The induced reduce graphene sheets activate the NiO nanowire in visible region by reducing it optical band gap (3.3 to 2.8 eV). Therefore, rGO/NiO nanostructure exhibit the excellent photo-degradation towards the organic dye than pure NiO nanowire [86]. Sadhukhan, S. et al, Synthesized rGO/NiO nanocomposites via hydrothermal process. The synthesized material was used to expose their degradation efficiency under visible light source. The charge transformation from NiO to graphene effectively reduce the recombination rate which is more favorable for degradation of methylene blue [87]. Al-Nafiey, A. et al synthesized visible light-driven photocatalyst rGO/NiO to improve the degradation of performance of organic dye. The expose methylene blue (MB) under visible light irradiation was effectively degrade [88]. Chen, J. et al Have employed the Synthesize visible light active photo-catalyst TiO_2 (sheet) /NiO (nanorod) hetero-structure to degrade the methyl blue (MB) and phenol under visible light irradiation. The photo-catalyst showed good photo-catalytic activity (90%) and reusability against organic dye [89].

Above literature demonstrate that the fabrication of 2D materials is considered as efficient photocatalyst for degradation of water waste product. In my present work, I have synthesized novel photocatalysts 2D/2D NiO/graphene with increase massive active sites and large surface area which was more favorable for photocatalytic activity. The 2D/2D NiO/graphene photocatalyst showed excellent degradation efficiency toward methyl orange under visible light due to strong interfacial coupling.

2.2.2 Tungsten trioxide (WO_3)

The WO_3 is an N-type visible light-driven photocatalyst with band gap 2.7-2.8eV. But its photo catalytic efficiency in visible light region is limited due to quick recombination rate of charge carriers. Visible light photocatalytic activity of WO_3 is improved by tailoring its optical properties and surface morphology. There are following numerous reports in which the photocatalytic efficiency is increased by modifying the WO_3 with other semiconductors and carbonaceous material. Alaei, *M* et al prepared WO_3 NPs with two different average particles size (50 and 80nm) via spray pyrolysis approach. These light active photocatalyst showed different photocatalytic properties against Congo red and rohdamine B. They observed that the WO_3 with different particle size behave inversely with dyes in degradation reaction due to electrostatic surface interaction [90]. Desseigne, M et al exposed the photo catalytic efficiency of WO_3 NPs with two different morphologies pseudospheres and nano-plates synthesized through simple chemical method. The de-colorization of organic dyes exhibited that photocatalytic property of WO_3 (pseudospheres) photocatalyst was higher than WO_3 nanoplates [91]. Sayama, K.et al studied the photo catalytic properties of synthesized WO_3 from amorphous peroxo-tungstic acid. The potocatalytic experiment was performed at visible light region by exposing hexane along with WO_3. It showed high degradation owing to good crystallinity and large surface area than commercial WO3 [92]. Ashkarran, A. A. et al applied arc discharge approach to prepare the WO_3 NPs in deionized water medium. The size of NPs was increased as increasing the arc current. The increase particle size (64nm) tunes the optical band gap (2.9 to 2.6eV). The photocatalytic assessment concludes that the prepared photocatalyst at low current boost the photo-degradation efficiency of WO_3 NPs towards the Rhodamine B in visible light region owing to small particle size and large surface area [93]. Zhang, G et al successfully prepared high crystalline WO_3 sheets with average size 200-500nm by hydrothermal approach. Modified WO_3 sheets with Pt (act as co-catalyst) boost the photocatalytic properties of WO_3 in visible region. They observed that he 2% Pt/WO_3 sheets displayed good degradation efficiency against tetracycline than pure WO_3 nanosheets [94]. Wang, L. et al used hydrothermal approach to synthesize the WO_3 nanotube at 200°C. The synthesized sample showed better photocatalytic activity in visible light region for decomposing the rhodamine B than $WO_3 \cdot 0.33H_2O/WO_3$ and $WO_3 \cdot H_2O$ which were attained at 140 and 80°C, respectively [95]. Abazari, R. et al synthesized WO_3 NPs via reverse microemulsion approach to improve the photocatalytic performance in visible region. The observed that visible light photocatalytic performance for decomposing methylene blue as compared commercial P-25 TiO_2 and bulk WO_3 [96].

Liu, Z. et al Prepared $CaFe_2O_4$ (CFO)/WO_3 nanoomposites by mixing different of CFO in WO_3 to enhance the photocatalytic performance of WO_3 in visible light region. The visible light photo catalytic activity of $CaFe_2O_4$ (CFO)/WO_3 photocatalysts was evaluate by degrading the acetaldehyde. The experimental results reveal that the 5% CFO coupled with WO_3 displayed high photocatalytic efficiency. Moreover, ITO and Ag coating on the CFO also effectively enhance the photocatalytic properties [97]. Adhikari, S. et al Increase photo-response range and retard the recombination rate of photogenerated charge carriers by fabricating Bi_2O_3/WO_3 heterostructure via hydrothermal method. They observed that the as-prepared sample display higher photocatalytic activity by degradation the 4-nitroaniline and rhodamine B than pure WO_3 and Bi_2O_3 under visible light source [98]. Tahir, M. B et al exposed the visible light photo-catalytic properties of WO_3/TiO_2 photocatalyst by decomposing the ciprofloxacin. They found that incorporation of TiO modified the morphology and optical properties of WO_3 that promotes their photo-degradation efficiency. Therefore, increased visible light absorption rate and novel morphology structure are the key parameter to enhance the degradation efficiency of 2% of WO_3/TiO_2 nano composite [99]. Priya. A. et al fabricated $BiFeWO_6$/WO_3 composites with different wt % (1,2 and 3) of bismuth iron tungstate via wet chemical approach. The visible light irradiation was exposed on the synthesized composite to investigate their photocatalytic properties. The results indicates that the 1% $BiFeWO_6$/WO_3 composite displayed good photodegradation efficiency than pure WO_3 by increasing the charge transfer rate. Besides, the as-prepared composites showed good photo stability and reusability in visible range [100]. Chai, B. et al investigated the physiochemical properties and photocatalytic activity of Z-scheme WO_3/g-C_3N_4 heterostructures through various techniques which were synthesized B anchoring the wo3 nanoplates on the surface of g-C_3N_4. The introducing WO_3 on g-C_3N_4 not only increase interfacial contact area, but also promotes the separation and transferring rate of electron/hole pairs. Subsequently, the photo- degradation result reveal that higher photocatalytic efficiency could be ascribed to the formation of Z-scheme visible light photo catalyst [101]. Wang, S.L. et al purposed that the 2D photocatalysts (tungsten carbide/tungsten trioxide) effectively improve visible light photocatalytic application due to strong interfacial interaction that leads to enhance charge separation and transferring rate from the conduction band of WO_3 to tungsten carbide. As a result, the experimental results indicates that tungsten carbide and tungsten trioxide composites exhibited good degradation efficiency toward organic pollutant (89%) under vis-IR light Due to synergistic effect between them [102]. Leghari, S.A. et al prepared WO_3/TiO_2 nanoomposites with different contents (1, 2, 4,5, and 10 wt %) of WO_3 to improve photo degradation efficiency in visible light region. The obtained results demonstrate that the induce WO_3 at as electron acceptor causing to inhibit the recombination rate. Therefore, 5% WO_3/ TiO_2 photocatalyst showed higher degradation efficiency (70%) towards the methyl orange (MO) owing to large mesoporous spheres and novel mesostructure [103]. Sajjad, A.K. L. et al fabricated visible light active photocatalysts ZnO/WO_3 with different concentration of ZnO. The inhering of ZnO on WO_3 cause to reduce the band gap of WO_3 and retard the recombination rate of charge carriers. Therefore, 2%ZnO/WO_3 composite exhibited highest photo degradation of MO (100%) under visible light than pure WO_3 [104].

Ramesh, K. et al. prepared strong anchoring of metal oxide (ZnO, TiO_2 annd WO_3) over reduce graphene oxide sheet to increase organic pollutants (MB and BPA) absorption and charge transferring rate. Among them, RGO/TiO_2 exhibits highest photo degradation and good stability against BPA [105]. Tran, V. A et al. prepared the ternary photocatalyst Ag@WO_3@rGO to enhance the photo degradation of RhB under visible light. Moreover, the crystal structure and morphology of WO_3 is not affected by existence of rGO and Ag but they provide the path for electron transferring [106]. Shi, R.et al. successfully synthesized N-doped graphene-based $CuO/WO_3/Cu$ by using GO and Cu(salen)PW_{12} complex as the substrate and precursor respectively. The $CuO/WO_3/Cu$@CN photocatalyst effectively improved the degradation of organic dyes (CV, MO, RhB and MB) under visible light source [107]. Chaudhary, K et al. synthesized WO3-ZnO@rGO ternary nanocomposites by incorporating the WO_3-ZnO over rGO sheets through ultrasound-assisted method. The results indicate that the synergistic effects at the interfaces of WO_3-ZnO@rGO nanocomposites leads to increase transferring and separation rate of charge carriers which causes the improved photocatalytic efficiency (94%) as well as good stability towards the dye (methylene blue) under visible light [108]. Neena, D. et al prepared N-rGO/ZnO nano composites through solvothermal process to improve the photocatalytic efficiency for the photo-degradation of organic pollutants. The results indicate that the N-rGO/ZnO photo catalyst exhibited enhance photocatalytic efficiency towards the pollutant (2,4- DCP) than bare ZnO rods under visible light [109]. Khan, M. Y. et al synthesized unique indigo-RGO/WO_3 nanoomposites to increase the visible light absorption which is more favorable for improved photocatalytic performance. The photocatalytic efficiency of as-prepared sample was carried out at different pH values as well as catalyst contents. The experimental result reveal that the 30mg catalyst showed highest degradation efficiency at pH=11 [110]. Hu, X et al fabricated the WO_3/GRx (x = 0.1, 0.5, and 1) nanocomposites by incorporating the wo3 nanorods over graphene sheets via hydrothermal process. The photocatalytic properties of synthesized material were carried out by decomposition of organic dye (methylene blue) under visible light illumination. From obtained results, they analyzed that the 1% WO_3/GR nanocomposite showed better degradation efficiency (83%) than pure WO_3 due to large interfacial contact area and wide visible light absorption range that cause to increase transferring rate [111]. Nugraha, M. W. et al Fabricated WO_3/N-CQDs (carbon quantum dots derived from sugarcane) composites with varying quantity of N-CQDs. The found that the anchoring of N-CQDs on the surface of WO_3 leads to large surface area, low band gap and high crystallinity of WO_3. The catalytic properties of as-prepared samples were detected by removal rate of dye (MB) under visible light irradiation. Thus, the increased visible light harvesting efficiency owing to low band gap cause to enhance the photocatalytic activity towards MB. The experimental result indicates that the 2.5%WO_3/N-CQDs nanocomposite displayed higher photocatalytic performance (96.8%) as well as photo stability and reusability [112]. Li, G. et al designed z-scheme WO_3/MoS_2-rGO ternary nanocomposite to improve photo catalytic efficiency. The WO_3/MoS_2-rGO with 10% mass fraction of MoS_2-rGO exhibited superior removal rate of rhodamine B than other prepared samples (WO_3/MoS_2 and WO_3). They also found that the holes and hydroxyl are the main active species to degrade the dye under visible light during chemical reaction through radial trapped experiment [113]. Zhi, L. et al designed unique hollow hierarchical flower like structure of AgI/WO_3 z-scheme photocatalyst by decorating 3D WO_3 hollow nano-flowers with AgI NPs to boost the light harvesting efficiency. Their photocatalytic efficiency was tested by removal of Eosin B and tetracycline hydrochloride from aqueous solution under LED lamp (5W). They observed that AgI/WO_3 hollow hierarchical nanoflower displayed remarkable photocatalytic efficiency as well as photo-stability than pure 3D WO_3 hollow flowers, AgI NPs and AgI/WO_3 nanosheets. This is attributed that the high light absorption efficiency and z-scheme coupled hetero-interface junction are the main factors to effectively improve the transferring rate of charge carriers [114].

The development z-scheme graphene base photocatalyst effectively enhance the photo degradation efficiency. In my publication –II, I have synthesized N-doped graphene modified WO_3 Z-scheme photocatalyst to boost the photocatalytic activity towards the mixture of strong pollutants (MO and 2, 4 DCP) in the presence of visible light source.

2.2.3 Magnesium Oxide (MgO)

Zheng, Y. et al evaluate the photocatalytic efficiency of MgO micro-particles with flower like structure to decomposing the different organic dyes such as Congo red, eriochrome black T, methylene blue, bromothymol blue and their mixture under UV light source [115]. Mageshwari, K et al prepared hierarchical MgO with coral-like nanostructure to improve the photo-catalytic performance. They performed photocatalytic experiment on the organic dye (MO) to investigate the photocatalytic efficiency of as-synthesized sample and observed that sample exhibit good degradation efficiency towards MO due to porous structure and large surface area [116]. Taourati, R. et al investigate the photocatalytic property of MgO NPs employing the degradation reaction of Alizarin red S. The experimental results demonstrate that the MgO displayed higher photocatalytic efficiency (80%) as well as good stability under UV light illumination [117]. Khan, M. I. et al synthesized MgO NPs with band gap (4.17eV) via ecofriendly green approach. The band gap value effectively the enhance photocatalytic properties of MgO by decomposition the MB under UV light [118].

Bandara et al prepared TiO2/MgO nano-porous structure in which MgO layer act as an electron sink and barrier to retard the recombination rate cause to boost the photo catalytic performance of TiO_2 for oxidation of 2,4-dichlorophenol, 2-chlorophenol and 4-aminobenzoic. Besides, the observed that the thickness of MgO layer strong effect the degradation efficiency of TiO_2 [119]. Nga, N. K et al have investigated the photo catalytic activity of chitosan/MgO nanoomposites by detoxifying the RB (reactive blue) 19 pollutant. They observed that chitosan/MgO exhibited good photo catalytic performance against RB (reactive blue) 19 pollutant than pristine MgO [120].

In my present work, I have synthesized binary 2D/2D MgO@G and ternary CQDs/MgO@G nanocomposites were synthesized to remarkably tune the band gap of MgO with increase massive active sites and large surface area which was more favorable for photocatalytic activity. The ternary CQDs/MgO@G photocatalyst showed excellent degradation efficiency towards pollutant under visible light due to strong interfacial coupling.

CHAPTER 3

3.1 Experimental methods

3.1.1 Sol gel method

It is wet chemical method to synthesize the high-quality nanomaterials. In this method, the liquid precursor changed into **sol**, and it further transformed into network structure called **gel**. The precursor used in this method are metal alkoxides. There are following basic steps involved in the fabrication of nanomaterials. (i) Sol is formed through the hydrolysis of metal oxide occur in water. (ii) **Condensation,** which leads to formation of porous structure due to increase in solvent viscosity. Moreover, Oxo- (M–O–M), hydroxo- (M–OH–M) bridges create, causing formation of metal–oxo-polymer or metal–hydroxo- during condensation process. (iii) After that, **aging** take place in which distance between colloidal particles increased and porosity decrease. Lastly, gel undergo drying and calcination to remove the organic solvent and water from gel and obtained desire product [121].

3.1.2 Hydrothermal

Hydrothermal is an effective and low-cost technique to synthesize the nanomaterials. The hydro mean "water" and thermal mean "heat" [122]. High temperature is required for hydrothermal process. Two basic steps (i) crystal nucleation and (ii) subsequent growth involved in the fabrication of nanomaterial. The desire size and morphology of product can be obtained by controlling the various parameters such as pH, pressure, additives, temperature, and amount of reactant [123,124].

3.2 Characterization techniques

3.2.1 X-ray diffraction

The crystallinity, phase, purity, orientation, lattice parameters and size of nanomaterial is determined by X-ray diffraction (XRD) [125]. This technique based on the Bragg's law. To analyze the crystal structure of sample, the X-rays fall on the sample that scattered through each atom within the sample. If these scattered X-rays (from atomic plane) are in-phase, resulting constructive interference and get maximum intensity at specific angle. The inter planner spacing was calculated using Bragg's law: $2d \sin \theta = n \lambda$. Besides, the size of crystalline material was determined by Debye-Scherrer's formula as give below.

$$D = K \lambda / \beta \cos\theta \qquad (3.1)$$

Here, k is sheerer constant, β represents full width half maximum [FWHM] and λ is wavelength of x-rays [126,127].

3.2.2 Scanning electron microscope (SEM)

The scanning electron microscope instrument used high energy electron beam to scan the surface of specimen. When electron beam is fall on the surface of specimen, three kinds of electrons (such as secondary electrons, backscattered electrons, and auger electrons) are emitted with X-rays. Basically, secondary, and backscattered electrons play an important role to scan the specimen. Elastic scattering of electrons after reflecting from the specimen produced backscattered electrons. Whereas secondary electrons are originated from the atoms of specimen. They are result of inelastic collision between sample and electron beam. Secondary and backscattered electrons come from surface and deeper surface of the specimen, respectively. Subsequently, Backscattered, and secondary electrons provide different information: Backscattered electrons provide the detail of the atomic number. While the secondary electrons are responsible to produce high-resolution images in the range of 1-5nm and X-rays are used identify the composition of element using EDX technique [125,128].

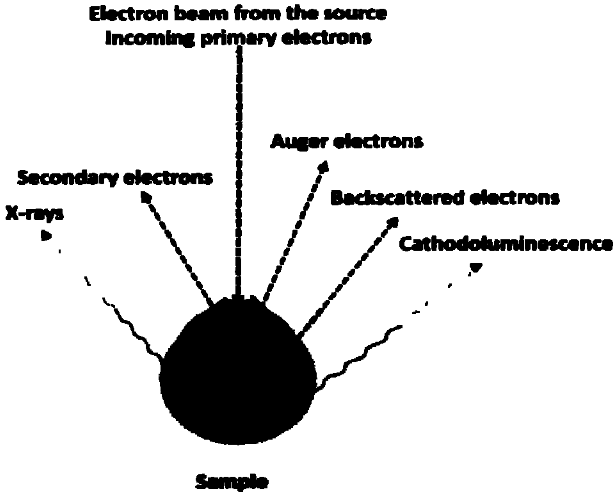

Figure. 3.1: Basic principle of SEM [129]

3.2.3 Energy dispersive X-ray

This technique is used for both quantitative and qualitative analysis to identify the chemical and elemental composition of the prepared sample. For this purpose, SEM instrument fitted with an x-ray detector is used to excite the atoms within a sample through high energy electron beam. When high energy beam is strike to the inner shell of the atom, displace an electron from the shell leaving behind the holes. To fill the vacancy, the electron from higher energy level is move towards the lower energy level by emitting the specific energy called x-rays (fig.3.2) and are detected by x-ray detector. The emitted x-rays have unique energy corresponding to the element. Therefore, these X-rays are used to identify elements present within the prepared sample.

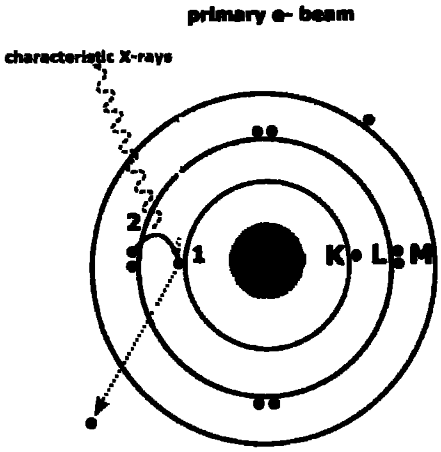

Figure. 3.2: Schematic illustration of EDX [130]

3.2.4 Transmission electron microscope (TEM)

The nanomaterial's size and its distribution are an important parameter for its applications in various fields. TEM technique is very useful to examine the size of nanomaterials. An electron beam produced by heating tungsten filament is focused on sample via condenser lenses. The focused electron beam strike with sample and transmitted through it. These transmitted electrons focused on the florescence screen by protective lens to form a clear image (as shown in fig.3.3). Moreover, the bright and dark area on the TEM images is shown which indicate the concentration of transmitted electrons. Denser sample exhibits dark area because more electrons are scattered as compared to thinner [131].

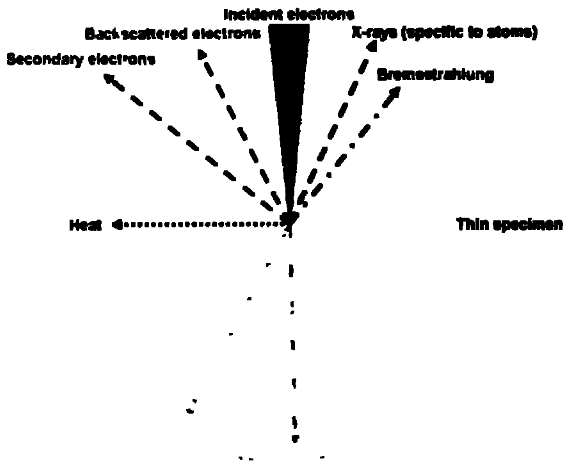

Figure. 3.3: Basic principle of TEM [132]

3.2.5 Fourier transform infrared spectrometer (FTIR)

The structure and chemical bonding of synthesized sample was identified using Fourier transform infrared spectrometer in the range of 4000-400cm^{-1}. The basic principle of FTIR is based on the Michelson interferometer. A light beam having different IR wavelength is passed via beam splitter (fig 3.4), where it partially reaches at movable mirror and rest of light beam at mixed mirror. These two reflected beams combine, resulting to construct an interference phenomenon. Then, this interferogram is sent to the sample, and its transmitted part is transferred to a detector. A detector detects the intensity of reflected or transmitted light in the form of wavelength.

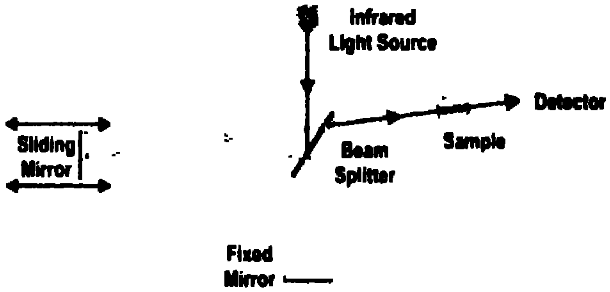

Figure. 3.4: schematic diagram of FTIR instrument [133]

3.2.6 Raman spectroscopy

The detailed information about phase, crystallinity and molecular interaction of prepared sample is examined by nondestructive technique known as Raman spectroscopy. Fig.3.5 depicts that the Raman spectroscopy based on the interaction between molecular bonding within the sample and incident light. When the sample is exposed by light, it interacts with molecules in many ways, some part of light reflects or undergo Raleigh scattering (elastic scattering), as a result emitting the same wavelength as incident light. If incoming light cause the vibrational oscillation within molecules is called inelastic scattering. Fluorescence take place, if the incident light has energy equal to the electronic energy level of the molecule, causing the excitation and de-excitation resulting the emission of longer wavelength than incident light. Stoke scattering occur when the molecules absorbed energy and emit the photon having shorter wavelength as compared to incident and in the case of anti-stoke scattering, the molecule within sample is already in vibrational exit estate, and transfer energy to scattered photon during vibrational de-excitation process. All these types of scattering provide detailed information about composition of prepared sample [134].

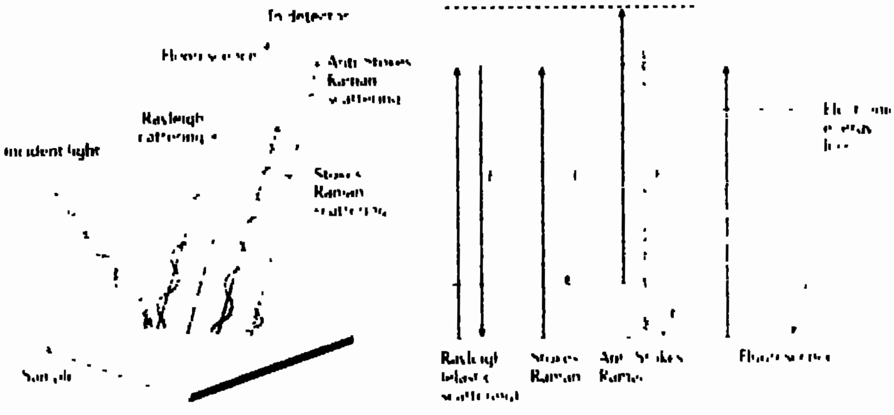

Figure.3.5: Possible interaction in Raman spectra [135]

3.2.7 Photoluminescence (PL)

This nondestructive technique is very useful to analyze the electronic structure of synthesized materials. When the sample is illuminated by incident light, it absorbed the energy and excites the electrons into allowed excited states. These electrons turn back to their stable equilibrium state by emitting energy in the form of photons known as non-radiative or radiative process as shown in fig.3.6. The emitted photon energy match with energy difference between two electronic states that participate in transition between equilibrium and exited state. Therefore, the PL spectrum is associated with concentration of non-radiative and radiative recombination rate. The non-radiatives are related to the impurities. Thus, the PL spectrum also reveals the peaks of impurities that strongly affect the quality of host material [126].

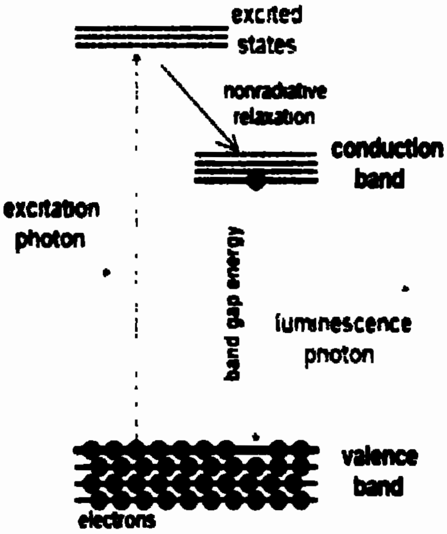

Figure.3.6: Schematic illustration of PL [136]

3.2.8 X-ray Photoelectron spectroscopy (XPS)

XPS studies provide information about elemental composition and electronic and chemical state of elements present in synthesized sample. XPS spectrum attained by photoelectrons released from sample when the impinging photons energy exceed than the binding energy of electrons. Kinetic energy of photoelectrons is depending on the binding energy of each electron (equation 3.2). Because, atom consist of various orbitals having different states, causing to produce numerous photoelectrons with different binding energies.

$$E_{k.e} = E_{photon} - E_{binding} - \varphi \qquad (3.2)$$

Here, φ, E_{photon} $E_{k.e}$, $E_{binding}$ represents the work function, incident photon energy, kinetic and binding energy of the photoelectron respectively.

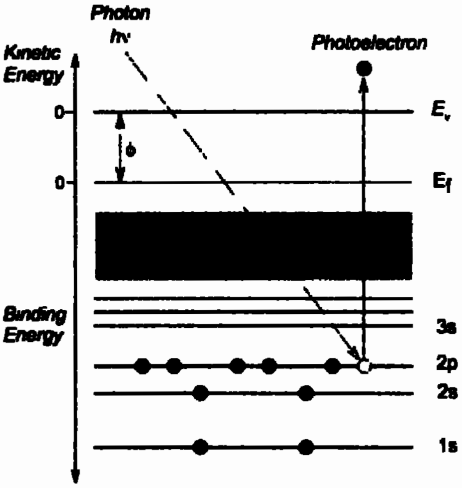

Figure. 3.7: Basic mechanism involved in XPS

3.2.9 UV- vis spectroscopy

This technique is used to study the optical properties related to band gap of synthesized material. An absorption spectrum can be observed when the monochromatic light is exposed on the synthesized material, the energy absorbed by material corresponds to the energy level cause to transfer the electron to a higher energy state. Generally, three kinds of electrons (nonbonding 'n', sigma and pi-electrons) exist in molecules absorbed light irradiation to migrate these electrons into higher state (anti-bonding). There are four possible electronic transitions: n–σ*, n–π*, σ–σ*, and π–π* as shown in fig.3.8. The absorption spectrum is obtained by absorbed light irradiation.

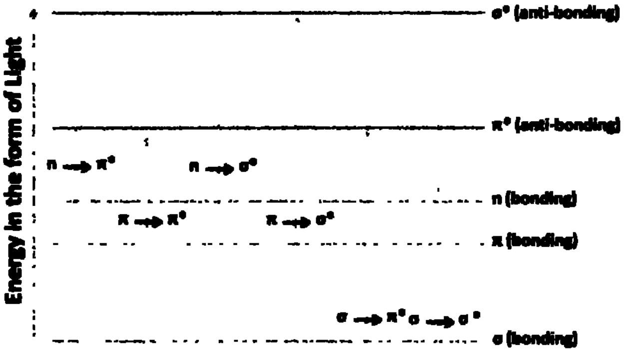

Figure.3.8: Basic mehanism involves in UV-vis spectroscopy [137]

3.2.10 Cyclic voltammetry

To study the electron transferring in redox active medium is determined by an effective technique known as cyclic voltammetry. It consists of three types of electrodes: counter electrode, working electrode and reference electrode. To perform this experiment, first the electrolyte solution is kept in the electrochemical cell associated with reference solution and electrodes. Then the potential is linearly sweep between the reference and working electrode using potentiao-state until it reach at a specific point, after that it's again sweep in reverse direction (clearly seen in fig.3.9). Subsequently, the changing current is measured at counter electrode.

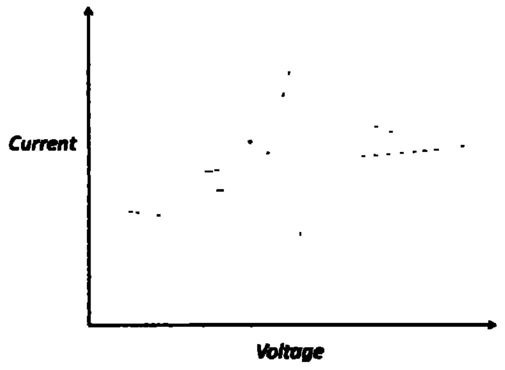

Figure.3.9: Graphial representation of cyclic voltammetry [138]

3.2.11 Photocatalytic degradation of pollutants

The photo-degradation of pollutant was performed using photo-reactor under visible light irradiation. Water circulating jacket was used to release the heat of lamp and keep the temperature constant (fig.3.10). To carry out the photocatalytic activity, the optimum amount of photocatalyst was dissolved into dye solution under continuous stirring. Before visible light irradiation, the suspended solution kept in dark to attain adsorption-desorption equilibrium. Later, this solution placed in the photo-reactor in dark region to proceed the photocatalytic performance. After regular time interval, 5ml sample was drawn from photo-reactor and centrifuge the solution to remove photocatalyst's suspension. Finally, the obtained solution was evaluated by UV-vis absorption spectrum to investigate the degradation efficiency. The degradation efficiency was determined using this relation.

$$\text{Photo-degradation } \% = (C_o - C)/C_o \times 100 \qquad (3.3)$$

Here, C_o and C represents the concentration of pollutants before and after visible light irradiation, respectively. Moreover, Langmuir – Hinshelwood Kinetic model is used to kinetic study of photocatalyst for photo-degration of pollutants [139].

$$\ln C_0/C = kt \tag{3.4}$$

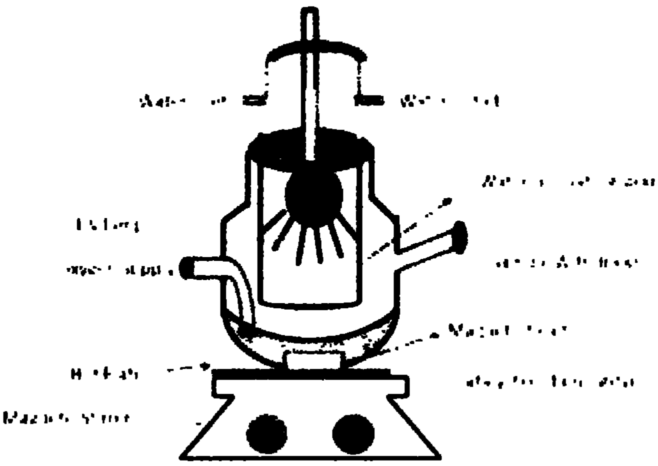

Figure.3.10: Assembly illustration of Photocatalytic activity

CHAPTER 4

Interfacial charge transfer via 2D-NiO and 2D-graphene nanosheets combination for significant visible photocatalysis

4.1. Introduction

Environmental technology and science are facing some serious issues based on increasing water and air pollution [140]. Many pollutants (heavy metals, dyes etc.) is produced due to industrial effluent which intensely effect environmental and aquatic life while their hostile effect depends on their complex molecular structure [141, 142]. It is crucial to develop an effective technique to tackle these intricate environmental problems. Photocatalytic degradation is most efficient technique to deal with environmental challenges (to eradicate the hazardous contaminations from environment) and sustainability with light irradiation [104, 143]. In photocatalytic process, excited electrons move from valence to conduction band of semiconductor materials to generate electron (e^-)–hole (h^+) pairs under light irradiation. These photoexcited charge carriers are responsible for oxidation reduction process with oxygen and water to degrade the organic pollutants and subsequently mineralize it to CO_2 and H_2O [144,145].

2D nanomaterials have been gaining tremendous attention in environmental remediation owing to their fascinating physiochemical properties like mechanical flexibility, large specific surface area and numerous active sites on their surface etc. [146,147]. Among various 2D materials, NiO (P-type semiconductor) possesses excellent conductance feature, low cost, elevated chemical, and long-term catalytic stability which make it appropriate as photocatalyst under visible light irradiation [148,149]. However, quick recombination of charge carriers, minimum harvesting of light, less selective absorption etc. are the considerable major limitations of NiO semiconductor to impend photocatalytic performance [150]. To overcome these obstacles, literature have shown that 2D-2D heterostructures endow electronic coupling and enhanced interfacial contact area between them. Thus, the physical and electronic coupling effect between semiconductor sheets and graphene is favorable to increase the transportation rate of electron/hole pairs and boost the photocatalytic efficiency [151-153]. Because highly conductive graphene sheet acts as an electron acceptor for shuttling electrons due to delocalized electronic network over the carbon sheets, leading to an effective charge separation rate at junction interface [154]. Recently, Sun *et al.* demonstrated that fabrication of 2D-2D $BiVO_4$/reduced graphene sheets via solvothermal method exhibited high photocatalytic efficiency as compared to 1D-2D and 0D-2D heterojunctions. The results clearly indicate the fast electrons shuttling in 2D-2D $BiVO_4$/ reduced graphene sheets at interfacial junction, leading to augment the separation rate of charge carriers and enhance photocatalytic efficiency [155]. Therefore, synthesis of novel 2D-2D semiconductor with graphene sheet bestows an effective way to overcome the limitation of charge carrier's transfer.

In present work, NiO nanosheets and 2D-2D graphene/NiO nanocomposite with different graphene concentration were prepared via co-precipitation and wet impregnation method. To the best of our knowledge, NiO nanosheets have been interacted with 2D graphene sheets for the first time to boost the photocatalytic efficiency. As-prepared graphene/NiO nanocomposites exhibit high surface photocatalytic rate than pure NiO towards the methyl orange under visible light. This improved photocatalytic efficiency can be attributed to the 2D/2D surface morphology associated with graphene and NiO sheets and intimate interfacial coupling between them, which effectively increased the separation and transferring rate of charge carriers. Therefore, this present work endows an avenue to synthesize numerous 2D-2D semiconductor/graphene hybrid structures which can be effectively used in photocatalytic applications.

4.2. Experimental

4.2.1. Materials

Nickel chloride, graphite power, sulfuric acid, hydrochloric acid, potassium permanganate, hydrogen peroxide, ammonia solution and methyl orange (MO) are purchased from Sigma-Aldrich. All these solution and reactants are used to synthesize materials without further purification.

4.2.2. Synthesis of graphene oxide

GO was prepared via modified hummer's method [156]. Expanded graphite (2.5 g) and conc. H_2SO_4 (98%, 65.0 mL) were mixed under continuous stirring to get homogenous solution. $KMnO_4$ (5.0 g) was gradually added into above solution, the temperature was sustained below 4 °C using ice bath. As liquid paste was formed, Ice bath was removed and further stirred for 3 hours. Subsequently, deionized water (200 mL) was mixed to dilute this solution and heated at 90 °C for 2 hrs under water bath. After that, the mixture was cooled at room temperature to add (7.5 mL) H_2O_2 drop wise. Due to this, the color of solution is changed to yellow. Finally, the prepared particles were separated through centrifugation at speed of 6000 rpm. Furthermore, the material was washed with 1M hydrochloric acid to eliminate the residual contaminants and with distilled water to set the pH=7. Subsequently, particles were sonicated and dried in oven at 60 °C to obtained final product (graphene oxide). The graphene oxide successfully converted into graphene sheets by using chemical reducing agent (NaOH).

4.2.3. Synthesis of NiO

The 2D-nanosheets of NiO were synthesized by co-precipitation method. Initially, 4.0 g nickel chloride was dissolved into 150 mL distilled water under constant stirring (Eq.1). Aqueous ammonia (10 mL) was added into above solution, green precipitates of Ni $(OH)_2$ nanosheets were formed because pH deeply effect the morphology of sample. Adding ammonia solution (to adjust pH of solution), the weak alkaline solution is obtained which gives hydroxide ions for fabrication of Ni $(OH)_2$ (Eq. 4.2-4.5). NH_3 act as complex reagent for Ni^{2+} ions to produce Ni $(NH_3)_6^{2+}$ which play a significant role for formation of Ni (OH) nanosheets by controlling the reaction of Ni^{2+} with OH^- as given in equations [157,158]. The obtained precipitates Ni $(OH)_2$ were segregated by centrifugation and washed with deionized water to eliminate the impurities, and dried at 60 °C. After that, the prepared Ni $(OH)_2$ nanosheets changed into NiO nanosheets (Eq. 4.6) by annealing it at high temperature (400 °C) to make sure the removal of hydroxide phase that may exist in primary layer of NiO [159].

$$NiCl.6H_2O + H_2O \longleftrightarrow Ni\,(OH)_2 + HCl + 5H_2O \qquad (4.1)$$

$$Ni\,(OH)_2 + 6NH_4(OH) \longleftrightarrow [Ni(NH_3)_6]^{2+} + 6H_2O + 2OH^- \qquad (4.2)$$

$$[Ni\,(NH_3)_6]^{2+} \longleftrightarrow Ni^{2+} + 6NH_3 \qquad (4.3)$$

$$6NH_3 + H_2O \longleftrightarrow 6NH_4\,(OH) \qquad (4.4)$$

$$Ni^{2+} + 2OH^- \longleftrightarrow Ni\,(OH)_2 \qquad (4.5)$$

$$Ni\,(OH)_2 \xrightarrow{\text{annealing}} NiO + H_2O \qquad (4.6)$$

4.2.4. Preparation of 2D-2D graphene/NiO composites

For surface modification, graphene/NiO nanocomposites were fabricated by wet impregnating method. 1.0 g of NiO was mixed in 50 mL distilled water under constant stirring to attain well dispersed and homogeneous solution. At the same time, 0.03 g of graphene was dissolved in 50 mL distilled water under continuous stirring. Then, graphene solution was gradually added into NiO suspension. After that, solution was dried at 60 °C in oven to attain the 3.0% graphene/NiO (2D-2D) nanocomposite. Various graphene mass contents were used to gain 5.0% and 10.0 % 2D-2D graphene/NiO nanocomposites by same procedure. The fabrication procedure of 2D-2D graphene/NiO nanocomposite is illustrated in Figure 4.1.

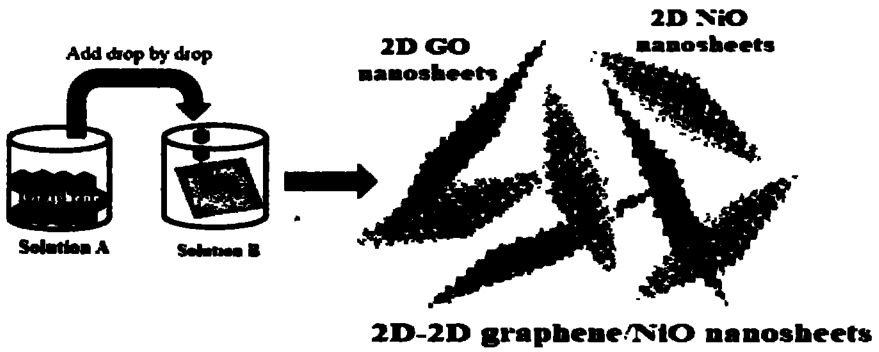

Figure 4.1. The synthesis method for 2D-2D graphene/NiO nanocomposite photocatalyst

4.2.5. Experimental set-up and measurement of photocatalytic activities

Photocatalytic activity of pure graphene, NiO and graphene/NiO nanocomposites with various percentages were examined under visible light using methyl orange as a dye. Degradation process was performed in quartz photochemical reactor. 1000 W tungsten lamp is used to carry out the photocatalytic activity. During the reaction, the temperature of mixture was sustained by cooling the water jacked photochemical reactor through water cooling system. Initially, (50.0 mg) sample was added into 50 mL dye solution. This solution was placed in dark for half an hour under stirring to acquire desorption-adsorption of MO dye and sample. Afterward, the solution was kept before lamp with fixed distance of 10 cm and irradiated by visible light for various time interval. After regular time internal, solution was drawn and centrifuged to segregate the samples for degradation analysis. The degradation experiment of synthesized photocatalysts were performed two times for accuracy and errors to omit.

4.2.6. Catalyst characterization

The crystalline properties of prepared materials were examined using Rigaku D/Max diffractrometer (Cu kα irradiation, wavelength =1.5A°) operated at 40 KV and 100 mA. Fluorescence spectrometer (Perkin Elemer LS-50B) was used to study the PL spectra of synthesized samples. The elemental composition and surface morphology were investigated through EDS and SEM (JEOL-JAD 2300), respectively. FTIR was employed to explore the chemical bonding of samples by Fourier transform spectrometer Bruker FTIR ALPHA II. Shimadzu (2700) spectrophotometer was used to obtain the UV-Vis absorbance spectra of samples. Raman spectra of NiO sheets and 2D-2D graphene/NiO nanocomposite were obtained using Raman spectrometer with excitation wavelength of 633 nm by Horiba Labram-HR 800.

4.3. Results and discussion

4.3.1 XRD analysis

The crystalline properties of synthesized samples were analyzed by XRD. Fig. 4.2A exhibits the XRD pattern of synthesized GO. The strong and sharp peak appeared at 10.8° is ascribed to the (001) plane of graphene oxide with lattice constant 0.82 nm. This indicates that the graphite was completely oxidized to become graphene oxide [160]. Further, Fig. 4.2B (a-e) exhibits the XRD pattern of graphene nanosheet, NiO and various 2D-2D graphene/NiO composites. In Fig. 4.2B (a), a broad diffraction peak $2\theta = 26.2°$ with lattice constant 0.34 nm was observed which represent the complete conversion of GO into graphene [161]. Figure 4.2B (b) exhibits the diffraction peaks at $2\theta = 37.07°$, 43.08°, 62.79°, 75.21° and 79.41° which are assigned to the (111), (200), (220), (311) and (222) planes of crystalline nickel oxide (well matched with standard JCPDS card (65-2901)) [162, 163]. The average crystalline size of NiO was determined through Scherrer formula is found to be around 4.25 nm [164]. It has been shown in Fig. 4.2B (b-e) that pure NiO and graphene/NiO nanocomposites have almost identical characteristic diffraction peaks. No characteristic peak of graphene sheets at $2\theta = 26°$ was observed. This may be owing to low concentration of graphene than NiO. Thus, NiO could restrain the restacking of graphene sheets [165].

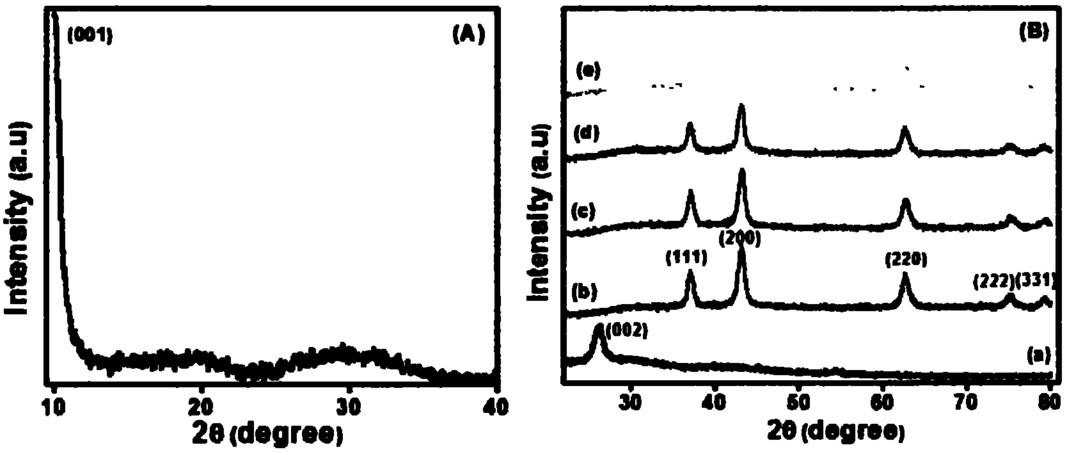

Figure 4.2. XRD pattern of (A) GO, (B) XRD pattern of (a) graphene sheets (b) pure NiO nanosheets, (c) 3.0 %, (d) 5.0% and (e) 10.0 % graphene/NiO nanocomposites, respectively.

4.3.2. Fourier transform infrared spectroscopy (FTIR)

The presence of functional group of graphene sheets and 2D-2D graphene/NiO composite were identified by FTIR. Figure 4.3 (a-c) exhibits the FTIR spectra of graphene, NiO and graphene/NiO nanocomposite. The band assignment of each vibrational mode observed are presented in Table

4.1. In Fig. 4.3 (a), peaks are observed at 1280 cm^{-1} and 1100 cm^{-1} which ascribed to the stretching vibration of C-O-C and C-C, respectively. Other bonds related to oxygen functional groups were almost eliminated. Specially, the bond associated with sp^2 hybridized stretching vibration of carbonyl functionality (-C=O) was totally removed. This shows the successful removal of carboxylic and carbonyl groups along with other oxygen functional groups from basal plane and edges of hexagonal graphene structure [166, 167]. In Fig. 4.3(b), FTIR spectrum of NiO nanosheets exhibits the peaks at 950 cm^{-1} which correspond to CN$^+$ stretching. Moreover, the bond around 400-600 cm^{-1} is ascribed to metal-oxygen vibrational bonds. The peak at 545 cm^{-1} is related to the Ni-O bond [148, 168, 169]. Extra absorbance peak observed in Fig. 4.3(c) at 1545 cm^{-1} due to skeleton vibration of graphene sheets [1670] reveals the successful fabrication of graphene/NiO nanocomposite.

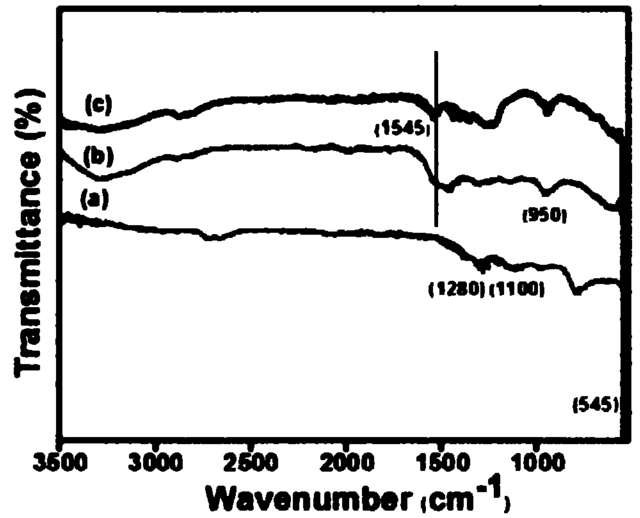

Figure 4.3. FTIR spectra of pure and composite samples; (a) graphene sheets, (b) NiO nanosheets and (c) graphene/NiO nanocomposite.

Table 4.1. FT-IR absorption band for functional group of graphene sheets, NiO and graphene/NiO nanocomposite.

Samples			**Band Assignments**	**Refrences**
Graphene sheets	NiO nanosheets	Graphene/NiO nanocomposite		
1100 cm^{-1}	-	-	C-C stretching vibration	[166-167]
1280 cm^{-1}	-	-	C-O-C stretching vibration	[166]
-	950 cm^{-1}	950 cm^{-1}	CN^{+} stretching	[148]
-	545 cm^{-1}	545 cm^{-1}	Peak related to Ni-O bond	[168-169]
-	-	1545 cm^{-1}	Skeleton vibration of graphene sheets	[170]

4.3.3. Scanning electron microscope (SEM)

The surface morphologies of NiO, graphene sheets and graphene/NiO composites were analyzed by SEM. Nickel oxide also exhibit sheets like morphology (indiated by red lines) as shown in Fig. 4.4 (a, b) (average thickness 16 nm). Thin and highly transparent graphene sheets (thickness 12 nm) with crumpled and folded edge can clearly be seen in Fig. 4.4 (c). In Fig. 4.4 (d-e), graphene/NiO composite displays diverse morphology on account of good mixing integrity of graphene and NiO sheets, which promotes the intimate interfacial coupling between them to expose the more active sites for utmost adsorption of dye molecules to boost the photocatalytic activity [171, 172].

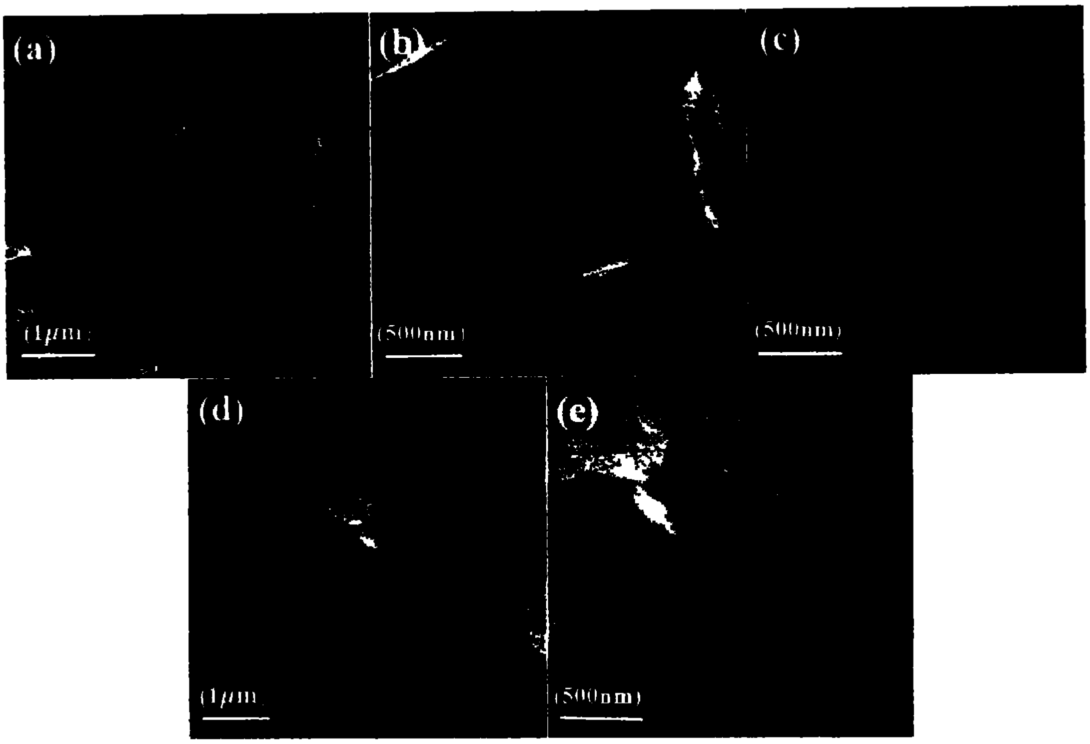

Figure. 4.4 SEM images of pure and composite samples; (a-b) NiO nanosheets (c) graphene sheets (d-e) graphene/NiO nanocomposite (10.0%)

4.3.4. Energy dispersive X-ray spectroscopy (EDS)

The EDS spectra of NiO and 10.0% graphene/NiO nanocomposite are shown in Fig. 4.5. Fig. 5(a) exhibits the existence of nickel (Ni) and oxygen (O) that suggests formation of NiO sheets with no obvious impurity. In Figure 4.5(b), 10.0% graphene/NiO nanocomposite displays the presence of Ni, O and C without any impurity. The signals for Ni, O and C are originated from nickel oxide and graphene sheets, respectively. Hence it indicates the formation of graphene/NiO nanocomposite with purity. The composition of NiO sheets and graphene/NiO nanocomposite is preesented in Table 4.2.

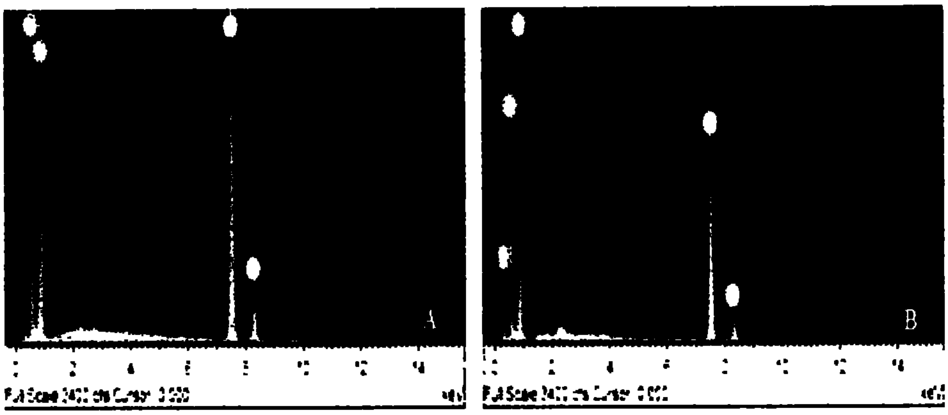

Figure 4.5. EDS of pure NiO (a) and 10.0% graphene/NiO composite (b).

Table.4.2. Elemental chemical analysis (atomic and weight %) of NiO sheets and graphene/NiO nanocomposite calculated by EDS.

Photo catalysts	**Atomic %**			**Weight %**		
	Ni	O	C	Ni	O	C
NiO	48.46	51.54	0	77.53	22.47	0
Graphene/NiO nanocomposite	40.03	20.55	40.03	55.99	30.60	13.41

4.3.5. UV-Vis absorption spectra

The optical properties of materials are associated with band gap energies which are ascertained by UV-Vis spectroscopy. Figure 4.6 exhibits the absorption spectra of NiO and graphene/NiO nanocomposites over the range of 275-700 nm. Pure NiO displays its characteristic absorption edge around 450 nm (Fig. 4.6A). It could be obviously examined that when the graphene sheets are incorporated into NiO nanosheets, the absorption edges of composites are slightly shifted towards longer wavelength (red shift). This indicates the significant reduction in band gap energies. The band gaps of NiO, graphene/NiO (5.0%) and graphene/NiO (10.0%) are calculated through Tauc's plot using mathematical relation [173]

$$(\alpha h\nu)^n = A\,(h\nu - E_g) \;\ldots\ldots\ldots\ldots\ldots\ldots\ldots\ldots (4.7)$$

Here α (absorption co-efficient), A (constant), hv (photon energy), E_g (band gap energy) and n is a parameter whose value is either 2 or 0.5 for direct and indirect transition, respectively [174]. The band gaps of pure NiO and graphene/NiO (5.0 %) and graphene/NiO (10.0 %) composites are found to be 3.3, 2.9 and 2.3 eV, respectively. This shows an effective reduction with incorporation of graphene sheets owing to the defect states between valence and conduction band of NiO [175]. These results imply the significantly reduced band gap energy to boost the effective utilization of solar irradiation which is favorable for enhanced photocatalytic activity.

By using calculated band gap value of NiO from UV-Vis spectra, the edge positions of valence and conduction band of NiO were estimated using following equations;

$$E_{VB} = X - E_e + 0.5\,E_g \quad \ldots\ldots\ldots\ldots\ldots (4.8)$$

$$E_{CB} = E_{VB} - E_g \quad \ldots\ldots\ldots\ldots (4.9)$$

Where E_e is free electron energy (4.5 eV) and X is electronegativity of NiO calculated using the equation.

$$X = [X(A)^k * X(B)^l]^{1/(k+l)} \quad \ldots\ldots\ldots (4.10)$$

The value of E_g and X for NiO 3.3 and 5.75 eV, respectively. The E_{CB} and E_{VB} of NiO were determined to be -0.4eV/NHE and +2.9 eV/NHE while -0.08eV/NHE is the Fermi level of graphene sheets (well matched with literature) [176-178]. The corresponding band alignment of 2D-2D graphene/NiO nanocomposite is shown in Fig. 4.6 (D). Consequently, the acquired results are used for transferring of charge carriers in nanocomposite (2D-2D graphene/NiO) which illustrate the photocatalytic process.

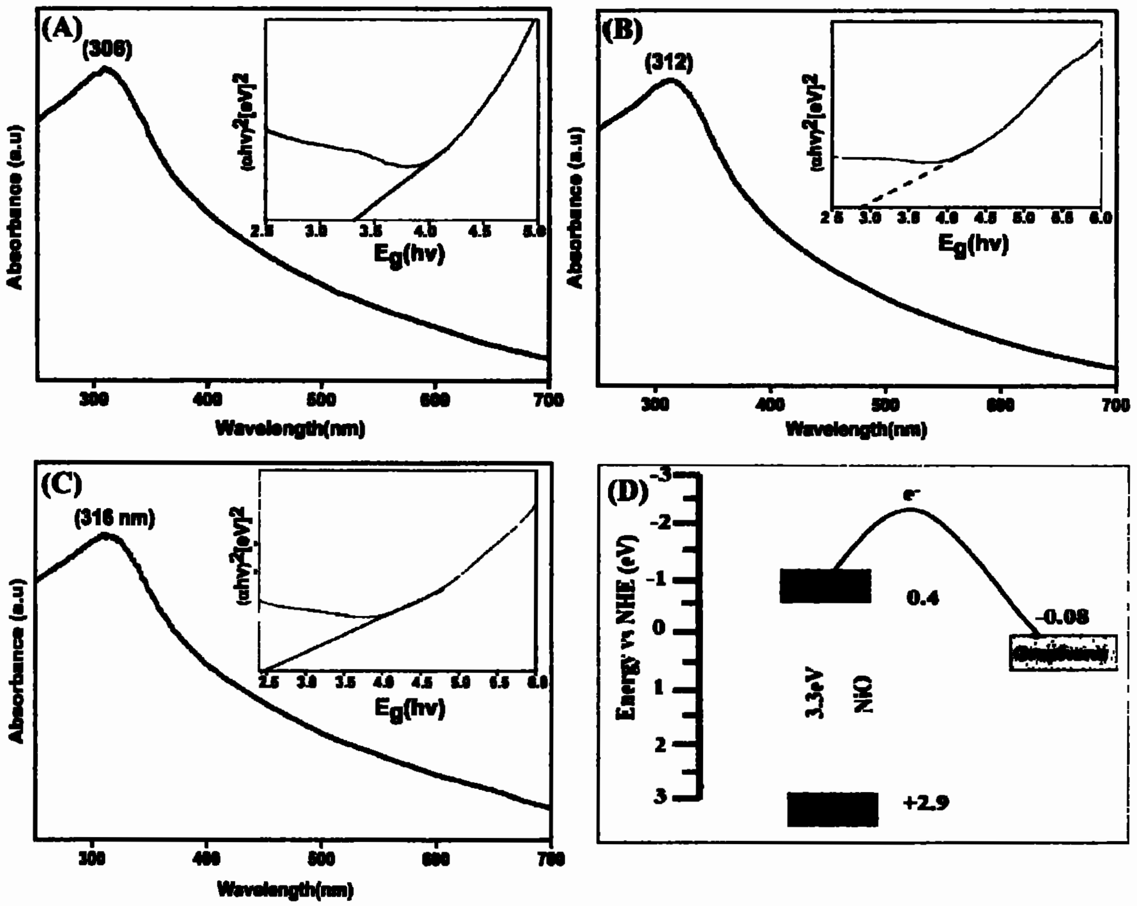

Figure 4.6. Optical absorption spectra (Inset showing band gap energy) of pure and various composites; (A) pure NiO nanosheets, (B) graphene/NiO nanocomposite (5.0%), (C) graphene/NiO nanocomposite (10.0%) and (D) Energy band diagram of graphene/NiO nanocomposite.

4.3.6. Raman spectroscopy

The interaction between 2D-2D graphene/NiO nanocomposites was evaluated by Raman spectroscopy as shown in Fig 4.7. Fig. 4.7(a) exhibits the peaks at 545 cm^{-1} and 1052 cm^{-1} corresponding to phonon scattering of first and second order in 2D pure NiO [179]. In 2D-2D graphene/NiO nanocomposite, two extra peaks are observed at about 1345 cm^{-1} and 1598 cm^{-1}

credited to the "D" and "G" band, respectively as shown in Fig. 4.7(b). The stretching of sp^2 carbon resulted into "G" band is associated with networks owing to E_{2g} vibration mode while "D" band represents the defects present in two-dimensional hexagonal lattice [180]. It is noteworthy that D band and G band in 2D-2D graphene/NiO nanocomposite confirms the chemical doping of graphene sheets in 2D NiO.

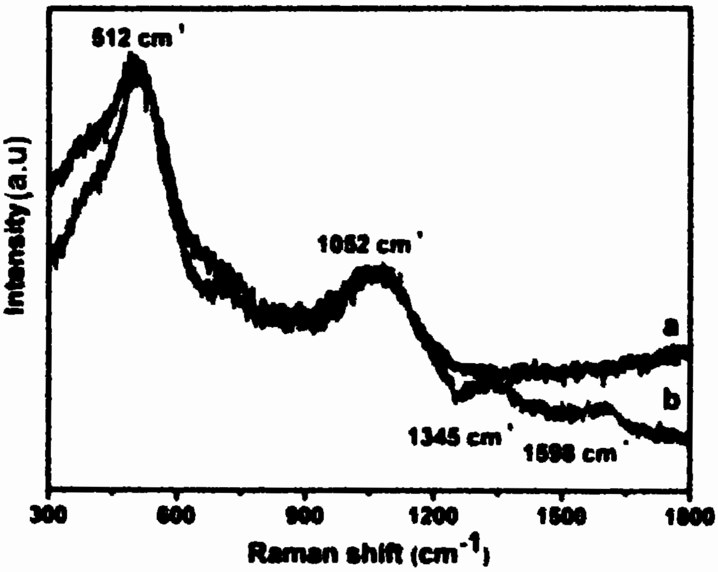

Figure 4.7. Raman spectra of pure and composite sample; (a) pure NiO nanosheets (b) 10.0% graphene/NiO nanocomposite

4.3.7. Photoluminescence spectroscopy

Photoluminescence technique was used to examine the recombination rate and transfer of charge carriers. Fig.4.8 depicts the Photoluminescence spectra of NiO nanosheets and 10.0% graphene/NiO nanocomposite in the range of (300-650 nm) using an excited wavelength (280 nm). The peak intensity reveals the charge carriers' recombination rate [181]. In Fig. 4.8 (a), the pure NiO shows an intense peak which appeared at about 380 nm. The low peak intensity of 2D-2D graphene/NiO composite suggests that the addition of graphene in 2D NiO effectively reduce the recombination rate of charge carriers as exposed in Fig.4.8 (b). The PL results indicate the surface interaction between NiO and graphene sheet and maximum charge transferring rate are responsible for enhanced photocatalytic efficiency.

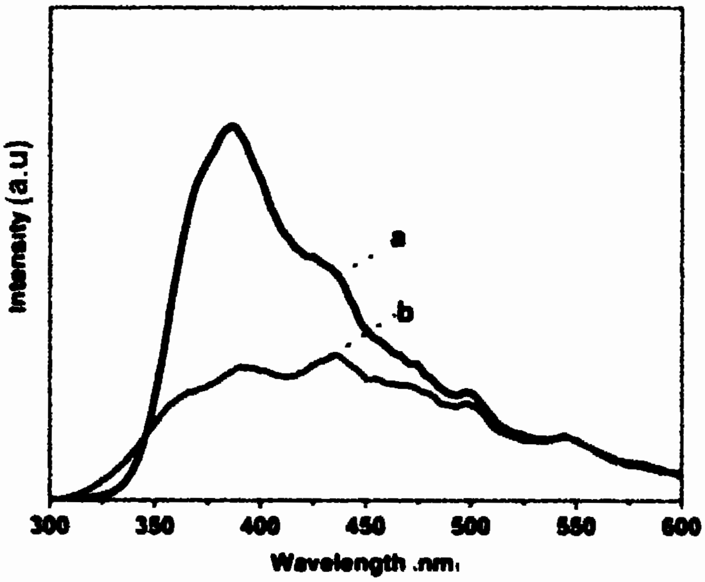

Figure 4.8. PL spectra of pure and composite samples; (a) NiO nanosheets and (b) 10.0% graphene/NiO composites.

4.3.8. Photocatalytic efficiency

All the prepared samples have been exposed under visible light to initiate photocatalytic process for the degradation of MO dye. The self-degradation of methyl orange is negligible. However, the photocatalysts play a vital role for the decomposition of dye. Pure NiO showed weak degradation efficiency of ~ 30.0% in 4 hrs. It is noticed that NiO nanosheets exhibit less photocatalytic performance owing to following underlying factors. (i) The quick recombination of electron-hole pairs. Only some of e^- take part in oxidation of dye which are captured by defect state of NiO nanosheets. (ii) Higher band gap is also responsible for less adsorption of dye (MO) molecules during the reaction. In contrast to pure NiO, graphene sheets and graphene/NiO (3.0%) graphene/NiO (5.0%) and graphene/NiO (10.0%) composites displays the photo catalytic efficiency of 94.0%, 45.0%, ~60.0% and 75.0%, respectively after same time intervals. Because graphene act as an electron reservoir account of its long π- conjugation composition to capture the photo excited electrons and suppress the recombination of charge carriers. Consequently, the photocatalytic activity of graphene/NiO nanocomposites is increased on account of synergistic effect between NiO and graphene. The synergistic effect made the pure NiO highly photoactive when used in various combinations with graphene. These results indicated that the significantly reduced band gap energy boost the effective utilization of solar irradiation which is favorable for enhanced photocatalytic efficiency.

The time degradation graph of MO in presence of different photocatalysts under visible light for 4 hrs is shown in Fig. 4.9. It can be noticed that the degradation of MO is increases as the time increases.

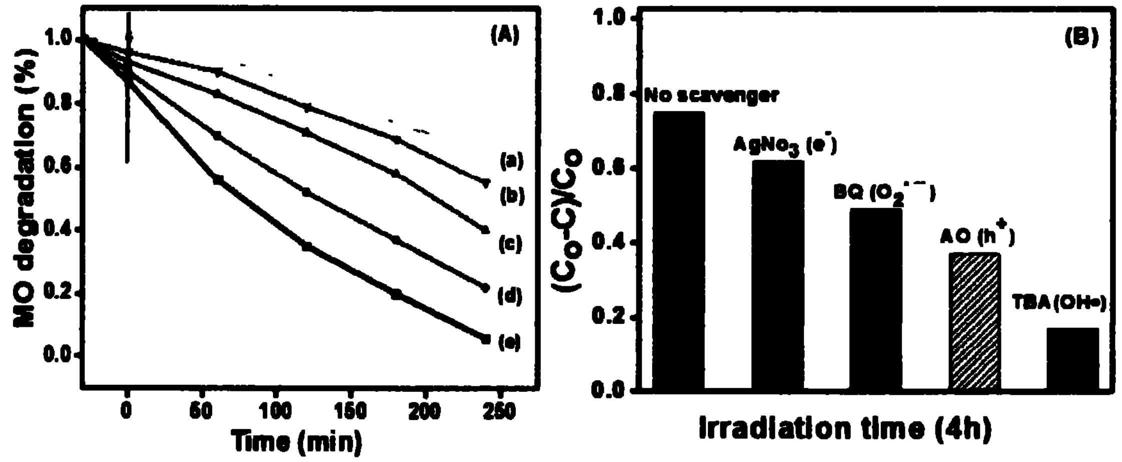

Figure 4.9 (A). Time degradation graph of MO under visible light; (a) NiO nanosheets (b) 3.0% graphene/NiO nanocomposite (c) 5.0% graphene/NiO nanocomposite (d) 10.0% graphene/NiO

nanocomposite (e) graphene sheets, (B) Controlled experiments of photocatalytic degradation of MO using diverse radical scavengers over the graphene/NiO composite under visible light irradiation for 4hrs.

4.3.9. Role of scavengers on photocatalytic activity

To determine the contribution of reactive species and explore the photocatalytic mechanism of graphene/NiO composite, controlled experiments were carried out by using diverse radical scavengers (Fig. 4.9B). When $AgNO_3$ as electron scavenger is added, the photocatalytic efficiency was slightly reduced because electrons are not directly involved in the degradation of MO. The more electrons are scavenged by $AgNO_3$ and electron transfer to graphene sheets reduces which results in less activity. Benzoquinone (BQ) as superoxide radical ($O_2^{\bullet-}$) scavenger exhibits significant effect for photoactivity of photocatalyst (graphene/NiO) due to incorporation of graphene sheets. The graphene sheets act as an acceptor in which network of graphene sheets store photogenerated electrons and increase the separation and transferring rate of charge carriers which facilitate the activation of O_2, consequently boosting the formation of superoxide radical that promote its contribution towards the degradation of MO over graphene/NiO composite. The addition of tetra-butyl alcohol and ammonium oxalate (AO) act as hydroxyl radical (OH•) and hole scavenger respectively in reaction system inhibited the photocatalytic activity of graphene/NiO composite, showing that OH• radical and hole (h^+) play an imperative role for the degradation of MO under visible light [151,182,183].

4.3.10. Mechanism discussion

The mechanism of photocatalytic activity of 2D-2D graphene/NiO nanocomposite for the degradation of MO is presented in a Fig. 4.10. The results indicate that the E_{VB} and E_{CB} are more positive (+2.9 eV) and negative (-0.4 eV) than graphene (as shown in Fig. 4.6D). Therefore, initially under visible light, excited electrons in conduction band of NiO can easily transfer to graphene sheets, leaving behind holes, because graphene act as an electron's acceptor due to low Fermi level (-0.08 eV) than E_{CB} of NiO. So, the photoexcited electrons stored in $\pi - \pi$ network of graphene sheets helps to increase the separation rate of charge carriers. Moreover, the degradation of MO molecules on the surface of photocatalyst occurs due to transferring of electrons from NiO to graphene sheets. So, these transferred electrons react with dissolved oxygen to produce reactive radicals ($O_2^{\bullet-}$) and hydroxyl radicals are also generated by converting the unstable reactive species present in aqueous solution. These reactive species (OH•, $O_2^{\bullet-}$) play vital role to degrade the MO. Primarily, the reactive species attack on the MO molecules to break the Azo bond followed by the breaking of aromatic rings leads to formation of organic intermediate (phenol, nitrobenzene, 1,4-benzoquinone, until it completely converted into harmless products (CO_2 and H_2O) (eq 4.15) [184. 185, 186]. The chemical reactions that occur at the liquid-solid interface is represented as follows based on literature and our observations (eq. 4.11-4.15).

$$\text{Graphene / NiO} + hv \rightarrow \text{NiO}\,(h_{VB}^{+}) + \text{graphene}\,(e_{CB}^{-}) \qquad (4.11)$$

$$\text{NiO}\,(h_{VB}^{+}) + (H_2O + H^{+} + OH^{-}) \rightarrow \text{NiO} + \dot{O}H + H^{+} \qquad (4.12)$$

$$\text{Graphene}\,(e_{CB}^{-}) + O_2 \rightarrow \text{graphene} + O_2^{\bullet-} \qquad (4.13)$$

$$O_2^{\bullet-} + 2(H^{+} + OH^{-}) \rightarrow H_2O^{\cdot} + 2\,OH^{-} \qquad (4.14)$$

$$\dot{O}H + \text{MO} \rightarrow \text{Intermediates} \rightarrow H_2O + CO_2 \qquad (4.15)$$

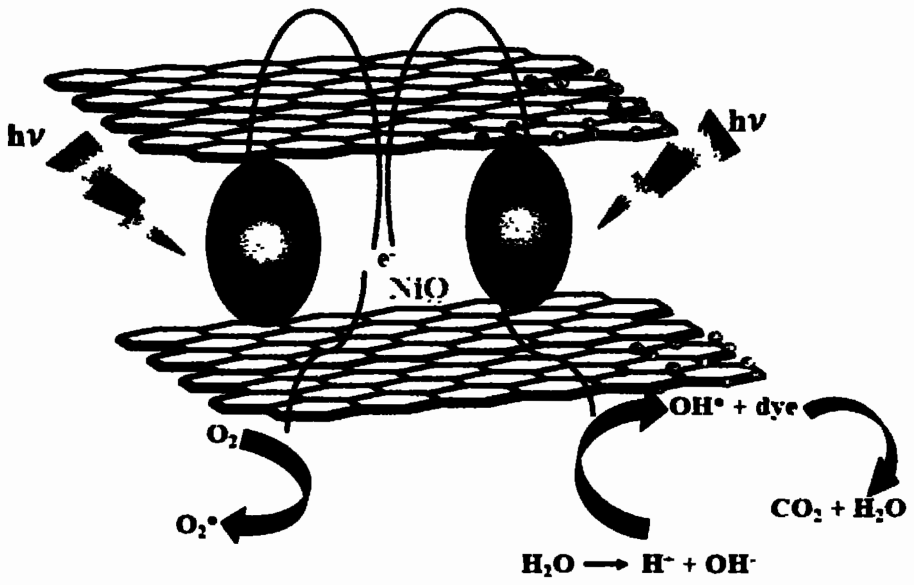

Figure 4.10. Photocatalytic mechanism for degradation of MO over the prepared 2D-2D graphene/NiO nanocomposite.

4.4. Conclusions

2D-2D graphene/NiO nanocomposites with different graphene contents were synthesized via wet impregnation method. The formation of NiO nanosheets and graphene sheets was confirmed by X-ray diffraction. In 2D-2D graphene/NiO composites, the NiO sheets are uniformly dispersed on graphene sheets which facilitate interfacial coupling between them. It was found that the absorption edge of graphene/NiO nanocomposites slightly shift towards longer wavelength which extend the absorption in visible range. As-synthesized 2D-2D graphene/NiO exhibits improved photocatalytic performance as compared to pure NiO towards the organic dye (MO) under visible light. This remarkably increased photocatalytic efficiency can be assigned to the interfacial contact associated with transferring rate and prolonging the lifetime of photogenerated charge carriers. The role of different scavengers described that scavenging of $OH^{\bullet}$ radicals greatly reduce the photocatalytic activity as compared to electrons, superoxide radical and holes scavengers. It is hoped that this present work provides a novel path to synthesize numerous 2D-2D semiconductor sheets graphene composites which can be effectively used towards the photocatalytic environmental applications.

CHAPTER 5

Influence of integrate nitrogen functionalities in nitrogen doped graphene modified WO_3 functional visible photocatalyst

5.1 Introduction

Semiconductor based photocatalysts has gained much attraction on account of high energy demand and rising environmental problems [187]. Past few years, numerous semiconductors such as oxynitride, sulphides and metal oxides have been fabricated to derive their photocatalytic response under visible light [188,189]. However, fast recombination rate of photogenerated charge carriers and low usage of visible light limits their application towards environmental remediation [190]. Subsequently, visible light responsive photocatalytic materials have been fabricated to tackle the challenges regarding energy production and environmental contamination. Among all of them WO_3 (n-type semiconductor) is considered a potential material owing to their tunable optical and electronic properties. WO_3 has been attained intrigued attention in photocatalytic applications due to long term stable physiochemical properties, photocorrosion and visible light absorption resilience [191-193]. Unfortunately, high rate of recombination process of photo induced charge-carriers and agitation in oxygen reduction on account of narrow band gap and low-potential, respectively, makes WO_3 less effective in photocatalysis [194].

To overcome these issues, many techniques have been applied to boost the photocatalytic activities of WO_3 through incorporation of carbonaceous materials. It was noticed that the carbon materials played an imperative role to boost photocatalytic efficiency of WO_3 [195, 196]. In graphene based composite material's large aromatic. structure of the graphene act as an electrons collector to improve the transportation of interfacial electrons because of its tremendous properties i.e., such as high surface area (2630 m^2g^{-1}), thermal and chemical stability. However, further modification of graphene's intrinsic features is needed to meet up the desired demand for vast of potential applications. Thus, doping of nitrogen is one of the best approaches to module its tremendous properties [197-199]. Addition of nitrogen atoms in graphene sheets tailor its electronic structure and convert it into semiconductor by breaking its lattice symmetry. Subsequently formation of more active sites in N-doped graphene sheets leads to significantly improve the photocatalytic efficiency. With improved properties such as tunable electronic structure, huge surface area, high active sites and superb charge carrier's, the N-doped graphene is considered as a promising candidate for photocatalytic activities [200, 201]. M. B. Tahir et al. [190] have reported that graphene/WO_3 (7.0%) composite showed outstanding photocatalytic efficiency regarding hydrogen generation as compared to pure WO_3. Li jia et al. [202] have examined that N-doped graphene/CdS composite degraded salicylic acid and methylene blue (MB) under visible light exposure. B. Amanulla et al. [203] have observed Ag_3PO_4 decorated nitrogen-doped graphene composite degraded 99.0 % eosin yellow compound to less toxic non-molecules. M. Ahmed et al. [204] have studied that 15-mm porous carrier exhibited highest removal of nitrogen (98.0%) from microaerobic bioreactors.

Most of organic species are utilized at large scale in agricultural, chemical industries, medical, and domestic proposes. 2, 4-dichlorophenol (2,4-DCP) is derivative of phenol having one or more covalently bonded chlorine atom, poisonous and non-biodegradable compound [205]. Many chlorinated compounds are xenobiotic, bioaccumulation in natural environment and recalcitrant nature. 2,4-DCP is intermediate product in manufacturing of 2,4-di-chloro-phenoxy-acetic acid herbicide [206]. The adverse contamination due to 2,4-DCP results into harmful infection in kidney, respiratory system, and liver. Most of organic dyes have been exploited in many chemical industries like textile, paints, pharmaceutical and cosmetics [207]. Methyl orange (MO) is an azo dye having very strong –N=N– bonds and carcinogenic in nature [208]. Therefore, both organics have been employed as model pollutants to mineralize them under visible light.

In this work, N-graphene/WO_3 nanocomposites as active photocatalysts with various amount of N-graphene were fabricated through wet chemical impregnation method. N-graphene/WO_3 composites presented remarkable photocatalytic activity towards the mixture of 2, 4-DCP and MO in aqueous solution. The improved photo degradation performance of N-graphene/WO_3 nanosystem could be considered to the resilient interfacial interaction of nitrogen doped graphene network and WO_3 which create massive active sites on its surface. This significantly promotes the adsorption of strong organic species. The effecting parameter (pH) and radical scavenger species were examined to demonstrate the photocatalytic reaction. Moreover, N-graphene/WO_3 also showed good reusability after many recycling. Therefore, the present work provides an avenue to develop several N-graphene/semiconductor nanocomposites for numerous effective applications.

5.2 Experimental

5.2.1 Materials

Graphite power, sodium tungstate (Na_2WO_4), hydrochloric acid (HCl), phosphoric acid ($H_3\,PO_4$), nitric acid (HNO_3), potassium permanganate ($KMnO_4$), methyl orange (MO), hydrogen peroxide (H_2O_2), ethanol and urea were provided by Sigma-Aldrich.

5.2.2 Synthesis of GO

GO was synthesized through Tour's method [209, 210]. Graphite was taken as starting material. 1.0g graphite and 6.0g of potassium permanganate are mixed. Then 9:1 ratio of sulphuric acid to phosphoric acid was mixed and pour into above solution keeping the temperature below 40 °C under mechanical stirring to make a homogeneous solution. This solution kept on hot plate at 50 °C for 13hrs under constant stirring. After formation of brown purple liquid, a liquid solution cool down at room temperature and endure into 200 mL of deionized ice water. A bright yellow solution obtained by adding H_2O_2 (1.0 mL). Finally, the product (GO) was collected by washing and centrifugation with distilled water and final product was dried at 60 °C for 5 hrs. Urea as a nitrogen source and NaOH for chemical reducing agent was used to transform the graphene oxide into N-graphene sheets through the hydrothermal treatment at 200 °C for 8hrs.

5.2.3 Preparation of WO_3

The WO_3 were fabricated through sol-gel method. 5.0g sodium tungstate was mixed into a 150 mL of distilled water followed by slowly addition of desire quantity of HNO_3 aqueous solution under continuous stirring. Solution was placed on hot plate at 40 °C for 5 hrs. Subsequently, the yellow precipitate was obtained. These obtained precipitates were centrifuged, washed with distilled water, and dried at 60°C. Final product was calcined at 600 °C for 4hrs.

5.2.4 Synthesis of N-graphene/WO_3 nanocomposites

For preparing N-graphene/WO_3 nanocomposites chemical wet impregnation treatment was adopted. For this purpose, 500 mg WO_3 dissolve into 20 mL distilled water. At same time 0.09g of N-graphene was dispersed into distilled water (20 mL) and sonicated for few minutes to make a homogeneous solution. N-graphene solution was added into above solution drop wise under constant stirring and dried at 60 °C to attain 1.0% N-graphene/WO_3 composite. Same procedure was followed by varying the amount of N-graphene to obtain various wt. % N-graphene/WO_3 (3.0% N-graphene/WO_3 and 5.0% N-graphene/WO_3) nanocomposites.

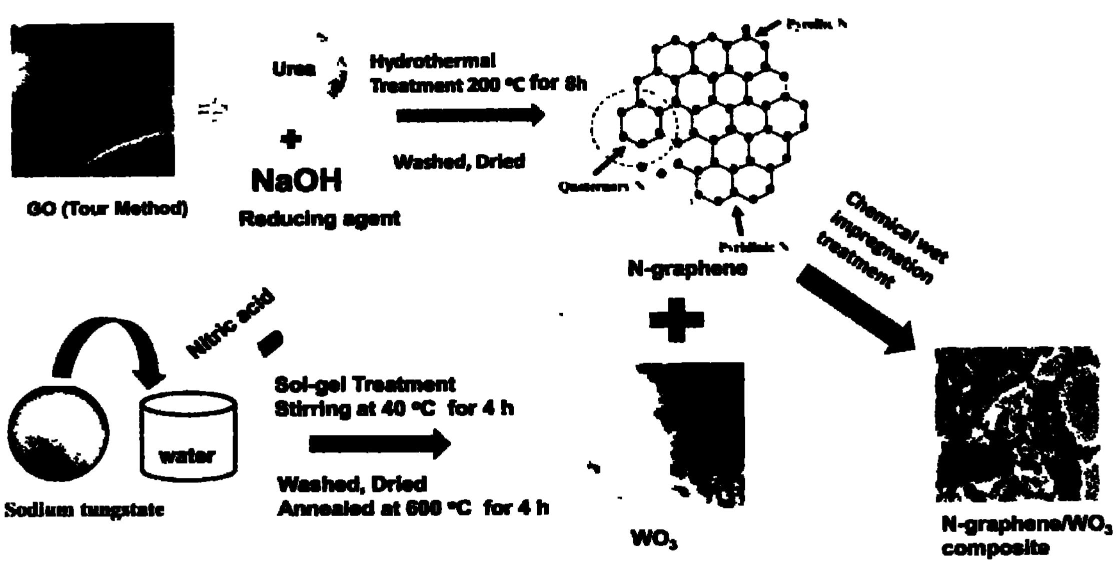

Scheme 5.1. The synthesis route of N-graphene/WO_3 nanocomposite.

5.2.5 Characterization techniques

The X-rays diffractometer (X'pert PRO MPD, PANalytical with Cu K_α radiation and wavelength =1.54Å) was employed to examine the structural properties of samples. The surface morphology and elemental composition of materials were analyzed through scanning electron microscope (SEM) (MIR3, TESCAN) and EDX (JEOL-JAD-2300), respectively. The detailed morphological studies were performed through transmission electron microscopy (TEM) worked at 80 kV. The FTIR (ALPHA II, Bruker, Germany) was used to explore the functional groups of prepared nanocomposites. The optical properties of samples were investigated by UV-Vis absorption spectroscopy (UV-2600 spectrometer, Shimadzu, Japan). PL spectra were obtained by using fluorescence spectrometer (Perkin Elmer, Ltd., Germany). XPS analysis was performed by Kratos Axis Ultra spectrometer with (monochromatic Al kα).

5.2.6 Photocatalytic activity of organic species

The photocatalytic efficiency of photocatalysts was evaluated through the degradation of organic species MO and 2, 4-DCP (20 mg L^{-1} of each) in visible light region. Initially, 50 mg of catalyst was added into 50 mL solution of organic mixture under magnetic stirring and kept the mixture in dark place for 30 mints to accomplish adsorption-desorption equilibrium. Then the suspended mixture was irradiated by visible light at room temperature under same environmental condition. After every hour, 4.0 mL suspended solution was collected and centrifuged to do away the catalyst. The decomposition of organic species of 2,4-DCP and MO at maximal adsorption (λ_{max}) of ~283 and ~464 nm, respectively was examined by using UV-Vis spectroscopy. The degradation % was calculated by employing the relation as given below:

$$\% \text{ degradation} = \left[C_o - {}^{C}/_{C_0}\right] \times 100 \tag{5.1}$$

Here C_0 and C represents concentration before and after irradiation of organics, respectively [211].

5.3 Results and discussion

5.3.1. Structural analysis of prepared samples

Figure 5.1 shows the XRD pattern of GO, N-graphene, WO_3 and composites of N-graphene/WO_3. In XRD profile of GO (Figure 5.1A), a very sharp and strong diffraction peak is observed at 9.2° (001) which indicates that oxidation of graphite into GO through expanding the interlayer spacing from 3.4 Å to 9.2 Å due to incorporation of oxygen bearing groups at the peripheries and along carbon grid of GO [212]. In XRD patterns of N-graphene, a diffraction peak at 26.5° (002) (with lattice constant 0.34 nm) is obviously seen which is clear evidence of reduction of GO into N-graphene sheets during the chemical treatment of GO with urea [213]. In doping process, oxygen functionalities of GO performs as a backbone for the incorporation of foreign material which offer active sites for integration of nitrogen atoms into the graphene network. Deoxygenation process leads to the existence of π–π bonding interaction between nitrogen and carbon lattice of graphene which significantly restores sp^2 graphitic crystalline structure i.e., graphitic, pyridinic N and sp^3 pyrrolic N [214]. Incorporated nitrogen functionalities into grid of carbon would effectively reduce dense sp^3 structural defects in GO lattice [215]. L. K Putri et al. [214] have observed that introduction of nitrogen and boron into GO considerably reformed the bonding structure and improved optical properties which were promising in photocatalytic hydrogen production.

Figure 5.1B reflects XRD profile of WO_3, 1.0% and 3.0% N-graphene/WO_3 composites. XRD diffraction signals of WO_3 and its composites exhibit characteristic peaks at $2\theta = 23.1°$ (002), 23.4° (020), 24.4° (200), 26.6° (120), 28.8° (112), 33.2° (022), 34.2° (202), 35.5° (122), 41.6° (222), 47.2 ° (004), 49.7° (140) and 55.6° (420) ascribed to monoclinic of WO_3 [JPDS No. 43-1035][216]. The sharp intensity peaks of pure WO_3 indicate its high crystallinity though the incorporation of N-graphene reduces crystallinity. It is noticed in composite samples that addition of N-graphene into host WO_3 not only broaden the signals significantly due to amorphous nature of carbon material but also slightly downshift the characteristic peaks due to internal stress of carbon and nitrogen functionalities in nitrogen doped graphene. No additional peaks related to carbon material were observed. These might be due to weak diffraction signal of disorderly stacked N-graphene sheets but its existence is clearly observed in TEM and Raman studies. Jamila et al. [217] have observed the amorphous nature of WO_3/GO/NCQDs composite with incorporation of GO.

Figure 5.1C represents the FTIR spectrum of pure WO_3, 1.0% N-graphene/WO_3 and 3.0% N-graphene/WO_3. In all samples, the wide absorption signals are observed in range of 3000-2800 cm^{-1} which indicate O—H stretching vibrations. It is also seen that O—W—O stretching in all samples vibrations are in the range of 1020-650 cm^{-1} [218, 219]. In 1.0% N-graphene/WO_3 and 3.0% N-graphene/WO_3, two new absorption characteristic peaks are observed at 1600 and 1409 cm^{-1} conforming the C=N and C=C stretching modes. These modes indicate the doping of nitrogen atom and skeleton vibrations of graphene sheet, respectively [220, 221] which confirms the formation of composite samples successfully.

Figure 5.1D depicts Raman spectra of graphene oxide (GO), N-graphene and 3.0% N-graphene/WO_3 composite samples. In Raman spectra (GO and N-graphene), typical D band of GO and N-graphene centered at 1337 and 1342 cm^{-1} while G band located at 1593 and 1601 cm^{-1}, correspondingly. I_D/I_G ratio of GO was found to be 1.13 that was increased to 1.15 in N-graphene [222,223]. The results indicated that after nitrogen doping in GO defects were enhanced by nitrogen dopant which disordered the graphene lattice. Raman spectrum of 3.0% N-graphene/WO_3 composite is well resolved into characteristic peaks located at 280, 334, 724 and 813 cm^{-1}. Comparatively, sharp peaks centered at 724 and 813 cm^{-1} indicates the O—W—O or W^{+6} —O stretching vibrations [216]. Peaks at low frequency region at 280 and 334 cm^{-1} confirms the O—W—O bending vibrations of monoclinic WO_3 [224]. Besides these, two additional peaks at 1350 and 1604 cm^{-1} are observed which designates D and G band of N-graphene sheet through the linking bridge of W—O—C. It is worth noting in both N-graphene and 3.0% N-graphene/WO_3 composite the upshifting of D and G bands which is associated with new surface linkages well consistent with literature [187, 196, 225]. The connection between WO_3 and N-graphene well promotes electron conduction and acceleration of electrons towards the surface of catalyst for redox reaction [210].

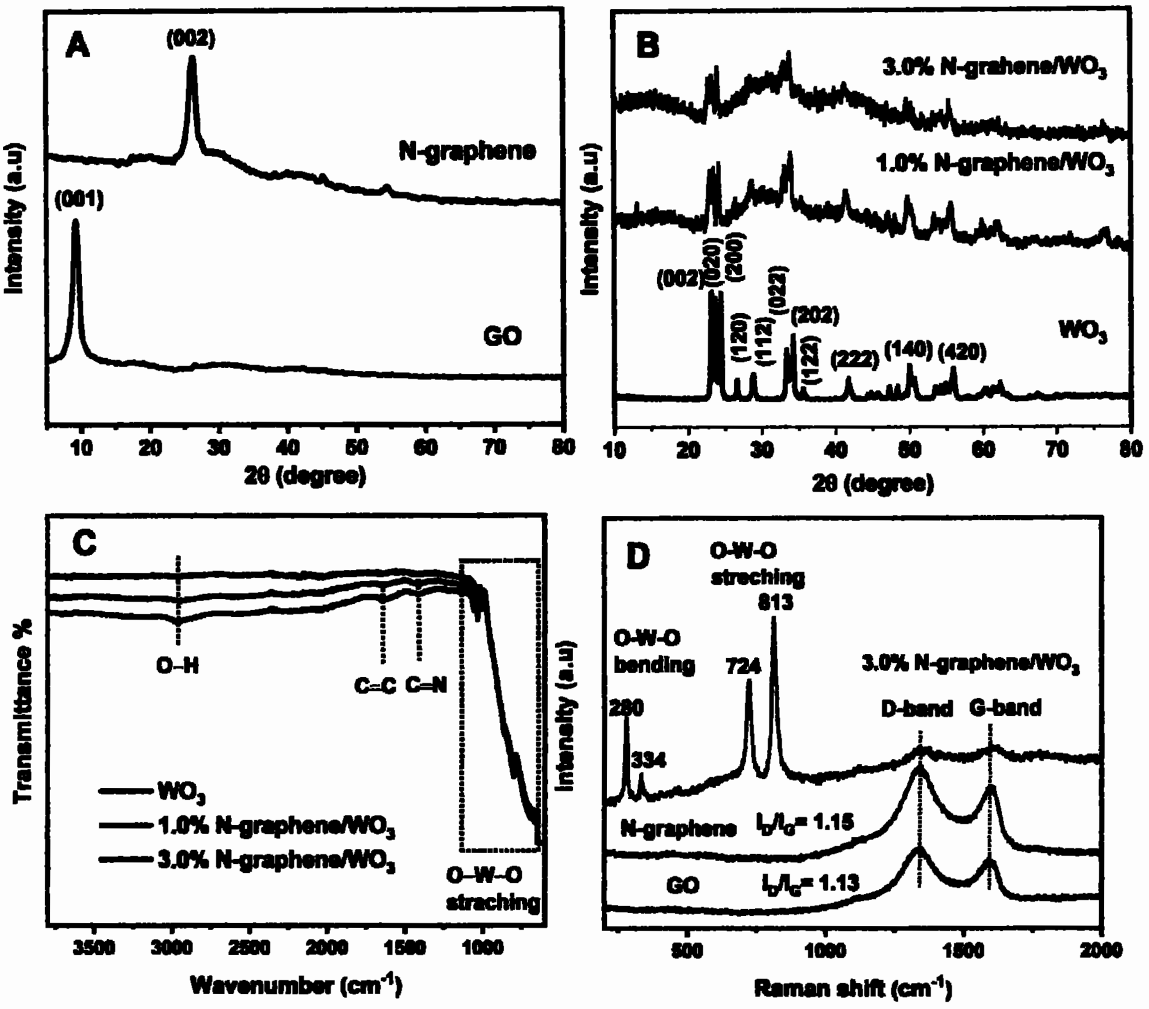

Figure 5.1. XRD pattern of (A) graphene oxide, N-graphene, (B) XRD and (C) FTIR spectra of WO3, 1.0% N-graphene/WO3, and 3.0% N-graphene/WO3 (D) Raman spectrum of graphene oxide, N-graphene and 3.0% N-graphene/WO3.

5.3.2. Morphological images

Figure 5.2 shows morphological images of prepared samples. SEM photograph of WO_3 (Figure 2a) reveals the round shaped primary particles with little agglomeration. SEM image of N-graphene (Figure 5.2b) indicates wrinkled and randomly overlapped sheets. In 3.0% N-graphene/WO_3 (Figure 5.2c), some inhomogeneous distribution of irregular massive rod like blocks along with round shaped particles of WO_3 can be noticeably seen on cracked sheets of N-graphene. This morphology with high active surface area has aptitude for capturing the visible light photons. TEM images of 3.0% N-graphene/WO_3 composite at different nano scales is shown in Figure 5.2d and f. In both images, it is obviously seen that N-graphene sheets are well decorated with WO_3 nanoparticles which displays the intimate contact between WO_3 and N-graphene. This contact between WO_3 and N-graphene lessens the recombination rate of photo induced charge carriers to improve the photocatalytic efficiency and improves visible light absorption as observed in DRS analysis. Additionally, the more wrinkles on the surface of graphene may arise due to nitrogen doped atoms that provide more active sites for the adsorption and desorption of organic species in photocatalytic activity. It can also be seen in both SEM and TEM images that N-graphene sheets maintained their two dimension (2D) structure after doping with nitrogen atoms [226]. HRTEM (Figure 5.2f) indicates inter planer distance of 0.37 nm (020) of WO_3 along with the few layers of N-graphene wrinkled sheets.

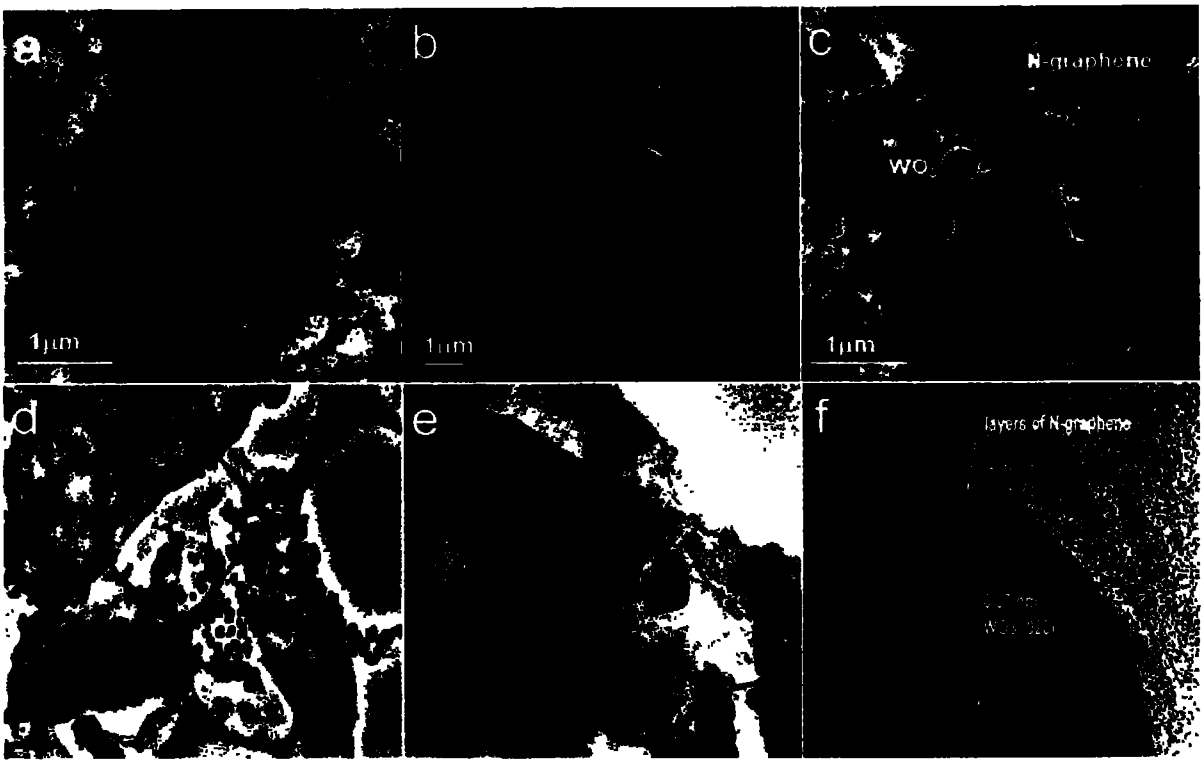

Figure 5.2. SEM images of pure WO_3 (a), N-graphene sheets (b) and 3.0% N-graphene/WO_3 nanocomposite (c) TEM images (d, e) and HRTEM (f) of 3.0% N-graphene/WO_3 composite.

5.3.3 EDX Analysis and elemental mapping

The elemental composition of synthesized materials was examined through energy dispersive X-ray analysis. The EDX spectrum of WO_3 (Figure 5.3A) displays W and O peaks with no other peaks which confirm the formation of pure WO_3 nanoparticles. Moreover, in 3.0% N-graphene/WO_3 nanocomposite (Figure 5.3B) an extra peak of C atom and N is detected. Moreover, the elemental mapping of 3.0 %N-graphene/WO_3 is shown in Fig.5.3 (a-e). The elemental composition of prepared samples is presented in Table 5.1.

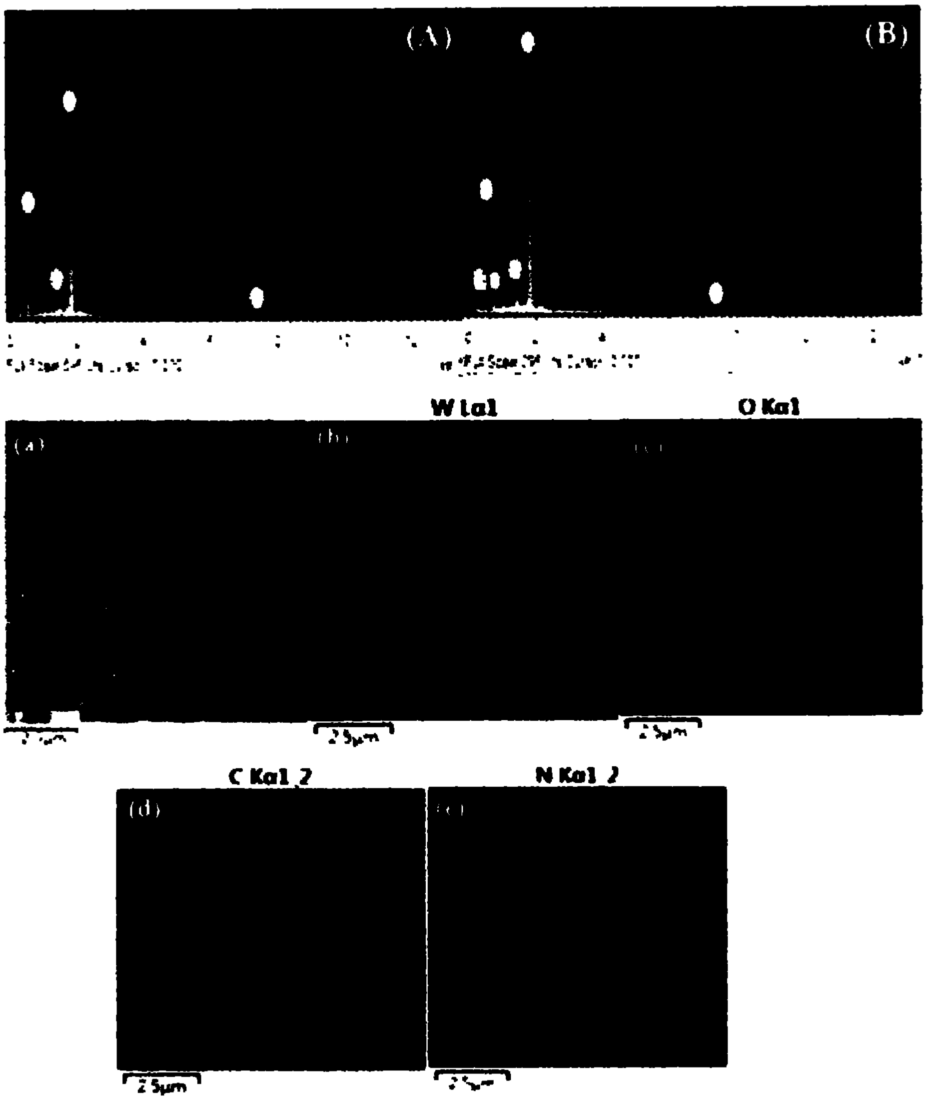

Figure 5.3. EDX spectrum of WO_3 and 3.0% N-graphene/WO_3 and elemental mapping of 3% N-graphene/WO_3 and their elements tungsten (W), carbon (C), oxygen (O) and nitrogen (N) respectively (a-e).

Table 5.1. Elemental composition of WO_3 and 3.0% N-graphene/WO_3 nanocomposite calculated by EDX spectra.

Photocatalysts	**Atomic %**				**Weight %**			
	W	O	C	N	W	O	C	N
WO_3	24.81	75.19	0	——	79.13	22.87	0	——
3.0 % N-graphene/WO_3 composite	23.67	60.27	11.26	4.8	78.70	18.50	2.71	0.9

5.3.4. UV-Vis absorption study and photoluminescence spectra (PL) spectra

UV-Visible diffused reflectance spectra of as-synthesized WO_3 and N-graphene/WO_3 are shown in Figure 5.4A. The absorption edge of pure WO_3 is found in visible region. Oxygen vacancies present in the lattice of WO_3 donates the electrons to its conduction band. As a result, WO_3 is considered as an n-type semiconductor but high rate of recombination of photo generated charge carriers reduces its photocatalytic ability [227]. UV-Visible spectrum of N-graphene is shown in inset (Figure 5.4A). The absorption edge of N-graphene is observed in visible region which is well correspondent to literature [228]. According to literature, GO has absorption edge at ~263 nm [229] but this edge has been shifted to visible region ~427 nm in N-graphene. Nitrogen doped atoms into graphene sheet reduced oxygen functional groups of GO and retained sp^2 hybridized system of conjugated structure of carbon with nitrogen as observed in XRD profile and also introduced nitrogen defects. It is suggested that nitrogen introduced the tail energy states below the conduction band of graphene by distorting the graphene lattice regularity. This foreign material allows π to π^* electronic transition and altering zero band gap semi-metallic graphene to semiconducting material [230]. It is noteworthy that the absorption edge of N-graphene/WO_3 composites has been red shifted towards longer wavelength and have the ability of more light scattering during photocatalysis process. The band gap values of fabricated samples are shown in Figure 5.4B. The band gap energy values of WO_3, 1.0% N-graphene/WO_3 and 3.0% N-graphene/WO_3 were calculated by Tauc plot and found to be 2.60, 2.53 and 2.45 eV, respectively. The effective reduction in band gap owing to nitrogen defects into carbon atoms which modify the surface of bare WO_3. The optical band gap value of N-graphene is shown in inset (Figure 5.4B) and come out 1.5 eV. The reduced optical band gap of 3.0% N-graphene/WO_3, availability of reactive sites and new linking bonds (W−O−C) are the promising factors in improved photocatalytic activity.

PL emission spectroscopy is a good tool to determine the trapping and transferring efficiency of charge carriers, energy band structure and provide the information about oxygen deficiencies in the prepared samples. PL spectra of pure WO_3 and N-graphene/WO_3 nanocomposites were recorded under the excitation wavelength of 280 nm as shown in Figure 5.4C. A broad peak located at 302 nm related to surface defects present in form of oxygen vacancies in WO_3. Sharp emission peaks centered in range of 458-467 nm indicates near band-edge transition. While the shoulder peak located at 537 nm could be attributed to presence of oxygen deficiencies in samples [231,232]. Furthermore, it is noteworthy that owing to incorporation of N-graphene sheets, PL intensity of N-graphene/WO_3 nanocomposites significantly reduced. A prominent quenching in PL intensity is obviously seen in 3.0% N-graphene/WO_3. The reduction in intensity is attributed to the formation of new additional paths for transferring of exited electrons from WO_3 to N-graphene sheets which effectively inhibited the recombination rate of charge carriers [233]. This property is favorable to increase the photocatalytic efficiency of N-graphene/WO_3 nanocomposites.

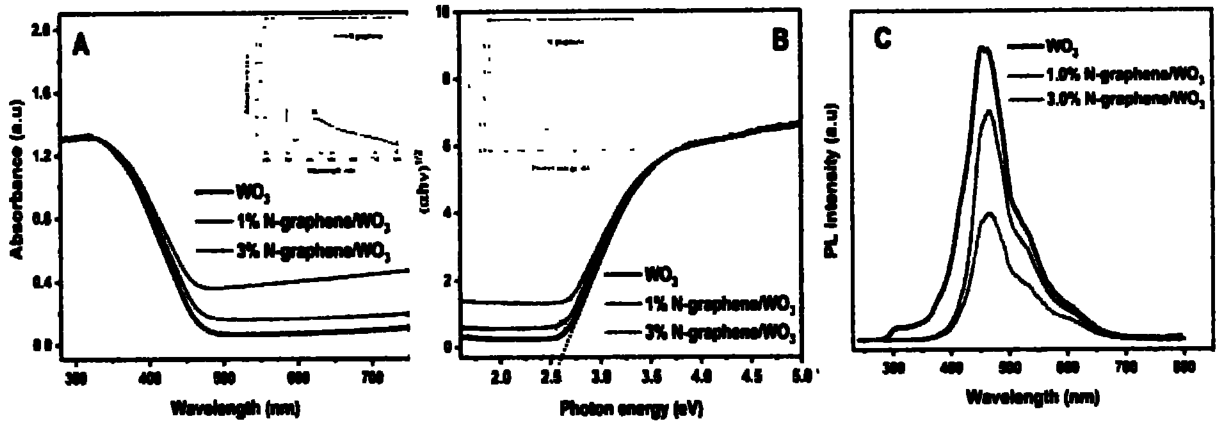

Figure 5.4. Optical absorption spectra (A) and Tauc relation (B), (inset) N-graphene and (C) PL spectra of corresponding pure WO$_3$, 1.0% N-graphene/WO$_3$ and 3.0% N-graphene/WO$_3$ composites.

5.3.5. XPS analysis

XPS analysis (Figure 5.5) was performed to determine bonding configuration of constituent elements (W, O, C and N) of 3.0% N-graphene/WO$_3$. Figure 5.5a shows high resolution spectrum of W4d which splits into two noticeable peaks i.e W4d$_{5/2}$ and W4d$_{3/2}$ found at binding energies of 246.7 eV and 262.0 eV, respectively [234]. XPS spectrum of O 1s peaks (Figure 5.5b) is fitted into two peaks at binding energies of 531.3 and 532.8 eV attributing to W–O and hydroxyl groups in sample, respectively. XPS spectrum of C 1s (Figure 5.5c) is decovoluted into three obvious peaks. The most prominent peak at 284.2 eV shows graphite-like sp^2(C=C) bonding configuration. This indicates that maximum carbon atoms in 3.0% N-graphene/WO$_3$ nanosystem exist in conjugated honeycomb lattice. The other two characteristic peaks at binding energies of 285.2 and 286.6 eV are associated to Csp^2–N (pyridinic) and Csp^3–N (pyrrolic) bonding. These results are matched well with the report [235]. Figure 5.5d illustrates all possible bonding configuration of nitrogen functionalizes in 3.0% N-graphene/WO$_3$ composite. The peaks centered at 398.5, 399.8 and 401.3 eV reflect pyridinic N, pyrrolic N and graphitic N, respectively [236]. It is clearly seen that the peak of pyrrolic N is very sharp than others which confirmed that pyrrolic N is greatly doped in our sample.

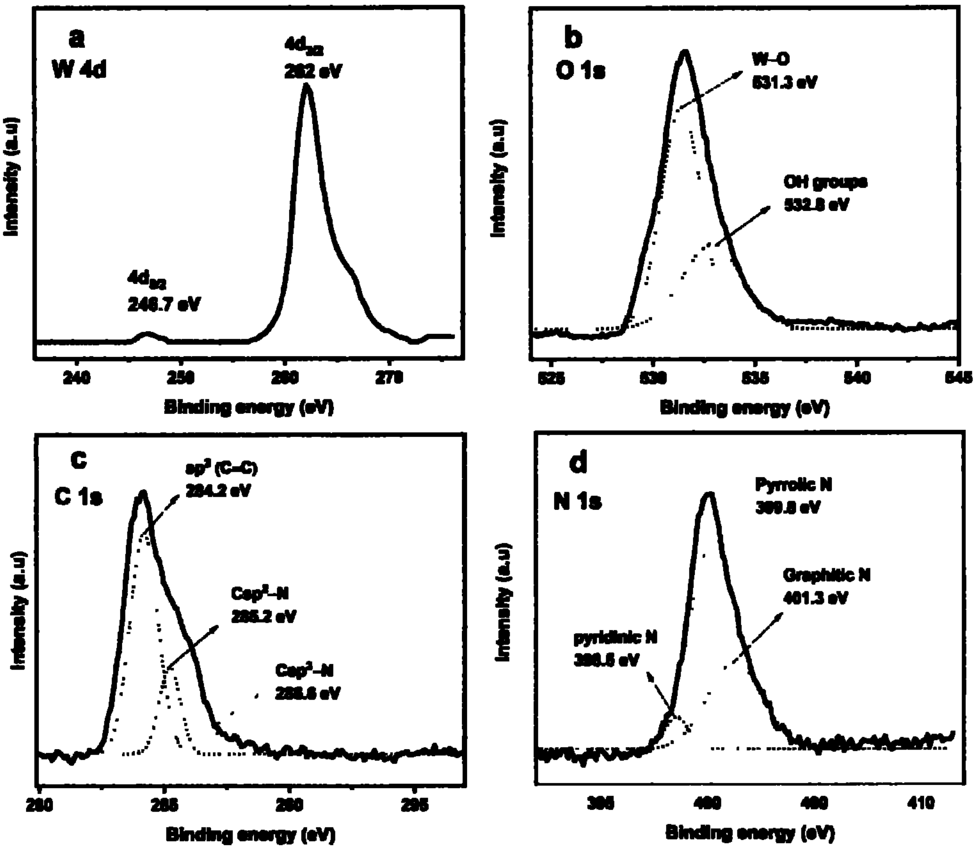

Figure 5.5. High revolution XPS spectrum of (a) W4d, (b) O 1s, (c) C 1s and (d) N 1s of 3.0% N-graphene/WO_3 nanosystem.

5.3.6. Photocatalytic activity and reusability of photocatalysts

Photocatalytic efficiency of as-synthesized materials was evaluated through degradation of 2, 4-DCP and MO under visible light as shown in Figure 5.6A and B. This photoreaction is very important for the laboratory and industrial point of view. Because mixed MO (dye) and 2, 4-DCP (pollutant) system is checked. The effluents from the industry are in the mixed form. So it is a key step to degrade the many pollutants at the same time and at natural pH. The presumed reason of the higher degradation of mixed pollutants as compared to individual pollutant may be the synergistic effect of one on other [237]. In the mixed system of 2, 4-DCP and MO, these pollutants act as the hole scavengers which can decrease the recombination of electrons and holes more. This mutual stimulating effect offers a vital support using N-graphene/WO_3 as visible-light catalyst for efficient simultaneous removal of 2,4-DCP and MO by photocatalytic process, respectively, in the same system. Thus enhancing the photocatalytic activity as compared to the single pollutant system. The rate of degradation of the pollutant in mixed system is more as compared to one by one. Photocatalysts play a decisive role for the degradation of 2, 4-DCP and MO. Figure 5.6A (MO) and 5.6B (2,4-DCP) showed that pure WO_3 performed minimum degradation efficiency ~24.0% of MO and ~16.0% of 2,4-DCP after 5hrs because of having low reduction potential and leaning to trap the photo generated charge carriers. It results into high rate of recombination. The highest degradation rate against the organic species was measured as (~94.0% of MO and ~81.0% of 2, 4-DCP) through 3.0% N-graphene/WO_3. MO and 2, 4-DCP removal by N-graphene was tested as ~31.0% and ~24.0 %, respectively. 1.0% N-graphene/WO_3 sample exhibited ~53.0% degradation process of 2, 4-DCP and ~78.0% of MO, respectively. While 5.0% N-graphene/WO_3 nanocomposite showed ~64.0% of 2, 4-DCP and ~86.0% of MO, respectively. Sajjad et al. [216] have reported that 2.0% ZnO/WO3 composite showed the highest degradation activity against MO solution. It is noticed that N-graphene/WO_3 composites showed excellent photocatalytic efficiency due to following reasons (i) the N-graphene has super charge carrier mobility. Consequently, the addition of optimum contents of graphene in WO_3 enhanced the photocatalytic performance by providing plenty of active sites and conductive channels for the transportation of electrons to surface of nanocomposites. (ii) N-graphene effectively reduce band gap of WO_3 due to synergistic effect between WO_3 and N-graphene which significantly leads to improve response of photocatalysts towards visible light region [219, 238]. Furthermore, nitrogen based defective conjunction system yields graphene with band energy gap as per studied in DRS. Nitrogen atoms provides more important active sites for enhancement of photocatalysis. As it is well known that graphene is chemically inert material because of its unpaired electrons that are tightly bound in delocalized π-system, which hinders its chemical reactivity and absorptivity [239]. N-graphene system is itself a photocatalyst because the incorporated nitrogen atoms with different electronegativity than carbon atoms in graphene produce unstable charged zone leading to polarization. This synergism results into more sites on N-graphene surface for the attachment of reactive organic species. But as the amount of N-graphene became too high, the surface area of N-graphene sheets is reduced owing to overlapping with itself. It effectively decreased adsorption and degradation of organics on the surface of photocatalyst.

The time degradation graph of organics in visible light region for 5h in presence of various as-prepared samples is shown in Figure 5.6C (MO) and 5.6D (2,4-DCP) that follows pseudo first order kinetics by using eq. (5.2).

$$\ln (C_o/C) = k_{app}t \qquad (5.2)$$

Here C_o (t = 0) and C (t = irradiation time) denotes initial and solute remaining concentration respectively. While k_{app} is degradation rate constant. From these graphs, it is observed that 3.0% N-graphene/WO_3 has the highest value of k_{app} against MO and 2, 4-DCP. Literature study of photocatalysts in degradation of various organics compared to the present work is represented in Table 5.2.

Table 5.2. Literature study of photocatalysts in degradation of various organics with present work.

Samples	Light source	Degradation % / Time Irradiation	Modal Pollutant	References
CuO/WO_3/Cu@NG	Visible	92.76%, 80.59%, 89.77%, 96.99% / (120 min)	Crystal violet, methyl orange, rhodamine B, and methylene blue	[107]
WO_3-ZnO@rGO	Visible	94% (90mint)	Methylene blue	[240]
CdTe/CdS/N-rGO	Visible	70% (360 min)	2,4-DCP	[241]
NG/TiO_2	UV	98% (300 min)	Methyl Orange	[242]
WSe_2/NG	Visible	99% (60 min)	Methylene blue	[243]
Ag_3PO_4/NG/WO_3	Visible	99% (60 min)	Indomethacin (IDM)	[244]
WO_3/N-CQDs	Visible	96 % (240min)	Methylene blue	[245]
3.0% N graphene/WO_3 composite	Visible	~94.0% ~81.0% (300 min)	MO, 2, 4-DCP	Present work

In N-graphene/WO_3 nano structure the interconnected network of N-graphene allow dispersion of WO_3 and provides promising kinetics for photocatalysis. The strong interfacial interaction between N-graphene and WO_3 promotes separation of charge carriers which enhanced photocatalytic performance towards the mixture of strong pollutants (2,4-DCP and MO) under visible light. Present work suggests that visible light responsive N-graphene/WO_3 photocatalyst is considered good material for environmental remediation.

Reusability of N-graphene/WO_3 catalyst was evaluated by the decontamination of MO and 2, 4-DCP under visible light region for four consecutive cycles (figure 5.7). The photocatalytic efficiency did not significantly reduce after four cycles of degradation tests. Figure 5.7 shows 3.0% N-graphene/WO_3 catalyst after degradation of both MO and 2,4-DCP, a small loss during filtration suggesting that the optimized photocatalyst remain active for long time and an ideal for industrial applications.

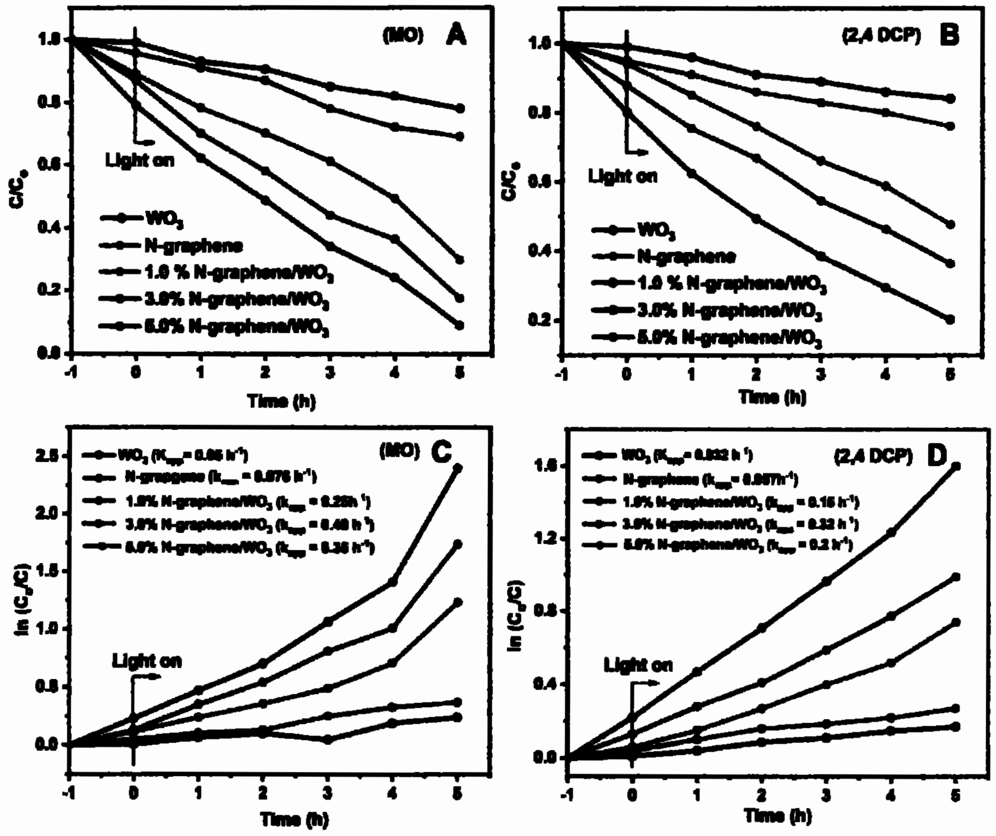

Figure 5.6. Time degradation (A,B), reaction kinetics (C,D) over MO and 2,4-DCP through WO_3, N-graphene, 1.0% N-graphene/WO_3, 3.0% N-graphene/ WO_3 and 5.0% N-graphene/WO_3.

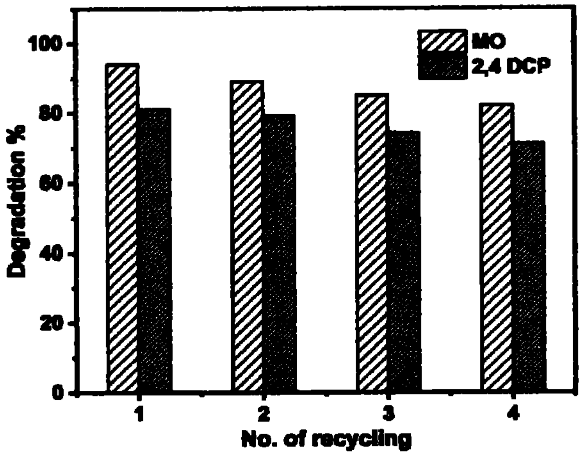

Figure5.7. Recycling of 3.0 % N-graphene/WO_3 over MO and 2,4-DCP.

5.3.7. Study of scavengers and effect of pH on photocatalysis

To determine the effect of reactive species during the photocatalytic degradation of mixed system of 2, 4-DCP and MO through 3.0% N-graphene/WO_3. In trapping test, we have used ammonium oxalate (AO), tetra-butyl alcohol (TBA), benzoquinone (BZQ) for holes (h^+), $OH^\bullet$ and $O_2^{\bullet-}$, respectively as active elements. A controlled experiment was performed by using different trapping radicals as shown in Figure 5.8A. Results revealed that the addition of AO and TBA scavengers significantly inhibited the photocatalytic reaction suggesting that holes (h^+) and $OH^\bullet$ are the major active species for the decontamination of both MO and 2,4-DCP. Whereas, the rate of photocatalytic efficiency slightly reduced with the addition of benzoquinone (BZQ) as $O_2^{\bullet-}$ scavenger indicating that $O_2^{\bullet-}$ is not mainly responsible for photo degradation process.

The effluent of industries has a large range of pH values which has greater influence on the photocatalytic degradation efficiency. For this purpose solutions having different pH were prepared by addition of optimum amount of NaOH or HCl to investigate the effect of pH on degradation of MO and 2, 4-DCP. pH mainly affects the dispersion of particle in reaction process and electrostatic interaction between organic dyes and photocatalysts. pH_{pzc} (point of zero charge) of WO_3/N-graphene was found to be 3 according to literature [246]. Under alkaline condition at pH values (pH=5, 9) greater than pH_{pzc} the electrostatic repulsive force between negative charge surface of photocatalyst and anionic MO would hinder the adsorption of MO on photocatalyst leading to reduce degradation 59% and 40%, respectively after 4 hours as shown in Figure 5.8B. Under acidic condition at low pH value (pH=2) than pH_{pzc} the positive charged photocatalyst strongly attract anionic MO promotes to enhance degradation rate 94%. But at pH=1, slightly hinder the degradation efficiency 82% due to poor dispersion and formation of particle agglomeration [247,248].

Surface property of photocatalyst plays a vital role on photo-degradation of pollutants. Therefore, the effect of pH on decontamination of 2,4-DCP was observed between pH 1 to 9 as shown in Figure 5.8C. On the basis on pH_{pzc} (=3) of photocatalyst (3.0% WO_3/N-graphene) the results indicate that the photodegradation of 2,4-DCP is higher in acidic condition than alkaline. In acidic condition pH < 3 (pH =1,2) 2,4-DCP molecules rapidly adsorbed on the positively charged surface of photocatalyst leading to increased degradation efficiency up to 76 and 87% respectively. While in alkaline condition pH > 3 (pH=5,9) 2,4-DCP barely adsorbed on the photocatalyst's surface owing to high solubility of 2,4-DCP anions and less surface interaction between negatively charged surface of photocatalyst and 2,4-DCP anions molecules impeding the photodegradation rate 49% and 39%, respectively.

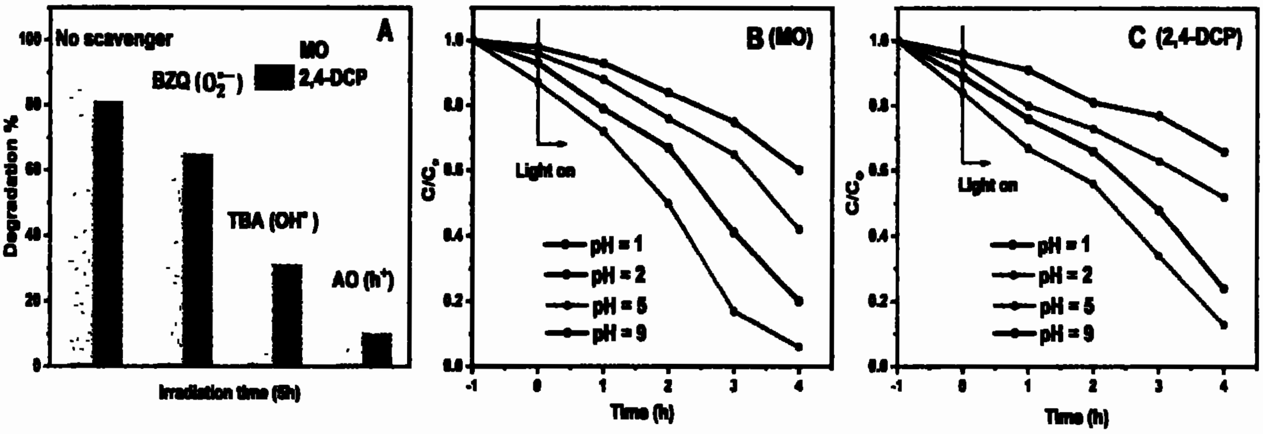

Figure 5.8. (A) Study of trapping test through 3.0% N-graphene/WO_3 photocatalyst on organics (MO and 2, 4-DCP) without scavenger and with scavengers i.e., ammonium oxalate (AO) for holes (h^+), tetra-butyl alcohol (TBA) for $OH^{\bullet}$ and benzoquinone (BZQ) for $O_2^{\bullet-}$, respectively. Effect of pH (pH = 1, 2, 5 and 9) on photodegradation of (B) MO and (C) 2, 4-DCP through 3.0% N-graphene/WO_3.

5.3.8. Proposed mechanism of photocatalyst

To elucidate the photocatalytic mechanism the valence (E_{VB}) and conduction edge potential (E_{CB}) plays a vital role in charge transfer process and calculated by following equations 5.3-5.4.

$$E_{VB} = \chi - E_e + 0.5\ E_g \qquad (5.3)$$

$$E_{CB} = E_{VB} - E_g \qquad (5.4)$$

Here χ, E_e and E_g are electronegativity of semiconductor, energy of free electron (4.5eV *vs.* NHE) and band gap energy of martial used, respectively. E_g of WO_3 and N-graphene was found to be ~2.6 and ~1.5 eV as measured by Tauc plot, respectively. Using above value E_{CB} and E_{VB} of WO_3 is calculated to be +0.79 and +3.39eV, respectively. According to literature, the E_{CB} and E_{VB} of N-graphene are to be −0.08 and +1.42 eV [228, 239].

The photocatalytic degradation of organic species was evaluated through as-synthesized material under visible light irradiation as revealed in Scheme 5.2. The light exposure simultaneously produces electron/hole pairs in WO_3/N-graphene composite. Hypothetically, photo induced electrons would transfer from E_{CB} of N-graphene to E_{CB} of WO_3, while holes (h^+) would move from E_{VB} of WO_3 to E_{VB} of N-graphene. The elevated concentration of electrons in E_{CB} of WO_3 can't react with O_2 to generate $O_2^{\bullet-}$ because the E_{CB} of WO_3 is more positive than redox potential $O_2/O_2^{\bullet-}$ (−0.33eV *vs.* NHE) [226]. On the other hand, the holes in VB of N-graphene suppressed the oxidation reaction owing to low E_{VB} of N-graphene than redox potential of $OH^{\bullet}/OH^-$ (+2.4eV. *vs.* NHE). Consequently, this conventional heterojunction behavior is not favorable to generate the radials ($O_2^{\bullet-}$, $OH^{\bullet}$) which are substantial to degrade the organics. To overcome these issues, Z-scheme is considered as an encouraging approach for photocatalytic removal of organic pollutants. In N-graphene/WO_3, the electron/hole pairs are generated under visible light irradiation. The photo generated electrons in WO_3 have tendency to move towards E_{VB} of N-graphene and increase the space separation between the photoexcited charge carriers and reduced the recombination rate as analyzed through quenching of PL intensities in composite sample. The accumulated electrons in N-graphene undergo reduction reaction to produce superoxide radicals ($O_2^{\bullet-}$) which on reacting with H_2O produce $OH^-/OH^{\bullet}$. Adsorbed molecules of MO on the surface of catalyst scavenged the electrons from CB of N-graphene and reduced to hydrazine derivatives which on reacting with $OH^{\bullet}/OH^-$decomposed into less toxic compounds. The collected holes in VB of WO_3 involved in oxidation reaction through reacting with OH^-/H_2O and produced hydroxyl radicals ($OH^{\bullet}$). These generated $OH^{\bullet}$ have appropriate potential to oxidize the organic molecules [246]. Therefore, the holes and hydroxyl radicals are the strategic elements to effectively oxidize the MO and 2, 4-DCP molecules and degraded into harmless compounds.

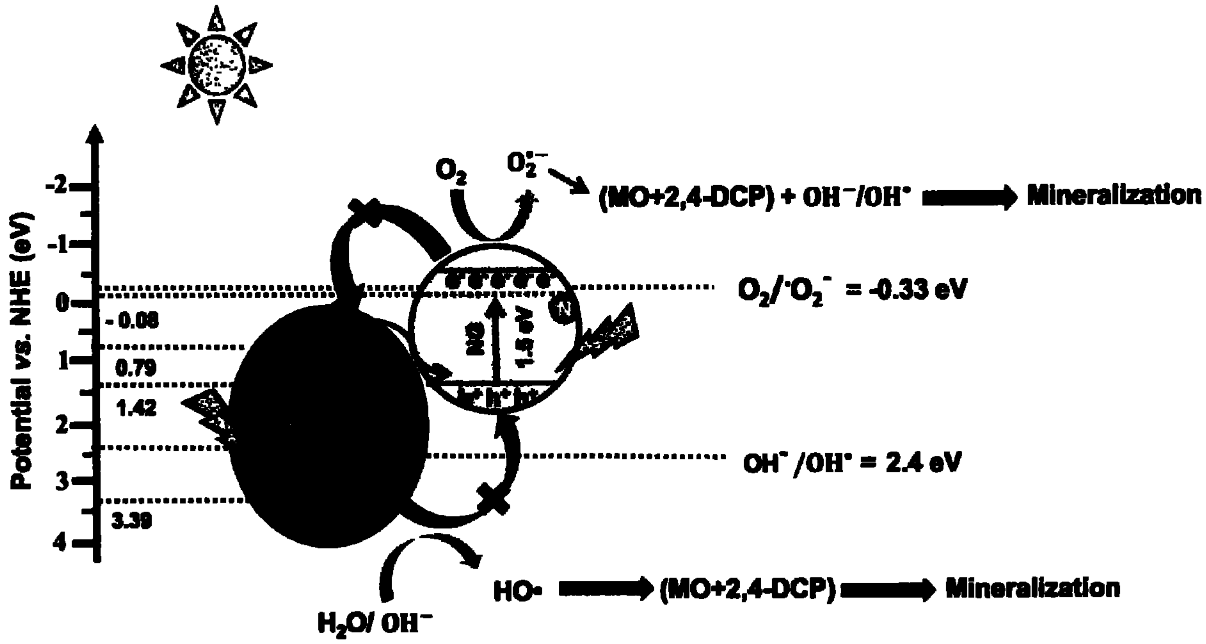

Scheme 5.2. Mechanism of degradation of organics under visible light irradiation over N-graphene/WO_3 nanocomposite.

5.4 Conclusions

In summary WO_3 and N-graphene/WO_3 composites with variable amount of N-graphene were fabricated through an efficient chemical method. The synthesized photocatalysts were considered as promising candidates for degradation of mixture of organics i.e. strong pollutants methyl orange (MO) and 2, 4 dichlorophenol (2,4-DCP). 3.0% N-graphene/WO_3 composite demonstrated excellent photocatalytic efficiency under visible light as well as good reusability. Results indicated that the increased photocatalytic performance is ascribed to significantly reduced the band gap of WO_3 and enhanced separation rate of electron-hole pairs owing to incorporation of N-graphene. Since the incorporated nitrogen into the skeleton of graphene sheets retained its sp^2 functionalization which effectively modified it into semiconductor material by opening its band gap. Moreover, the scavenger radials study suggested that OH• and h^+ are main active species to degrade the pollutants (MO and 2, 4-DCP). Therefore, N-graphene/WO_3 compound system showed excellent photocatalytic behavior for the mineralization of waste materials, would be the good choice in the future for numerous novel applications.

CHAPTER 6

Carbon qauantum dots modified 2D/2D MgO@G nanocomposites as an visible photocatalyst

6.1 Introduction

The organic dyes released from pharmaceutical, textile and food industries are very toxic and cause a serious threat to environmental pollutions [249]. For environmental protection, it is a noteworthy a great challenge to decompose the organic dyes present in industrial effluent into non-toxic material owing to their complex aromatic structure. The various wastewater treatment methods such as reverse osmosis, ultrafiltration, precipitation, flocculation etc used for decolorizing the organic pollutants [250].

Photocatalysis technique have been gaining tremendous attention as it easily degrade the dyes into simple and non-toxic material in the presence of solar irradiation [251]. Numerous semiconductors (TiO_2, NiO, ZnO, WO_3) have been widely used as photocatalyst for photo-degradation owing to their peculiar and fascination properties [252]. Magnesium oxide (MgO) with wide band gap (Eg = 2.5–8.0 eV) has high thermal conductivity , low refractive index and dielectric constant, which contribute its potential applications in fields of adsorption, paint, catalysis and so on. Recently, it is reported that the surface defects (superoxide O^{2-}) in MgO making it an interesting candidate for environmental remediation. The surface defects create a low position energy level between conduction and valence band when the Eg of magnesium oxide reflects the transition from valence (O^{2-}) to conduction band (Mg^{2+}). Thus, MgO photocatalyst easily generate the electron/hole pairs which contribute in photocatalytic activity under visible light source [253- 255]. Few defect sites and wide band gap are the main obstacle to limit its application in photocatalysis under visible light [251,254]. There are numerous methods (e.g doping, composite) to boost the photo-catalytic efficiency of MgO in visible light irradiation. To overcome the above mention issues, it was observed that graphene sheets play a significant role to boost the photocatalytic efficiency of MgO. Because the remarkable properties such as large surface area, high chemical stability and electron mobility of 2D graphene have allowed it to acquire outstanding progress in fields of photocatalytic applications [256]. Moradi, S. et al have reported that the MgO/ZnO/Graphene ternary composites exhibit higher photocatalytic efficiency (94%) against the sulfamethoxazole under UV light illumination [257]. Zeng, W. et al have investigate the 2D/2D MgO/graphene sheet composites degrade the methylene blue under visible light source [254].

Besides, the carbon quantum dots (CQDs) competent member of carbon family have shown great potential in photocatalytic application either as itself photocatalyst or with the combination of other materials. The CQDs play a diverse role in CQDs modified photocatalysts due to their size effect and optical features. Furthermore, CQDs also act as electron acceptor, increase light harvesting ability and retard the charge carriers' recombination in photo-chemical reaction [258,259]. Gholinejad, M. et al investigated that the prepared Pd stable NPs on MgO-CQDs at as a catalyst for Suzuki reaction [260].

In present work, 2D MgO 2D/2D MgO@G and CQDs/MgO@G with optimum content of CQD synthesized through co-precipitation and wet impegration method, respectively. CQDs/MgO/G exhibited remarkable excellent photocatalytic performance against Congo red under visible light source. The photocatalytic efficiency of CQDs/MgO@G enhanced on account of strong interfacial contact between 2D MgO and graphene sheets. Moreover, the incorporation of CQDs significantly enhanced the surface area which provides massive actives on its surface for adsorption of pollutants. Moreover, the effect of reactive species were also studied to explore the photocatalytic reaction. Consequently, this work provides path to develop several CQDs modified 2D/2D graphene base semiconductors for various effective environmental applications.

6.2 Materials and Synthesis

Graphite power, magnesium nitrate $Mg(NO_3)_2$, potassium permanganate ($KMnO_4$), phosphoric acid (H_3PO_4), hydrochloric acid (HCl), nitric acid (HNO_3), Congo red, hydrogen peroxide (H_2O_2), sodium hydroxide (NaOH) and citric acid were provided by Sigma-Aldrich.

6.2.1 Synthesis of 2D MgO sheets

4g of magnesium nitrate $Mg(NO_3)_2$ mixed in distilled water (100ml) under continuous string for 1 hr. Simultaneously, optimum amount of NaOH dissolved into distilled water until it reaches at pH= 3- 4. This solution drop-wise added into magnesium nitrate solution. After few minutes, a white precipitates were formed. These white precipitates washed with distilled water and dry at 60 °C to extract the extra ionic impurities. The obtained product was further annealed at 500°C for 2hrs.

6.2.2 Synthesis of graphene sheets and CQDs

The same method was used to synthesize the graphene sheets as earlier reported [261]. For synthesis of CQDS, 4g citric acid used as precursor was dissolved into 10ml distilled water under vigorous string and then transfer this solution into Teflon autoclave for hydrothermal treatment (180 °C for 4 hrs). Finally, the obtained product was centrifuge for 10mints to eradicate the larger particles.

6.2.3 Synthesis of 2D-2D Mgo@G and CQDs/MgO@G nanocomposites

The 0.12g of graphene sheets was dissolved into distilled water and sonicate for 1hr to get the homogenous solution. Then, the optimum amount of MgO poured into graphene solution and left for 1 hr under string. The solution was centrifuge at 5000rpm for 15mints and dry at 60°C to get the binary composite (MgO@G). Same producer was employed to prepare the ternary composites with different concentration of CQDs.

6.2.4 Characterization Techniques

The structural and phase information of synthesized samples were obtained through XRD (X'pert PRO MPD, PANalytical with Cu K_α radiation and wavelength =1.54Å). The SEM (MIR3, TESCAN) with EDX was used to investigate the surface morphologies of nano-materials. The FTIR (ALPHA II, Bruker) was employed to analyze the functional group present in the prepared materials. The optical properties were studied with help of UV-2600 spectrometer, Shimadzu, Japan) in the range of 200-800nm.

6.2.5 Photocatalytic activity

The photo catalytic efficiency of all samples were investigated by detoxifying the organic dye (Congo red) under visible light region. For this purpose, the appropriate amount of photocatalyst was dissolved into dye solution (50ml) under constant string and then kept into dark region for half hour to get the adsorption-desorption equilibrium between the organic dye and photocatalyst' surface. 5ml solution was collected before exposing in the visible light irradiation for 3hrs. After regular time irradiation, the solution was collected and centrifuge to separate the photo-catalyst. The UV-vis spectrometer was employed on the solution for further analysis. The degradation parentage of Congo red was determined using formula

$$Degradation\ \% = (1 - Ct/C_0) \times 100\% \qquad (6.1)$$

The C_0 and C_t represents the initial concentration of dye and concentration of dye after specific time (t), respectively.

6.3 Results and dissussion

6.3.1 Structural analysis

The XRD pattern (fig.6.1) depicts the crystal structure of MgO sheets, MgO@G and CQDs/ MgO@G with different concentration of CQDs. XRD diffraction peaks of MgO at $2\theta = 38°$ (111), 42.8° (200), 62.2° (220) and 78.4° (222) well matched with (JCPDS NO. 45-09) [262,254]. The absence of secondary phase confirm the formation of pure MgO. In XRD profile of 2D/2D MgO@G, an additional intense diffraction peak at $2\theta = 26.5°$ (002) corresponding to the stacked graphene sheets [263] is the clear evidence of loading MgO on the graphene sheets. Moreover, it can be clearly seen in CQDs/ MgO@G composites (fig.6.1 c-d) that the peak intensity of graphene sheets suppress due to induction of CQDs. This feature suggest that long regular stack of graphene sheets is destroyed causes the weak diffraction peak. The dramatically weak diffraction peak show the good exfoliation efficiency between the samples [264,265].Therefore, the CQDs act as intercalator to retards the agglomeration of sheets and enhance the surface area which is beneficial for photocatalytic activity (clearly seen in SEM images) [262]. It was also noticed that in all doped CQDs/ MgO@G composites, the slightly peaks shifting indicates the successful incorporation of dopants.

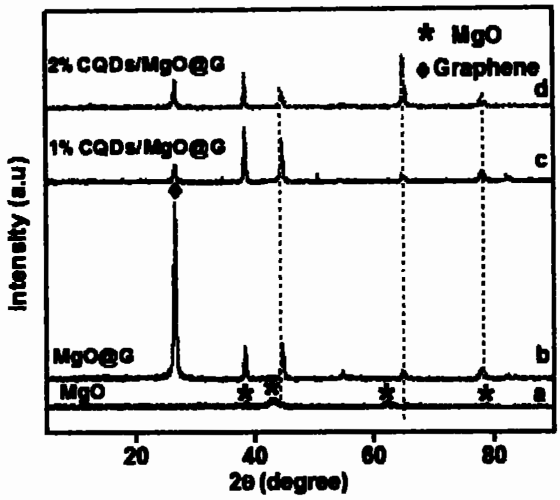

Figure 6.1: XRD pattern of (a) MgO sheets, (b) 2D-2D MgO@G, (c) 1% CQDs/ MgO@G and (d) 2% CQDs/ MgO@G nanocomposite.

6.3.2 Raman Spectra

The Raman spectra of MgO@G and 2% CQDs/ MgO@G is depicted in fig. 6.2. In both 2D-2D MgO@G and 2% CQDs/ MgO@G composites, the D band is located at 1559 and 1570 cm^{-1}, while the G band centered at 1320cm^{-1} and 1336cm^{-1}, respectively. It can be clearly observed, the peak of D and G band is slightly broad and shifted in 2% CQDs/MgO@G composite after inducing the CQDs. The Id/Ig value for 2% CQDs/MgO@G was found to be (1.15) higher than 2D-2DMgO@G. The large Id/Ig value indicates the massive surface defects [266] which promote the charge carriers on the surface of photocatalyst for redox chemical reaction. Besides, the Raman peak near to 200 cm^{-1} is assigned to MgO simultaneously noticed in both samples, showing the successful formation of nano-composites [267].

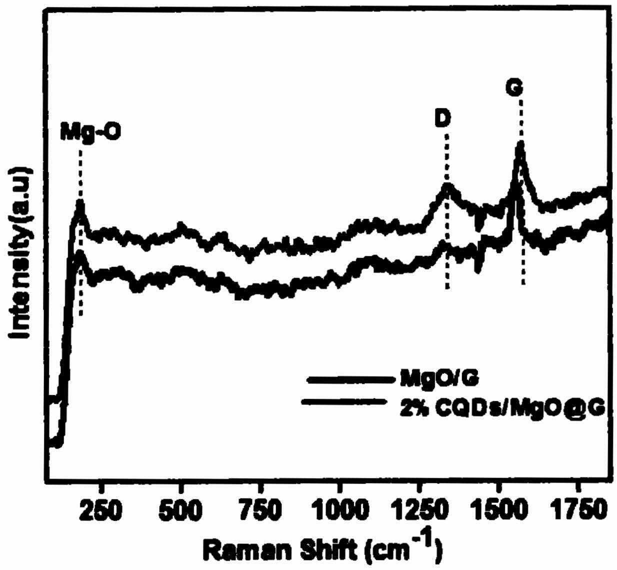

Figure 6.2: Raman spectra of MgO sheets and 2% CQDs/ MgO@G nanocomposite

6.3.3 FTIR

Figure 6.3 shows the FTIR spectra of pure MgO and 2% CQDs/ MgO@G ternary nanocomposite. It is well known that the carbon dioxide and water molecules are absorbed on the surface of MgO from atmosphere because of their acid-base surface properties [268,269]. Therefore, in both prepared samples, the absorption signals at 1640cm^{-1} and 2366 cm^{-1} corresponds to the O-H bending and CO_2. [269,270] .The Mg-O stretching vibrations in the range of 670-590 cm^{-1} observed in all samples [271]. Further, In CQDs/MgO@G nanocomposite, the peaks at 1528 cm^{-1} and 1447 cm^{-1} is ascribed to skeleton of graphene sheets [272]. Besides, the signals at 1705 cm^{-1}, 1383 cm^{-1} and board peak at 1200 cm^{-1} attributed to the stretching vibration of C=O, C-OH and C-O-C groups, respectively due to presence of CQDs [273,274]. An additional peak at 973 cm^{-1} indicates the vibrational mode Mg-O-C [275] which confirm the formation of ternary nanocomposites successfully.

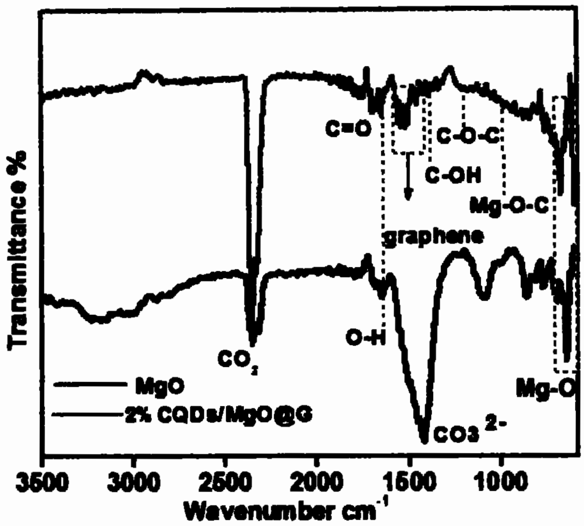

Figure.6.3: FTIR spetra of MgO sheets and 2% CQDs/ MgO@G nanocomposites

6.3.4 Morphological study

The surface morphology of graphene, MgO, MgO@G, CQDs/MgO@G was investigated through Scanning electron microscopy and obtained results depicted in figure 6.4. The transparent and crumpled graphene sheets with slightly folded edge seen in figure.6.4a. Fig.6.4b demonstrate that the MgO also have sheets like morphology with highly sharp pointed fold edges. In 2D-2D MgO@G nanocomposites (fig.6.4c), MgO overlapped with gaphene sheets due to good mixing integrity of MgO and graphene sheets resulting to form a long stacked sheets with high surface area. These staked sheets were exfoliated with the incorporation of CQDs as agreed with XRD pattern. Besides, the induce CQDs increased wrinkled on sample with large surface area (fig.6.4d) which play an effective role to increase the catalytic efficiency.

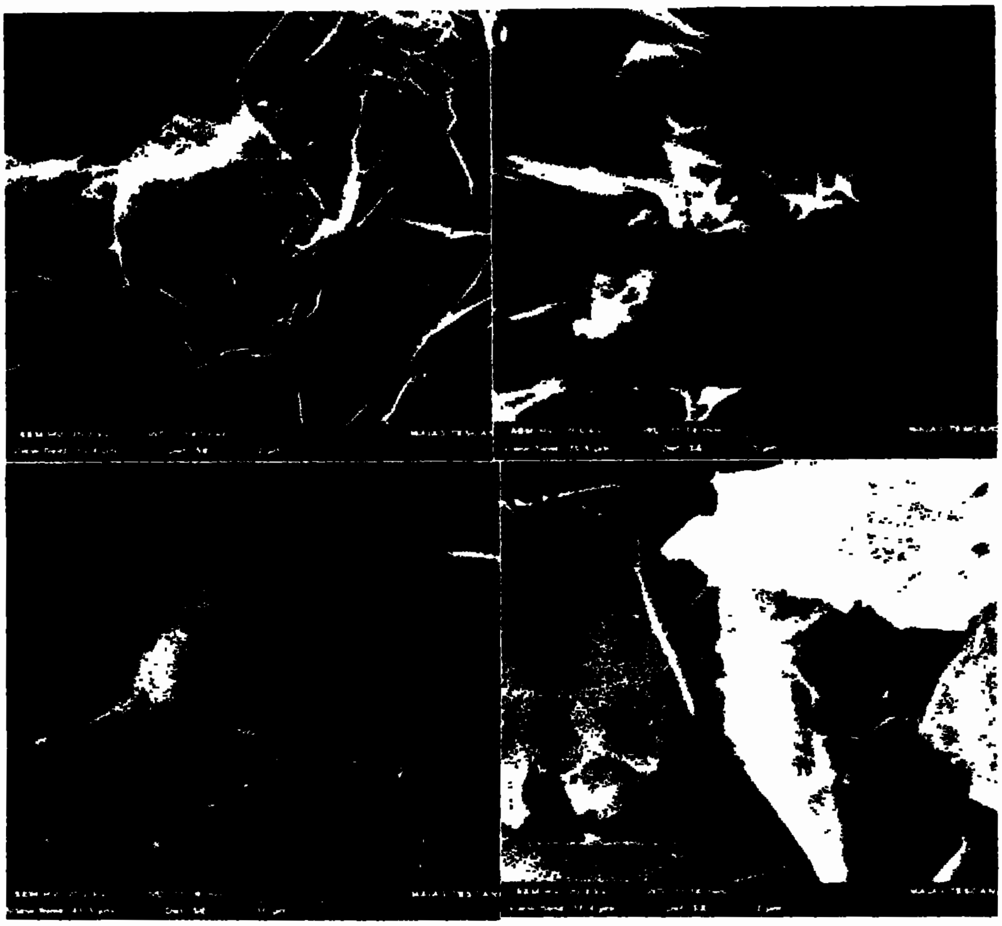

Figure. 6.4: SEM images of of graphene sheets (a) , MgO sheeets (b) MgO@G (c) and 2%CQDs/MgO@G (d).

6.3.5 Energy dispersive x-ray (EDX)

The energy dispersive x-rays was used to determine the elemental compositions of synthesized materials (figure 6.5). In both MgO@G and CQDs/MgO@G spectra, the peaks of C, O, Mg are observed which indicates the formation of binary and ternary composites. The obtained results suggest the purity of synthesized samples as no extra peak for any other impurity was detected. The weight and atomic parentage of binary and ternary composites are presented in table.6.1.

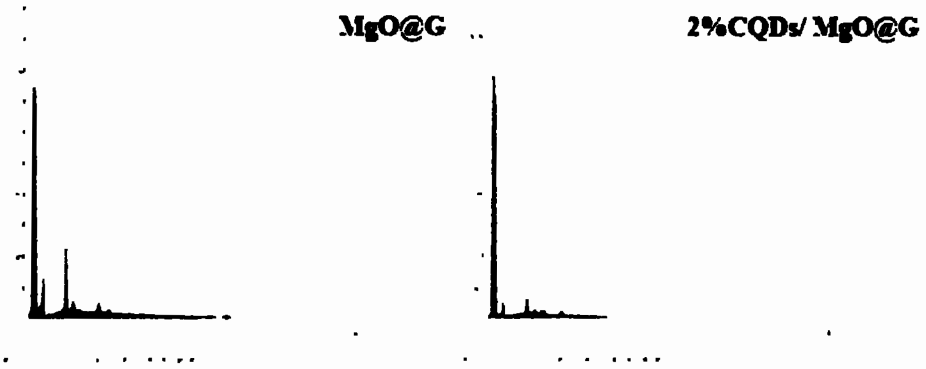

Figure.6.5: EDX pattern of MgO@G and 2% CQDs/MgO@G

Table.6.1: Atomic and elemental composition of MgO@G and 2% CQDs/MgO@G

Elements	MgO @G		2% CQDs/MgO@G	
	Mass%	Atomic%	Mass%	Atomic%
Mg	5.65	3.08	2.39	1.24
O	21.99	18.25	12.71	10.05
C	70.25	77.67	83.65	88.14
Total	97.89	99	98.75	99.43

6.3.6 UV-vis absorption study

The optical absorbance properties associated with energy band gap of prepared samples were examined through UV-vis spectroscopy as show in figure 6.6. The absorption edge of pure MgO is observed in ultraviolet region at the 267nm attributed to the charge transferring from valence band (O 2p) to conduction band (Mg 3s and 3p state). The band gap of MgO is found to be 4.6eV as calculated from E_g=1240/λ_{abs}. As mostly reported in literature, MgO is an insulator with wide band gap (7.8eV). MgO with narrow band gap corresponding to oxygen deficiency which leads to formation of new energy level. Thus, oxygen vacancies enhance the photocatalytic activity of MgO

[264]. Furthermore, it could be obviously seen that absorption edge of nanocomposites is shifted towards the visible region corresponding to the decline energy band gap. The calculated gap bap values of binary and ternary composites are to be 2.98eV, 2.82, 2.7eV, respectively. These intriguing modifications in band gap of MgO owing to presence of graphene sheets and CQDs, resulting the formation of chemical bonds (Mg-O-C) making it an efficient photocatalyst to utilize the solar irradiation for photocatalysis.

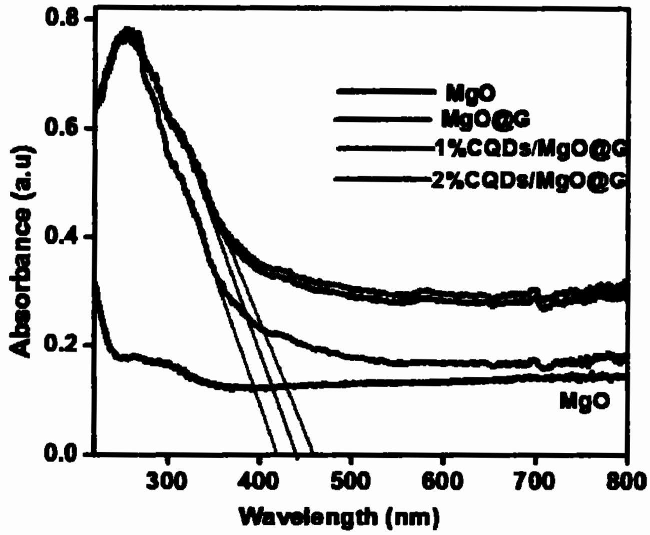

Figure.6.6: Absorption spectra of MgO sheets, 2D-2D MgO@G, 1% CQDs/ MgO@G and 2% CQDs/ MgO@G nanocomposites.

6.3.7 Photocatalytic performance

The photocatalytic efficiency of Pure MgO, 2D-2DMgO@G, 1%CQDs/MgO@G and 2% CQDs/MgO@G nanocomposites were evaluated by decolorizing the Congo red under visible light illumination (fig. 6.7A). The degradation of Congo red was negligible without any photocatalyst. The pure MgO decomposed Congo red ~21% on account of few surface defects. The MgO have required valence and conduction edge position (+3.8eV and -0.7eV Vs NHE) for redox reaction, but its wide band gap is responsible for its low degradation efficiency. The photocatalytic properties of MgO in visible region was enhanced through inducing scavenging materials to attenuate the energy band gap on account of synergistic effect. Subsequently, 2D-2D MgO@G, 1% CQDs/MgO@G and 2%CQDs/MgO@G nano-composites decolorized the Congo red 75.5%, 89.9% and 99%, respectively. Because the crumpled surface of CQDs/MgO@G (as shown in SEM image) provides the massive active site for maximum adsorption of organic molecules. Besides, the graphene sheets (due to long pi-conjugates) and CQDs also act as electron- sink causes to retard the recombination rate of photogenerated electron/hole pairs and enhance their transferring rate. These charge carriers effectively proceed the redox reaction to decompose the organic molecules.

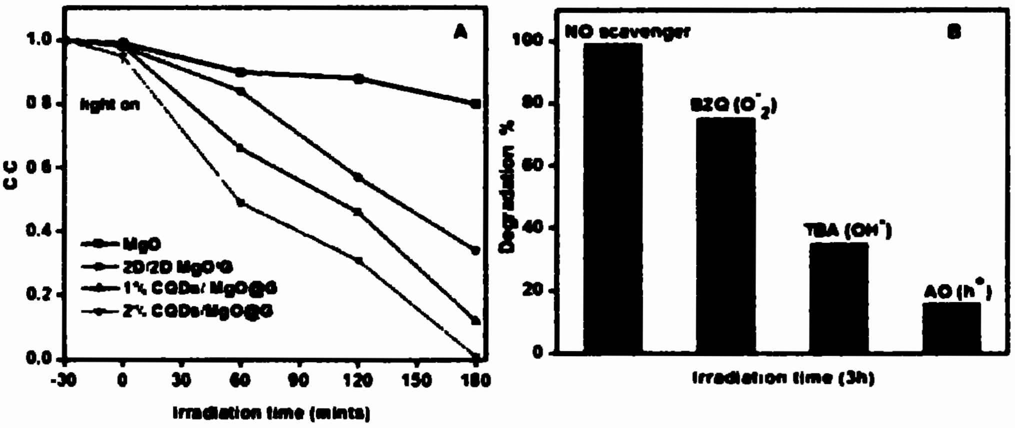

Firgure. 6.7: (A) Photocatalytic degradation % of Congo red through of MgO sheets, 2D-2D MgO@G, 1%CQDs/ MgO@G and 2%CQDs/MgO@G nano omposites. (B) Controlled experiment using different radical scavengers.

6.3.8 Role of reactive species on photodegradation

The contribution of reactive species during the photodegradation of Congo red through 2%CQDs/ MgO@G nanocomposite were determined by using trapping test. Acontrolled experiment was carried out using benzoquinone (BZQ), ammonium oxalate (AO) and tetra-butyl alcohol (TBA) for $O_2^{\cdot-}$, h^+ and $OH^{\bullet}$ respectively as radical sanevgers (fig.6.7B). The results demonstrated that the addition of TBA and AO as radical sanevgers significantly impede the degradation efficiency which indicate that $OH^{\bullet}$and h^{+} are main active agents in photo catalytic reaction. Though, the phto catalytic reaction is slight effeted by BZQ) as $O_2^{\bullet -}$ suggesting that $O_2^{\bullet -}$ is not play an imerative role for detoxifying the Congo red.

6.3.9 Photocatalytic mechanism

To demonstrate the photocatalytic activity of CQDs/MgO@G, the valence and conduction band edge position of samples are key parameters in charge transferring process and was estimated using formula [276]

$$E_{VB} = X - E_e + 0.5E_g \qquad (6.2)$$

$$E_{CB} = E_{VB} - E_g \qquad (6.3)$$

Here, the E_e, X and E_g represents the electron affinity (4.5eV), electronegativity (2.05eV) and energy band gap (4.6eV) of MgO, respectively. The VB and CB edge position of MgO was found to be +4.45eV and -0.7eV, respectively. Scheme.6.1 depict the photocatalytic mechanism to degrade the Congo red by exposing the photocatalyst in visible light irradiation. Mostly, the MgO with wide band gap (4.6eV) is an active under UV irradiation. However, the graphene sheet and CQDs tuned the MgO into visible light active material by remarkable reducing its energy band gap (2.7eV). The CQDs/MgO@G photo catalyst with light exposure simultaneously produce electron/hole pairs. These electrons in CB of MgO efficiently captured by CQDs and graphene sheets because both act as electron scavenger, resulting to suppress the recombination rate of charge carriers. The captured electrons of MgO reactive with oxygen and to form superoxide $(\bullet O^{2-})$. The holes in MgO VB band with edge position +4.48eV vs NHE higher than required oxidation potential ($OH^-/\bullet OH = 2.3$ eV/vs. NHE) interact with H_2O/OH^- to form hydroxide radials ($\bullet OH$). These reactive species $\bullet O^{2-}$ and $\bullet OH$ degrade the organic molecules at catalyst surface.

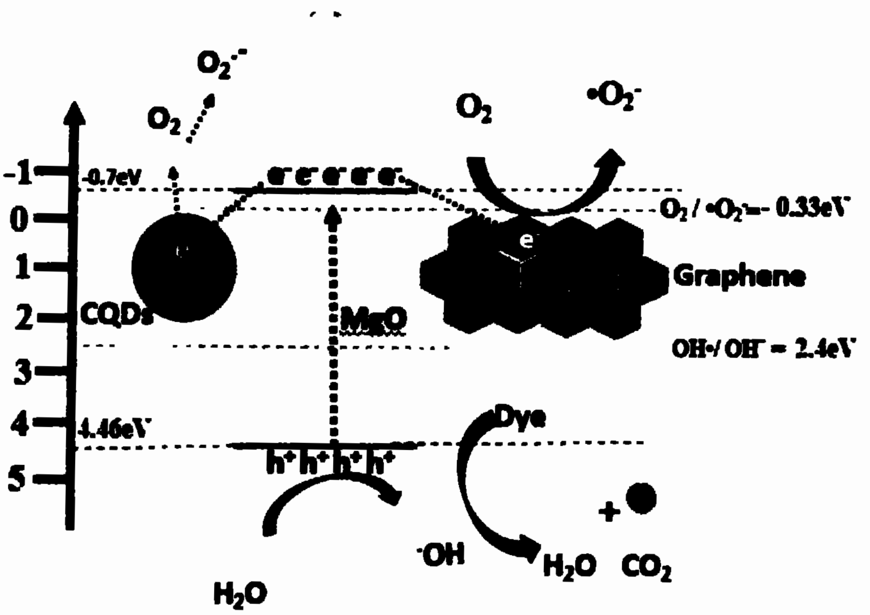

Scheme.6.1: Schematic diagram of photodegradation of Congo red through CQDs/MgO@G

6.4 Conclusion

In summary 2D MgO, binary 2D/2D MgO@G and ternary CQDs/MgO@G composites with variable amount of CQDs were synthesized through effective chemical process. The synthesized binary 2D/2D MgO@G enhanced photocatalytic efficiency toward the Congo red due to strong interfacial interaction. Whereas, the ternary CQDs/MgO@G composite exhibited higher photocatalytic performance than 2D/2D binary composite under visible light source. Results revealed that the increased photocatalytic performance of ternary composites is attributed to significantly decline the band gap of MgO and recombination rate of charge carriers owing to graphene sheets and CQDs which act as an electron scavenger. The incorporated CQDs in ternary composites also enlarge the surface area which offers massive active sites for adsorption of organic molecules. Besides, the scavenger radials experiment proposed that h^+ and OH• are reactive species to decompose the pollutant (Congo red). Consequently, compound system exhibited superior photocatalytic behavior for the mineralization of waste materials, would be a good choice in future for various novel applications.

CHAPTER 7

Conclusion

In present era, the researcher's intention has been increased towards the energy crisis and environmental remediation. The researchers are trying to develop effective and efficient techniques to deals with environmental challenges. Photocatalysis is a cost effective, safe and easily handle technique for environmental and energy crisis. The researchers still making this technique more practical and cost effective by synthesizing visible light active catalysts, both for energy and environmental applications. In this research work, I have prepared numerous graphene based semiconductor nanocomposites and applied them for water waste treatment. The synthesized nanocomposites were exhibited enhance photocatalytic efficiency under visible light source.

Publication-1 NiO sheets and 2D/2D graphene/NiO nanocomposites were prepared via chemical method to boost the photocatalytic activity towards the degradation of MO under visible light. The incorporation of graphene sheets improved the photocatalytic performance of 2D NiO sheets from 30% to 75% owing to strong interfacial contact 2D/2D graphene/NiO composites.

Publiation-2 WO_3 was modified with N-graphene to work with visible light induction for decomposition of strong mixture of pollutants (2,4 DCP and MO). The induced N-graphene in WO_3 enhance the surface area and supress the charge carriers' recombination rate cause to improve photocatalytic activity.Moreover, the photocatalytic efficiency of the binary composites was greatly increased owing to nitrogen functionalities in N-graphene.

Projcet-3 Ternary CQDs/MgO@G and binary 2D/2D MgO@G nanocomposites were synthesized to remarkably tune the band gap of MgO. Reduced band gap making it a visible light responsive catalyst for detoxifying the Congo red. The synthesized 2D/2D MgO@G nanocomposites provide large surface area and more active sites, which effectively inrcease the photocatalytic performance against Congo red in the presene of visible light. It was also noticed that induce CQDs act as electron scavenger leads to enhance degradation efficiency of ternary CQDs/MgO@G composites again Congo red than binary composite (MgO@G).

Table 7.1 Outcomes of photocatalytic performance of various synthesized materials.

Catalyst	**Photodegradation of organics pollutants**	**Degradation (%)**	**Degradation Time**	**Light source**
2D/2D Grpahene/NiO composite	MO	75%	4h	Visible
N-graphene/WO_3 composite	(2,4DCP, MO)	81 (2,4DCP), 94 (MO)	5h	Visible
CQDs/ 2D/2DMgO@G composite	Congo Red	~99	3h	Visible

It is concluded that the graphene sheets and 2D semiconductors have great potential towards the numerous photocatalytic applications.

Future perspective

This research project defines the significance of graphene sheets in modifying semiconductors for photocatalytic applications. Considering its tremendous degradation efficiency,

- The efficient and novel nanocomposites with tremendous features can be used for deduction of environmental remediation and industrial effluents under solar light.
- These materials can be further explored for the reduction of carbon diode level in environment.
- The synthesized nanomaterials have great potential for cost effective hydrogen production through water splitting process.
- It is also proposed that detailed electronic properties of nanomaterial can be studied by employing advanced characterization techniques such as synchrotron radiation X-ray photoelectron spectroscopy (SR-XPS), X-ray absorption spectroscopy (XAS).

References

[1] Liu, J., Liu, G., & Liu, W. (2014). Preparation of water-soluble β-cyclodextrin/poly (acrylic acid)/graphene oxide nanocomposites as new adsorbents to remove cationic dyes from aqueous solutions. *Chemical Engineering Journal*, *257*, 299-308.

[2] Wintgens, T., Salehi, F., Hochstrat, R., & Melin, T. (2008). Emerging contaminants and treatment options in water recycling for indirect potable use. *Water Science and Technology*, *57*(1), 99-107.

[3] Gupta, V. K., Ali, I., Saleh, T. A., Nayak, A., & Agarwal, S. (2012). Chemical treatment technologies for waste-water recycling—an overview. *Rsc Advances*, *2*(16), 6380-6388.

[4] Connell, D. W., Wu, R. S., Richardson, B. J., & Lam, P. K. (2009). Chemistry of organic pollutants, including agrochemicals. *Environ Ecol Chem*, *6*, 181.

[5] Kumar, V., Kim, K. H., Park, J. W., Hong, J., & Kumar, S. (2017). Graphene and its nanocomposites as a platform for environmental applications. *Chemical Engineering Journal*, *315*, 210-232.

[6] Gaya, U. I., & Abdullah, A. H. (2008). Heterogeneous photocatalytic degradation of organic contaminants over titanium dioxide: a review of fundamentals, progress and problems. *Journal of photochemistry and photobiology C: Photochemistry reviews*, *9*(1), 1-12.

[7] Chong, M. N., Jin, B., Chow, C. W., & Saint, C. (2010). Recent developments in photocatalytic water treatment technology: a review. *Water research*, *44*(10), 2997-3027.

[8] Ajmal, A., Majeed, I., Malik, R. N., Idriss, H., & Nadeem, M. A. (2014). Principles and mechanisms of photocatalytic dye degradation on TiO 2 based photocatalysts: a comparative overview. *Rsc Advances, 4*(70), 37003-37026.

[9] Saravanan, R., Gracia, F., & Stephen, A. (2017). Basic principles, mechanism, and challenges of photocatalysis. In *Nanocomposites for visible light-induced photocatalysis* (pp. 19-40). Springer, Cham.

[10] Gnanaprakasam, A., Sivakumar, V. M., & Thirumarimurugan, M. (2015). Influencing parameters in the photocatalytic degradation of organic effluent via nanometal oxide catalyst: a review. *Indian Journal of Materials Science, 2015.*

[11] Tahir, M. B., Sohaib, M., Sagir, M., & Rafique, M. (2020). Role of Nanotechnology in Photocatalysis. *Reference Module in Materials Science and Materials Engineering.*

[12] Kumar, S., Ahlawat, W., Bhanjana, G., Heydarifard, S., Nazhad, M. M., & Dilbaghi, N. (2014). Nanotechnology-based water treatment strategies. *Journal of nanoscience and nanotechnology, 14*(2), 1838-1858.

[13] Tahir, M. B., Iqbal, T., Rafique, M., Rafique, M. S., Nawaz, T., & Sagir, M. (2020). Nanomaterials for photocatalysis. In *Nanotechnology and Photocatalysis for Environmental Applications* (pp. 65-76). Elsevier.

[14] Blanco-Galvez, J., Fernández-Ibáñez, P., & Malato-Rodríguez, S. (2007). Solar photocatalytic detoxification and disinfection of water: recent overview.

[15] Ameta, R., Solanki, M. S., Benjamin, S., & Ameta, S. C. (2018). Photocatalysis. In *Advanced oxidation processes for waste water treatment* (pp. 135-175). Academic Press.

[16] Khan, M. M., Adil, S. F., & Al-Mayouf, A. (2015). Metal oxides as photocatalysts. *Journal of Saudi Chemical Society*, *19*(5), 462-464.

[17] Karthikeyan, C., Arunachalam, P., Ramachandran, K., Al-Mayouf, A. M., & Karuppuchamy, S. (2020). Recent advances in semiconductor metal oxides with enhanced methods for solar photocatalytic applications. *Journal of Alloys and Compounds*, *828*, 154281.

[18] Darkwah, W. K., & Oswald, K. A. (2019). Photocatalytic applications of heterostructure graphitic carbon nitride: pollutant degradation, hydrogen gas production (water splitting), and CO 2 reduction. *Nanoscale research letters*, *14*(1), 1-17.

[19] Low, J., Yu, J., Jaroniec, M., Wageh, S., & Al-Ghamdi, A. A. (2017). Heterojunction photocatalysts. *Advanced materials*, *29*(20), 1601694.

[20] Ge, J., Zhang, Y., Heo, Y. J., & Park, S. J. (2019). Advanced design and synthesis of composite photocatalysts for the remediation of wastewater: A review. *Catalysts*, *9*(2), 122.

[21] Huang, D., Chen, S., Zeng, G., Gong, X., Zhou, C., Cheng, M., ... & Li, J. (2019). Artificial Z-scheme photocatalytic system: What have been done and where to go?. *Coordination Chemistry Reviews*, *385*, 44-80.

[22] Xu, Q., Zhang, L., Yu, J., Wageh, S., Al-Ghamdi, A. A., & Jaroniec, M. (2018). Direct Z-scheme photocatalysts: Principles, synthesis, and applications. *Materials Today*, *21*(10), 1042-1063.

[23] Xu, Q., Zhang, L., Cheng, B., Fan, J., & Yu, J. (2020). S-scheme heterojunction photocatalyst. *Chem*, *6*(7), 1543-1559.

[24] Ge, M., & Li, Z. (2017). Recent progress in Ag3PO4-based all-solid-state Z-scheme photocatalytic systems. *Chinese Journal of Catalysis*, *38*(11), 1794-1803.

[25] Zhou, P., Yu, J., & Jaroniec, M. (2014). All-solid-state Z-scheme photocatalytic systems. *Advanced Materials*, *26*(29), 4920-4935.

[26] Xia, X., Song, M., Wang, H., Zhang, X., Sui, N., Zhang, Q., ... & William, W. Y. (2019). Latest progress in constructing solid-state Z scheme photocatalysts for water splitting. *Nanoscale*, *11*(23), 11071-11082.

[27].Murillo-Sierra, J. C., Hernández-Ramírez, A., Zhao, Z. Y., Martínez-Hernández, A., & Gracia-Pinilla, M. A. (2021). Construction of direct Z-scheme WO3/ZnS heterojunction to enhance the photocatalytic degradation of tetracycline antibiotic. *Journal of Environmental Chemical Engineering*, *9*(2), 105111.

[28] Zhou, S., Hou, M., Sun, Y., Zhao, W., Wang, H., Guo, Q., ... & Zhao, J. (2021). Ultrahigh-performance visible-light photodegradation enabled by direct Z-scheme AgI/(Na, F)–C3N4 composites. *Composites Part B: Engineering*, *224*, 109200.

[29] Low, J., Yu, J., & Jiang, C. (2020). Design and fabrication of direct Z-scheme photocatalysts. In *Interface Science and Technology* (Vol. 31, pp. 193-229). Elsevier.

[30] Raizada, P., Kumar, A., & Singh, P. (2020). Graphitic carbon nitride-based new advanced materials for photocatalytic applications. *Curr Anal Chem*, *16*, 1-00.

[31] Raizada, P., Kumar, A., & Singh, P. (2021). Graphitic carbon nitride-based new advanced materials for photocatalytic applications. *Current Analytical Chemistry*, *17*(2), 150-165.

[32] Sobana, N., Selvam, K., & Swaminathan, M. (2008). Optimization of photocatalytic degradation conditions of Direct Red 23 using nano-Ag doped TiO2. *Separation and Purification Technology*, *62*(3), 648-653.

[33] Rajabi, H. R., Khani, O., Shamsipur, M., & Vatanpour, V. (2013). High-performance pure and Fe3+-ion doped ZnS quantum dots as green nanophotocatalysts for the removal of malachite green under UV-light irradiation. *Journal of hazardous materials*, *250*, 370-378.

[34] Reza, K. M., Kurny, A. S. W., & Gulshan, F. (2017). Parameters affecting the photocatalytic degradation of dyes using TiO 2: a review. *Applied Water Science*, *7*(4), 1569-1578.

[35] Beydoun, D., Amal, R., Low, G., & McEvoy, S. (1999). Role of nanoparticles in photocatalysis. *Journal of Nanoparticle Research*, *1*(4), 439-458.

[36] Alkaykh, S., Mbarek, A., & Ali-Shattle, E. E. (2020). Photocatalytic degradation of methylene blue dye in aqueous solution by MnTiO3 nanoparticles under sunlight irradiation. *Heliyon*, *6*(4), e03663.

[37] Ebrahimi, R., Maleki, A., Zandsalimi, Y., Ghanbari, R., Shahmoradi, B., Rezaee, R., ... & Giahi, O. (2019). Photocatalytic degradation of organic dyes using WO3-doped ZnO nanoparticles fixed on a glass surface in aqueous solution. *Journal of Industrial and Engineering Chemistry*, *73*, 297-305.

[38] Neppolian, B., Choi, H. C., Sakthivel, S., Arabindoo, B., & Murugesan, V. (2002). Solar/UV-induced photocatalytic degradation of three commercial textile dyes. *Journal of hazardous materials*, *89*(2-3), 303-317.

[39] Liu, Y., Ohko, Y., Zhang, R., Yang, Y., & Zhang, Z. (2010). Degradation of malachite green on Pd/WO3 photocatalysts under simulated solar light. *Journal of hazardous materials*, *184*(1-3), 386-391.

[40] Seshadri, H., Chitra, S., Paramasivan, K., & Sinha, P. K. (2008). Photocatalytic degradation of liquid waste containing EDTA. *Desalination, 232*(1-3), 139-144.

[41] Zhu, C., Li, Y., Yang, Y., Chen, Y., Yang, Z., Wang, P., & Feng, W. (2020). Influence of operational parameters on photocatalytic decolorization of a cationic azo dye under visible-light in aqueous Ag3PO4. *Inorganic Chemistry Communications, 115*, 107850.

[42] Khan, I., Saeed, K., Ali, N., Khan, I., Zhang, B., & Sadiq, M. (2020). Heterogeneous photodegradation of industrial dyes: An insight to different mechanisms and rate affecting parameters. *Journal of Environmental Chemical Engineering*, 104364.

[43] Baruah, A., Chaudhary, V., Malik, R., & Tomer, V. K. (2019). Nanotechnology based solutions for wastewater treatment. In *Nanotechnology in Water and wastewater treatment* (pp. 337-368). Elsevier.

[44] Ukoba, K. O., Eloka-Eboka, A. C., & Inambao, F. L. (2018). Review of nanostructured NiO thin film deposition using the spray pyrolysis technique. *Renewable and Sustainable Energy Reviews, 82*, 2900-2915.

[45] Singh, S. D., Nand, M., Das, A., Ajimsha, R. S., Upadhyay, A., Kamparath, R., ... & Ganguli, T. (2016). Structural, electronic structure, and band alignment properties at epitaxial NiO/Al2O3 heterojunction evaluated from synchrotron based X-ray techniques. *Journal of Applied Physics, 119*(16), 165302.

[46] Diallo, A., Kaviyarasu, K., Ndiaye, S., Mothudi, B. M., Ishaq, A., Rajendran, V., & Maaza, M. (2018). Structural, optical and photocatalytic applications of biosynthesized NiO nanocrystals. *Green Chemistry Letters and Reviews, 11*(2), 166-175.

[47] Hashem, M., Saion, E., Al-Hada, N. M., Kamari, H. M., Shaari, A. H., Talib, Z. A., ... & Kamarudeen, M. A. (2016). Fabrication and characterization of semiconductor nickel oxide (NiO) nanoparticles manufactured using a facile thermal treatment. *Results in physics*, *6*, 1024-1030.

[48] Diao, C. C., Huang, C. Y., Yang, C. F., & Wu, C. C. (2020). Morphological, optical, and electrical properties of p-type nickel oxide thin films by nonvacuum deposition. *Nanomaterials*, *10*(4), 636.

[49] Haider, A. J., Al-Anbari, R., Sami, H. M., & Haider, M. J. (2019). Photocatalytic activity of nickel oxide. *Journal of Materials Research and Technology*, *8*(3), 2802-2808.

[50] UR, S., CR, R. K., MS, K., Betageri, V. S., MS, L., Veerapur, R., ... & Kollur, S. P. (2021). Biogenic Synthesis of NiO Nanoparticles Using Areca catechu Leaf Extract and Their Antidiabetic and Cytotoxic Effects. *Molecules*, *26*(9), 2448.

[51] Li, Y., Liu, Z., Li, J., Ruan, M., & Guo, Z. (2020). An effective strategy of constructing a multi-junction structure by integrating a heterojunction and a homojunction to promote the charge separation and transfer efficiency of WO 3. *Journal of Materials Chemistry A*, *8*(13), 6256-6267.

[52] Zou, Y. S., Zhang, Y. C., Lou, D., Wang, H. P., Gu, L., Dong, Y. H., ... & Zeng, H. B. (2014). Structural and optical properties of WO3 films deposited by pulsed laser deposition. *Journal of alloys and compounds*, *583*, 465-470.

[53] Dang, X., Jiang, X., Zhang, T., & Zhao, H. (2021). WO3 Inversce Opal Photonic Crystals: Unique Property, Synthetic Methods and Extensive Application. *Chinese Journal of Chemistry*, *39*(6), 1706-1715.

[54].Thiyagarajan, T., Deivasigamani, V., Raj, M., Joseph, C., Dheivasigamani, T., Palanivel, B., ... & Shkir, M. (2021). Facile synthesis and characterization of WO3/CuWO4 nanocomposites for the removal of toxic methylene blue dye. *Korean Journal of Chemical Engineering*, *38*(5), 952-965.

[55] Ahmadi, M., Younesi, R., & Guinel, M. J. (2014). Synthesis of tungsten oxide nanoparticles using a hydrothermal method at ambient pressure. *Journal of Materials Research*, *29*(13), 1424-1430.

[56] Wang, J., Tu, Y., Yang, L., & Tolner, H. (2016). Theoretical investigation of the electronic structure and optical properties of zinc-doped magnesium oxide. *Journal of Computational Electronics*, *15*(4), 1521-1530.

[57] Zhang, D. N., Zhao, L., Wang, J. F., & Li, Y. L. (2015). Electronic structures and the stability of MgO surface: density functional study. *Surface Review and Letters*, *22*(03), 1550037.

[58] Rajab, M. A., Salman, S. A., & Abdullah, M. N. (2020). Effect of Nanoparticles and Fibers Types on Hybrid Blend Composite Materials Behavior of Epoxy and Phenol-Formaldehyde. *International Journal of Nanoelectronics & Materials*, *13*(1).

[59] Kaveh, R., & Alijani, H. (2021). An overview: recent development of semiconductor/graphene nanocomposites for photodegradation of phenol and phenolic compounds in aqueous solution. *Journal of Asian Ceramic Societies*, *9*(1), 1-23.

[60] Zhang, F., Wang, X., Liu, H., Liu, C., Wan, Y., Long, Y., & Cai, Z. (2019). Recent advances and applications of semiconductor photocatalytic technology. *Applied Sciences*, *9*(12), 2489.

[61] Mishra, S., & Acharya, R. (2021). Photocatalytic applications of graphene based semiconductor composites: A review. *Materials Today: Proceedings*, *35*, 164-169.

[62] Padmanabhan, N. T., Thomas, N., Louis, J., Mathew, D. T., Ganguly, P., John, H., & Pillai, S. C. (2021). Graphene coupled TiO2 photocatalysts for environmental applications: A review. *Chemosphere*, 129506.

[63] Putri, L. K., Ong, W. J., Chang, W. S., & Chai, S. P. (2015). Heteroatom doped graphene in photocatalysis: a review. *Applied surface science*, *358*, 2-14.

[64] Kumar, P., Boukherroub, R., & Shankar, K. (2018). Sunlight-driven water-splitting using two-dimensional carbon based semiconductors. *Journal of Materials Chemistry A*, *6*(27), 12876-12931.

[65] Yutomo, E. B., Noor, F. A., & Winata, T. (2021). Effect of the number of nitrogen dopants on the electronic and magnetic properties of graphitic and pyridinic N-doped graphene–a density-functional study. *RSC Advances*, *11*(30), 18371-18380.

[66] Dan, M., Vulcu, A., Porav, S. A., Leostean, C., Borodi, G., Cadar, O., & Berghian-Grosan, C. (2021). Eco-friendly nitrogen-doped graphene preparation and design for the oxygen reduction reaction. *Molecules*, *26*(13), 3858.

[67] Bie, C., Yu, H., Cheng, B., Ho, W., Fan, J., & Yu, J. (2021). Design, fabrication, and mechanism of nitrogen-doped graphene-based photocatalyst. *Advanced Materials*, *33*(9), 2003521.

[68] Liu, M., Wen, Y., Lu, L., Chen, Y., Tian, X., Jin, H., ... & Dai, K. (2021). Nitrogen-doped graphene/graphitic carbon nitride with enhanced charge separation and two-electron-transferring reaction activity for boosting photocatalytic hydrogen peroxide production. *Sustainable Energy & Fuels*, *5*(5), 1511-1520.

[69] Wang, H., Maiyalagan, T., & Wang, X. (2012). Review on recent progress in nitrogen-doped graphene: synthesis, characterization, and its potential applications. *ACS catalysis*, *2*(5), 781-794.

[70] Mazzier, D., Favaro, M., Agnoli, S., Silvestrini, S., Granozzi, G., Maggini, M., & Moretto, A. (2014). Synthesis of luminescent 3D microstructures formed by carbon quantum dots and their self-assembly properties. *Chemical Communications*, *50*(50), 6592-6595.

[71] Raja, I. S., Song, S. J., Kang, M. S., Lee, Y. B., Kim, B., Hong, S. W., ... & Han, D. W. (2019). Toxicity of zero-and one-dimensional carbon nanomaterials. *Nanomaterials*, *9*(9), 1214.

[72] Nekoueian, K., Amiri, M., Sillanpää, M., Marken, F., Boukherroub, R., & Szunerits, S. (2019). Carbon-based quantum particles: an electroanalytical and biomedical perspective. *Chemical Society Reviews*, *48*(15), 4281-4316.

[73] Motahari, F., Mozdianfard, M. R., Soofivand, F., & Salavati-Niasari, M. (2014). NiO nanostructures: synthesis, characterization and photocatalyst application in dye wastewater treatment. *Rsc Advances*, *4*(53), 27654-27660.

[74] Haider, A. J., Al-Anbari, R., Sami, H. M., & Haider, M. J. (2019). Photocatalytic activity of nickel oxide. *Journal of Materials Research and Technology*, *8*(3), 2802-2808.

[75] Khairnar, S. D., & Shrivastava, V. S. (2019). Facile synthesis of nickel oxide nanoparticles for the degradation of Methylene blue and Rhodamine B dye: a comparative study. *Journal of Taibah University for Science*, *13*(1), 1108-1118.

[76] Maniammal, K., Madhu, G., & Biju, V. (2018). Nanostructured mesoporous NiO as an efficient photocatalyst for degradation of methylene blue: structure, properties and performance. *Nano-Structures & Nano-Objects*, *16*, 266-275.

[77] Chaudhary, S., Kaur, Y., Jayee, B., Chaudhary, G. R., & Umar, A. (2018). NiO nanodisks: Highly efficient visible-light driven photocatalyst, potential scaffold for seed germination of Vigna Radiata and antibacterial properties. *Journal of Cleaner Production, 190*, 563-576..

[78] Thampy, U. U., Mahesh, A., Sibi, K. S., Jawahar, I. N., & Biju, V. (2019). Enhanced photocatalytic activity of ZnO–NiO nanocomposites synthesized through a facile sonochemical route. *SN Applied Sciences*, *1*(11), 1-15.

[79] Chen, C. J., Liao, C. H., Hsu, K. C., Wu, Y. T., & Wu, J. C. (2011). P–N junction mechanism on improved NiO/TiO2 photocatalyst. *Catalysis communications*, *12*(14), 1307-1310.

[80].Vidya, J., & Balamurugan, P. (2019). Photocatalytic degradation of methylene blue using PANi—NiO nanocomposite under visible light irradiation. *Materials Research Express*, *6*(9), 0950c8.

[81] Faisal, M., Harraz, F. A., Ismail, A. A., El-Toni, A. M., Al-Sayari, S. A., Al-Hajry, A., & Al-Assiri, M. S. (2018). Novel mesoporous NiO/TiO2 nanocomposites with enhanced photocatalytic activity under visible light illumination. *Ceramics International*, *44*(6), 7047-7056.

[82] Santos, R. K., Martins, T. A., Silva, G. N., Conceição, M. V., Nogueira, I. C., Longo, E., & Botelho, G. (2020). Ag3PO4/NiO composites with enhanced photocatalytic activity under visible light. *ACS omega*, *5*(34), 21651-21661.

[83] Ding, M., Yang, H., Yan, T., Wang, C., Deng, X., Zhang, S., ... & Xu, X. (2018). Fabrication of hierarchical ZnO@ NiO core–shell heterostructures for improved photocatalytic performance. *Nanoscale research letters*, *13*(1), 1-9.

[84] Chen, J. Z., Chen, T. H., Lai, L. W., Li, P. Y., Liu, H. W., Hong, Y. Y., & Liu, D. S. (2015). Preparation and characterization of surface photocatalytic activity with NiO/TiO2 nanocomposite structure. *Materials*, *8*(7), 4273-4286.

[85].Soofivand, F., & Salavati-Niasari, M. (2017). Step synthesis and photocatalytic activity of NiO/graphene nanocomposite under UV and visible light as an effective photocatalyst. *Journal of Photochemistry and Photobiology A:.Chemistry*, *337*, 44-53.

[86] Rahimi, K., Zafarkish, H., & Yazdani, A. (2018). Reduced graphene oxide can activate the sunlight-induced photocatalytic effect of NiO nanowires. *Materials & Design*, *144*, 214-221.

[87] Sadhukhan, S., Bhattacharyya, A., Rana, D., Ghosh, T. K., Orasugh, J. T., Khatua, S., ... & Chattopadhyay, D. (2020). Synthesis of RGO/NiO nanocomposites adopting a green approach and its photocatalytic and antibacterial properties. *Materials Chemistry and Physics*, *247*, 122906.

[88] Al-Nafiey, A., Kumar, A., Kumar, M., Addad, A., Sieber, B., Szunerits, S., ... & Jain, S. L. (2017). Nickel oxide nanoparticles grafted on reduced graphene oxide (rGO/NiO) as efficient photocatalyst for reduction of nitroaromatics under visible light irradiation. *Journal of Photochemistry and Photobiology A: Chemistry*, *336*, 198-207.

[89] Chen, J., Wang, M., Han, J., & Guo, R. (2020). TiO2 nanosheet/NiO nanorod hierarchical nanostructures: p–n heterojunctions towards efficient photocatalysis. *Journal of colloid and interface science*, *562*, 313-321.

[90].Alaei, M., Mahjoub, A. R., & Rashidi, A. (2012). Effect of WO3 nanoparticles on Congo red and rhodamine B photo degradation.

[91] Desseigne, M., Dirany, N., Chevallier, V., & Arab, M. (2019). Shape dependence of photosensitive properties of WO3 oxide for photocatalysis under solar light irradiation. *Applied Surface Science*, *483*, 313-323.

[92] Sayama, K., Hayashi, H., Arai, T., Yanagida, M., Gunji, T., & Sugihara, H. (2010). Highly active WO3 semiconductor photocatalyst prepared from amorphous peroxo-tungstic acid for the degradation of various organic compounds. *Applied Catalysis B: Environmental*, *94*(1-2), 150-157.

[93] Ashkarran, A. A., Ahadian, M. M., & Ardakani, S. M. (2008). Synthesis and photocatalytic activity of WO3 nanoparticles prepared by the arc discharge method in deionized water. *Nanotechnology*, *19*(19), 195709.

[94] Zhang, G., Guan, W., Shen, H., Zhang, X., Fan, W., Lu, C., ... & Shi, W. (2014). Organic additives-free hydrothermal synthesis and visible-light-driven photodegradation of tetracycline of WO3 nanosheets. *Industrial & Engineering Chemistry Research*, *53*(13), 5443-5450.

[95] Wang, L., Hu, H., Xu, J., Zhu, S., Ding, A., & Deng, C. (2019). WO3 nanocubes: Hydrothermal synthesis, growth mechanism, and photocatalytic performance. *Journal of Materials Research*, *34*(17), 2955-2963.

[96] Abazari, R., Mahjoub, A. R., Saghatforoush, L. A., & Sanati, S. (2014). Characterization and optical properties of spherical WO3 nanoparticles synthesized via the reverse microemulsion process and their photocatalytic behavior. *Materials letters*, *133*, 208-211.

[97] Liu, Z., Zhao, Z. G., & Miyauchi, M. (2009). Efficient visible light active CaFe2O4/WO3 based composite photocatalysts: effect of interfacial modification. *The Journal of Physical Chemistry C*, *113*(39), 17132-17137.

[98] Adhikari, S. P., Dean, H., Hood, Z. D., Peng, R., More, K. L., Ivanov, I., ... & Lachgar, A. (2015). Visible-light-driven Bi2O3/WO3 composites with enhanced photocatalytic activity. *RSC advances*, *5*(111), 91094-91102.

[99] Tahir, M. B., Farman, S., Rasheed, A., Alrobei, H., Shahzad, K., Ali, A. M., & Muhammad, S. (2021). Insight role of TiO2 to improve the photocatalytic performance of WO3 nanostructures for the efficient degradation of ciprofloxacin. *Zeitschrift für Physikalische Chemie*.

[100] Priya, A., Arunachalam, P., Selvi, A., Madhavan, J., & Al-Mayouf, A. M. (2018). Synthesis of BiFeWO6/WO3 nanocomposite and its enhanced photocatalytic activity towards degradation of dye under irradiation of light. *Colloids and Surfaces A: Physicochemical and Engineering Aspects*, *559*, 83-91.

[101] Chai, B., Liu, C., Yan, J., Ren, Z., & Wang, Z. J. (2018). In-situ synthesis of WO3 nanoplates anchored on g-C3N4 Z-scheme photocatalysts for significantly enhanced photocatalytic activity. *Applied Surface Science*, *448*, 1-8.

[102] Wang, S. L., Zhu, Y., Luo, X.; Huang, Y., Chai, J., Wong, T. I., & Xu, G. Q. (2018). 2D WC/WO3 heterogeneous hybrid for photocatalytic decomposition of organic compounds with Vis–NIR light. *Advanced Functional Materials*, *28*(11), 1705357.

[103] Leghari, S. A. K., Sajjad, S., & Zhang, J. (2013). Large mesoporous micro-spheres of WO 3/TiO 2 composite with enhanced visible light photo activity. *RSC advances*, *3*(35), 15354-15361.

[104] Sajjad, A. K. L., Sajjad, S., & Iqbal, A. (2018). ZnO/WO3 nanostructure as an efficient visible light catalyst. *Ceramics International*, *44*(8), 9364-9371.

[105] Ramesh, K., Gnanavel, B., & Shkir, M. (2021). Enhanced visible light photocatalytic degradation of bisphenol A (BPA) by reduced graphene oxide (RGO)–metal oxide (TiO2, ZnO and WO3) based nanocomposites. *Diamond and Related Materials, 118*, 108514.

[106] Tran, V. A., Nguyen, T. P., Kim, I. T., Lee, S. W., & Nguyen, C. T. (2021). Excellent photocatalytic activity of ternary Ag@ WO3@ rGO nanocomposites under solar simulation irradiation. *Journal of Science: Advanced Materials and Devices*, *6*(1), 108-117.

[107] Shi, R., Z. Zhang, and F. Luo, N-doped graphene-based CuO/WO3/Cu composite material with performances of catalytic decomposition 4-nitrophenol and photocatalytic degradation of organic dyes. Inorganic Chemistry Communications, 2020. 121: p. 108246.

[108] Chaudhary, K., Shaheen, N., Zulfiqar, S., Sarwar, M. I., Suleman, M., Agboola, P. O.,

... & Warsi, M. F. (2020). Binary WO3-ZnO nanostructures supported rGO ternary nanocomposite for visible light driven photocatalytic degradation of methylene blue. Synthetic Metals, 269, 116526

[109] Neena, D., Kondamareddy, K.˙K., Humayun, M., Mohan, V. B., Lu, D., Fu, D., &

Gao, W. (2019). Fabrication of ZnO/N-rGO composite as highly efficient visible-light photocatalyst for 2, 4-DCP degradation and H2 evolution. Applied Surface Science, 488, 611-619.

[110] Khan, M. Y., Ahmad, M., Sadaf, S., Iqbal, S., Nawaz, F., & Iqbal, J. (2019). Visible light active indigo dye/graphene/WO3 nanocomposites with excellent photocatalytic activity. *Journal of Materials Research and Technology*, *8*(3), 3261-3269.

[111] Hu, X., Xu, P., Gong, H., & Yin, G. (2018). Synthesis and characterization of WO3/Graphene nanocomposites for enhanced photocatalytic activities by one-step in-situ hydrothermal reaction. *Materials*, *11*(1), 147.

[112] Nugraha, M. W., Abidin, N. H. Z., & Sambudi, N. S. (2021). Synthesis of tungsten oxide/amino-functionalized sugarcane bagasse derived-carbon quantum dots (WO3/N-CQDs) composites for methylene blue removal. *Chemosphere*, *277*, 130300.

[113] Li, G., Hou, J., Zhang, W., Li, P., Liu, G., Wang, Y., & Wang, K. (2020). Graphene-bridged WO3/MoS2 Z-scheme photocatalyst for enhanced photodegradation under visible light irradiation. *Materials Chemistry and Physics*, *246*, 122827.

[114] Zhi, L., Zhang, S., Xu, Y., Tu, J., Li, M., Hu, D., & Liu, J. (2020). Controlled growth of AgI nanoparticles on hollow WO3 hierarchical structures to act as Z-scheme photocatalyst for visible-light photocatalysis. *Journal of Colloid and Interface Science*, *579*, 754-765.

[115]. Zheng, Y., Cao, L., Xing, G., Bai, Z., Huang, J., & Zhang, Z. (2019). Microscale flower-like magnesium oxide for highly efficient photocatalytic degradation of organic dyes in aqueous solution. *RSC Advances*, *9*(13), 7338-7348.

[116]. Mageshwari, K., & Sathyamoorthy, R. (2012). Studies on photocatalytic performance of MgO nanoparticles prepared by wet chemical method. *Transactions of the Indian Institute of Metals*, *65*(1), 49-55.

[117] Taourati, R., Khaddor, M., Laghzal, A., & El Kasmi, A. (2020). Facile one-step synthesis of highly efficient single oxide nanoparticles for photocatalytic application. *Scientific African*, *8*, e00305.

[118] Khan, M. I., Akhtar, M. N., Ashraf, N., Najeeb, J., Munir, H., Awan, T. I., ... & Kabli, M. R. (2020). Green synthesis of magnesium oxide nanoparticles using Dalbergia sissoo extract for photocatalytic activity and antibacterial efficacy. *APPLIED NANOSCIENCE.*

[119] Bandara, J., Hadapangoda, C. C., & Jayasekera, W. G. (2004). TiO2/MgO composite photocatalyst: the role of MgO in photoinduced charge carrier separation. *Applied Catalysis B: Environmental*, *50*(2), 83-88.

[120] Nga, N. K., Chau, N. T. T., & Viet, P. H. (2020). Preparation and characterization of a chitosan/MgO composite for the effective removal of reactive blue 19 dye from aqueous solution. *Journal of Science: Advanced Materials and Devices*, *5*(1), 65-72.

[121] Baig, N., Kammakakam, I., & Falath, W. (2021). Nanomaterials: a review of synthesis methods, properties, recent progress, and challenges. *Materials Advances*, *2*(6), 1821-1871.

[122] Tatarchuk, T., Peter, A., Al-Najar, B., Vijaya, J., & Bououdina, M. (2018). Photocatalysis: activity of nanomaterials. *Nanotechnology in environmental science*, 209-292.

[123] Gan, Y. X., Jayatissa, A. H., Yu, Z., Chen, X., & Li, M. (2020). Hydrothermal synthesis of nanomaterials. *Journal of Nanomaterials, 2020.*

[124] Li, J., Wu, Q., & Wu, J. (2016). Synthesis of Nanoparticles via Solvothermal and Hydrothermal Methods 12.

[125] Mourdikoudis, S., Pallares, R. M., & Thanh, N. T. (2018). Characterization techniques for nanoparticles: comparison and complementarity upon studying nanoparticle properties. *Nanoscale*, *10*(27), 12871-12934.

[126] Abraham, J., Jose, B., Jose, A., & Thomas, S. (2020). Characterization of green nanoparticles from plants. In *Phytonanotechnology* (pp. 21-39). Elsevier.

[127] Sharma, R., Bisen, D. P., Shukla, U., & Sharma, B. G. (2012). X-ray diffraction: a powerful method of characterizing nanomaterials. *Recent research in science and technology, 4*(8).

[128] Campbell, J., Burkitt, S., Dong, N., & Zavaleta, C. (2020). Nanoparticle characterization techniques. In *Nanoparticles for Biomedical Applications* (pp. 129-144). Elsevier.

[129] Akhtar, K., Khan, S. A., Khan, S. B., & Asiri, A. M. (2018). Scanning electron microscopy: Principle and applications in nanomaterials characterization. In *Handbook of materials characterization* (pp. 113-145). Springer, Cham.

[130] Nanakoudis, A. (2018). EDX analysis with a scanning electron microscope (SEM): how does it work. *ThermoFisher Scientific.*

[131] Asadi Asadabad, M., & Jafari Eskandari, M. (2015). Transmission electron microscopy as best technique for characterization in nanotechnology. *Synthesis and Reactivity in Inorganic, Metal-Organic, and Nano-Metal Chemistry, 45*(3), 323-326.

.[132] Chakravadhanula, V., & Sai, K. (2011). *Vapor phase deposition of functional nanocomposite thin films and their modification by ion beam irradiation* (Doctoral dissertation).

[133] Ismail, A. A., van de Voort, F. R., & Sedman, J. (1997). Fourier transform infrared spectroscopy: principles and applications. In *Techniques and instrumentation in analytical chemistry* (Vol. 18, pp. 93-139). Elsevier

[134] Nicolson, F., Kircher, M. F., Stone, N., & Matousek, P. (2021). Spatially offset Raman spectroscopy for biomedical applications. *Chemical Society Reviews, 50*(1), 556-568.

[135] Mosca, S., Conti, C., Stone, N., & Matousek, P. (2021). Spatially offset Raman spectroscopy. *Nature Reviews Methods Primers, 1*(1), 1-16.

[136] Vallikkodi, M. (2018). Synthesis, growth and characterization of piperazinium P-aminobenzoate and piperazinium P-chlorobenzoate nonlinear optical single crystals. *Alagappa University, Karaikudi, India.*

[137] CLARK, J. (2019). What causes molecules to absorb UV and visible light?

[138] Azevedo, A. F., Baldan, M. R., & Ferreira, N. G. (2012). Nanodiamond films for applications in electrochemical systems. *International Journal of Electrochemistry, 2012.*

[139] Bhatia, S., & Verma, N. (2017). Photocatalytic activity of ZnO nanoparticles with optimization of defects. *Materials Research Bulletin, 95*, 468-476.

[140] V. Kumar, K.H. Kim, J.W. Park, J. Hong, S. Kumar, Graphene and its nanocomposites as a platform for environmental applications, *Chemical Engineering Journal*, 315 (2017) 210-232.

[141] Deblonde, T., Cossu-Leguille, C., & Hartemann, P. (2011). Emerging pollutants in wastewater: a review of the literature. *International Journal of Hygiene and Environmental Health, 214*(6), 442-448.

[142] Gupta, K., & Khatri, O. P. (2017). Reduced graphene oxide as an effective adsorbent for removal of malachite green dye: plausible adsorption pathways. *Journal of Colloid and Interface Science, 501*, 11-21.

[143] Doufar, N., Benamira, M., Lahmar, H., Trari, M., Avramova, I., & Caldes, M. T. (2020). Structural and photochemical properties of Fe-doped ZrO2 and their application as photocatalysts

with TiO2 for chromate reduction. *Journal of Photochemistry and Photobiology A: Chemistry, 386*, 112105.

[144] Sajjad, S., Bano, T., Leghari, S. A. K., (2017). Efficient visible light magnetic modified iron oxide photocatalysts, *Ceramics International*, 43 (17), 14672-14677.

[145] Douafer, S., Lahmar, H., Benamira, M., Messaadia, L., Mazouzi, D., & Trari, M. (2019). Chromate reduction on the novel hetero-system LiMn2O4/SnO2 catalyst under solar light irradiation. *Surfaces and Interfaces*, *17*, 100372.

[146] Song, H., Yang, Y., Li, Z., Huang, M., Yu, J., & Wu, Y. (2019). Atomically thin two-dimensional ZnSe/ZnSe (ea) x van der Waals nanojunctions for synergistically enhanced visible light photocatalytic H_2 evolution. *Nanoscale*, *11*(38), 17718-17724.

[147] Shu, Y., Li, B., Chen, J., Xu, Q., Pang, H., & Hu, X. (2018). Facile synthesis of ultrathin nickel–cobalt phosphate 2D nanosheets with enhanced electrocatalytic activity for glucose oxidation. *ACS Applied Materials & Interfaces*, *10*(3), 2360-2367.

[148] Abdul Rahman, I., Ayob, M. T. M., & Radiman, S. (2014). Enhanced photocatalytic performance of NiO-decorated ZnO nano-whiskers for methylene blue degradation. *Journal of Nanotechnology*, *2014*.

[149] Zhang, F., Liu, Y. J., Liu, Q. H., Li, Q., Li, H., Cai, X. Y., & Wang, Y. D. (2013). Synthesis and characterization of Ni $(OH)_2$ and NiO nanosheets and their removal properties of azo dyes from aqueous solution. *Materials Technology*, *28*(6), 310-315.

[150] Nallendran, R., Selvan, G., & Balu, A. R. (2018). Photoconductive and photocatalytic properties of CdO–NiO nanocomposite synthesized by a cost effective chemical method. *Journal of Materials Science: Materials in Electronics*, *29*(13), 11384-11393.

[151] Yuan, L., Yang, M. Q., & Xu, Y. J. (2014). Tuning the surface charge of graphene for self-assembly synthesis of a $SnNb_2O_6$ nanosheet–graphene (2D–2D) nanocomposite with enhanced visible light photoactivity. *Nanoscale*, *6*(12), 6335-6345.

[152] Sun, J., Zhang, H., Guo, L. H., & Zhao, L. (2013). Two-dimensional interface engineering of a titania–graphene nanosheet composite for improved photocatalytic activity. *ACS Applied Materials & Interfaces*, *5*(24), 13035-13041.

[153] Xiao, F. X., Miao, J., & Liu, B. (2014). Layer-by-layer self-assembly of CdS quantum dots/graphene nanosheets hybrid films for photoelectrochemical and photocatalytic applications. *Journal of the American Chemical Society*, *136*(4), 1559-1569.

[154] Hou, Y., Wen, Z., Cui, S., Guo, X., & Chen, J. (2013). Constructing 2D porous graphitic C_3N_4 nanosheets/nitrogen-doped graphene/layered MoS2 ternary nanojunction with enhanced photoelectrochemical activity. *Advanced Materials*, *25*(43), 6291-6297.

[155] Sun, J., Wang, C., Shen, T., Song, H., Li, D., Zhao, R., & Wang, X. (2019). Engineering the dimensional interface of $BiVO_4$-2D reduced graphene oxide (RGO) nanocomposite for enhanced visible light photocatalytic performance. *Nanomaterials*, *9*(6), 907.

[156] Sun, Y., Li, G., Xu, J., Lei, B., Feng, H., & Sun, Z. (2019). Impacts of graphene sheets on photoelectric and photo catalytic activities of SnS_2 nanoparticles. *Materials Chemistry and Physics*, *229*, 92-97.

[157] Liang, Z. H., Zhu, Y. J., & Hu, X. L. (2004). β-nickel hydroxide nanosheets and their thermal decomposition to nickel oxide nanosheets. *The Journal of Physical Chemistry B*, *108*(11), 3488-3491.

[158] Ramesh, T. N., & Kamath, P. V. (2006). Synthesis of nickel hydroxide: effect of precipitation conditions on phase selectivity and structural disorder. *Journal of power sources*, *156*(2), 655-661.

[159] Abubakar, D., Ahmed, N. M., Mahmud, S., & Al-Hazeem, N. Z. (2017). Optimum Annealing Temperature for Transformation of NiO Nanoflakes from Chemically Grown Ni (OH)2 Nanostructure Thin Film. In *Journal of Nano Research* (Vol. 49, pp. 75-84). Trans Tech Publications Ltd.

[160] Thangavel, S., Elayaperumal, M., & Venugopal, G. (2012). Synthesis and properties of tungsten oxide and reduced graphene oxide nanocomposites. *Materials Express*, *2*(4), 327-334.

[161] Kottegoda, I. R., Idris, N. H., Lu, L., Wang, J. Z., & Liu, H. K. (2011). Synthesis and characterization of graphene–nickel oxide nanostructures for fast charge–discharge application. *Electrochimica Acta*, *56*(16), 5815-5822.

[162] Zhu, X., Dai, H., Hu, J., Ding, L., & Jiang, L. (2012). Reduced graphene oxide–nickel oxide composite as high performance electrode materials for super capacitors. *Journal of Power Sources*, *203*, 243-249.

[163] Xie, D., Su, Q., Yuan, W., Dong, Z., Zhang, J., & Du, G. (2013). Synthesis of porous NiO-wrapped graphene nanosheets and their improved lithium storage properties. *The Journal of Physical Chemistry C*, *117*(46), 24121-24128.

[164] Saima, N., Sajjad, S., Sajjad, A.K.L., Sania, S., Iqbal, A., (2018). ZnO/TiO_2 nanocomposite photoanode as an effective UV-vis responsive dye sensitized solar cell. *Material Research Express* 5(9).

[165] Y., Chu, W., Wang, N., Lin, T., Yang, W., Wen, J., & Zhao, X. S. (2015). Self-assembled Ni/NiO/RGO hetero-structures for high-performance super capacitors. *RSC Advances*, *5*(95), 77958-77964.

[166] Marcano, D. C., Kosynkin, D. V., Berlin, J. M., Sinitskii, A., Sun, Z., Slesarev, A. & Tour, J. M. (2010). Improved synthesis of graphene oxide. *ACS Nano*, *4*(8), 4806-4814.

[167] Sajjad, A.K.L., Shamaila, S., Iqbal, A., (2017) Study of graphene oxide structural features for catalytic, antibacterial, gas sensing, and metals decontamination environmental applications, *ACS Applied Materials & Interfaces*, 9 (50), 43393-43414.

[168] Raja, V., Puvaneswaran, S. K., & Swaminathan, K. (2017). Unique and hierarchically structured novel Co 3 O 4/NiO nanosponges with superior photocatalytic activity against organic contaminants. *Frontiers of Materials Science*, *11*(4), 375-384.

[169] Gao, H., Tayebee, R., Abdizadeh, M. F., Mansouri, E., Latifnia, M., & Pourmojahed, Z. (2020). The efficient biogeneration of Ag and NiO nanoparticles from VPLE and a study of the anti-diabetic properties of the extract. *RSC Advances*, *10*(5), 3005-3012.

[170] Ji, Z., Wu, J., Shen, X., Zhou, H., & Xi, H. (2011). Preparation and characterization of graphene/NiO nanocomposite. *Journal of Materials Science*, *46*(5), 1190-1195.

[171] Ma, L., Pei, X. Y., Mo, D. C., Heng, Y., Lyu, S. S., & Fu, Y. X. (2019). Facile fabrication of NiO flakes and reduced graphene oxide (NiO/R-GO) composite as anode material for lithium-ion batteries. *Journal of Materials Science: Materials in Electronics*, *30*(6), 5874-5880.

[172] Ahmed, S., Rafat, M., & Hashmi, S. A. (2017). Effect of electrolyte concentration on super capacitor performance of graphene-NiO composite. *Int. J. Adv. Res. Sci. Eng*, *6*, 609-14.

[173] Li, X., Yu, J., Low, J., Fang, Y., Xiao, J., & Chen, X. (2015). Engineering heterogeneous semiconductors for solar water splitting. *Journal of Materials Chemistry A*, *3*(6), 2485-2534.

[174] Li, X., Xia, T., Xu, C., Murowchick, J., & Chen, X. (2014). Synthesis and photo activity of nanostructured CdS–TiO_2 composite catalysts. *Catalysis Today*, *225*, 64-73.

[175] Hongbin., Y, Guan H- G., Chunxian G., Qunliang S., San Ping J., Yi., W., Wei Z.,& Chang M- Li (2011). Graphene/NiO composite for enhanced charge separation and collection in p-type dye sensitized solar cell. *J. Phys. Chem. C*, *115*(24), 12209-12215.

[176] Senobari, S., & Nezamzadeh-Ejhieh, A. (2020). A novel ternary nano-composite with a high photocatalyitic activity: Characterization, effect of calcination temperature and designing the experiments. *Journal of Photochemistry and Photobiology A: Chemistry*, *394*, 112455.

[177] Thampy, U. U., Mahesh, A., Sibi, K. S., Jawahar, I. N., & Biju, V. (2019). Enhanced photocatalytic activity of ZnO–NiO nanocomposites synthesized through a facile sonochemical route. *SN Applied Sciences*, *1*(11), 1478.

[178] Gao, E., Wang, W., Shang, M., & Xu, J. (2011). Synthesis and enhanced photocatalytic performance of graphene-Bi_2WO_6 composite. *Physical Chemistry Chemical Physics*, *13*(7), 2887-2893.

[179] Qiu, Z., He, D., Wang, Y., Zhao, X., Zhao, W., & Wu, H. (2017). High performance asymmetric supercapacitors with ultrahigh energy density based on hierarchical carbon nanotubes@ NiO core–shell nanosheets and defect-introduced graphene sheets with hole structure. *RSC Advances*, 7(13), 7843-7856.

[180] Prabhu, S., Cindrella, L., Kwon, O. J., & Mohanraju, K. (2017). Green synthesis of rGO-WO3 composite and its efficient photoelectrochemical water splitting. *International Journal of Hydrogen Energy*, *42*(50), 29791-29796.

[181] Jamila, G. S., Shamaila, S., Sajjad, A.K.L., Long, M., (2020) Nitrogen doped carbon quantum dots and GO modified WO_3 nanosheets combination as an effective visible photo catalyst, *Journal of Hazardous Materials* 382, 121087.

[182] Tian, H., Wan, C., Xue, X., Hu, X., & Wang, X. (2017). Effective electron transfer pathway of the ternary TiO_2/RGO/Ag nanocomposite with enhanced photocatalytic activity under visible light. *Catalysts*, *7*(5), 156.

[183] Liu, S., Zhang, N., Tang, Z. R., & Xu, Y. J. (2012). Synthesis of one-dimensional CdS@ TiO_2 core–shell nanocomposites photocatalyst for selective redox: the dual role of TiO2 shell. *ACS applied materials & interfaces*, *4*(11), 6378-6385.

[184] Arcibar-Orozco, J. A., Zili-Tomita. H. E., Suárez-Toriello, V. A., & Saucedo-Lucero, J. O. (2022). Petcoke Revalorization as Support for ZnO-based Photocatalyst. *Waste and Biomass Valorization*, *13*(3), 1681-1694.

[185] S., Shamaila, S., Sajjad, A.K.L., Shaheen, S., Iqbal, A., Noor, S., Sughra, G., Ali, U., (2017) A cost effective and eco-friendly green route for fabrication of efficient graphene nanosheets photocatalyst, *Journal of Environmental Chemical Engineering* 5 (6), 5770-5776

[186] Lahmar, H., Benamira, M., Douafer, S., Messaadia, L., Boudjerda, A., & Trari, M. (2020). Photocatalytic degradation of methyl orange on the novel hetero-system La2NiO4/ZnO under solar light. *Chemical Physics Letters*, *742*, 137132.

[187] Wu, Y., et al., Ternary mesoporous WO_3/Mn_3O_4/N-doped graphene nanocomposite for enhanced photocatalysis under visible light irradiation. Catalysis Science & Technology, 2015. 5(6): p. 3375-3382.

[188] Xue, Q., et al., Photocatalytic degradation of geosmin by Pd nanoparticle modified WO_3 catalyst under simulated solar light. Chemical Engineering Journal, 2016. 283: p. 614-621.

[189] Xie, J., et al., Simple preparation of WO_3–ZnO composites with UV–Vis photocatalytic activity and energy storage ability. Ceramics International, 2014. 40(8): p. 12519-12524.

[190] Tahir, M.B., G. Nabi, and N. Khalid, Enhanced photocatalytic performance of visible-light active graphene-WO_3 nanostructures for hydrogen production. Materials Science in Semiconductor Processing, 2018. 84: p. 36-41.

[191] Rizzo, A., F. Di Benedetto, and D. Valerini, Sputtered WO_3 films for water splitting applications. 2016.

[192] Lai, C.W. and S. Sreekantan, Fabrication of WO_3 nanostructures by anodization method for visible-light driven water splitting and photodegradation of methyl orange. Material Science in

Semiconductor Processing, 2013. 16(2): p. 303-310.

[193] Alalm, M.G., et al., Improved WO3 photocatalytic efficiency using ZrO_2 and Ru for the degradation of carbofuran and ampicillin. Journal of hazardous materials, 2016. 302: p. 225-231.

[194] Theerthagiri, J., et al., Synthesis and characterization of a CuS–WO_3 composite photocatalyst for enhanced visible light photocatalytic activity. RSC Advances, 2015. 5(65): p. 52718-52725.

[195] Shi, J., et al., Controllable synthesis of $WO_3 \cdot nH_2O$ microcrystals with various morphologies by a facile inorganic route and their photocatalytic activities. New Journal of Chemistry, 2013. 37(5): p. 1538-1544.

[196] Sadiq, M.M.J., U.S. Shenoy, and D.K. Bhat, Enhanced photocatalytic performance of N doped RGO-$FeWO_4/Fe_3O_4$ ternary nanocomposite in environmental applications. Materials Today Chemistry, 2017. 4: p. 133-141.

[197] Iqbal, A., Sajjad, S., and Leghari, SAK, Low cost graphene oxide modified alumina nanocomposite as solar light induced photocatalyst, ACS Applied Nano Materials, 2018, 1(9): p. 4612-4621.

[198] Kumar, M.P., et al., On the large capacitance of nitrogen doped graphene derived by a facile route. RSC advances, 2014. 4(73): p. 38689-38697.

[199] Chang, D.W. and J.B. Baek, Nitrogen-Doped Graphene for Photocatalytic Hydrogen Generation. Chemistry–An Asian Journal, 2016. 11(8): p. 1125-1137.

[200] Kong, X.-K., C.-L. Chen, and Q.-W. Chen, Doped graphene for metal-free catalysis. Chemical Society Reviews, 2014. 43(8): p. 2841-2857.

[201] Gu, X., et al., Three-dimensional nitrogen-doped graphene frameworks anchored with bamboo-like tungsten oxide nanorods as high performance anode materials for lithium ion batteries. Journal of Power Sources, 2016. 320: p. 231-238.

[202] Jia, L., et al., Highly durable N-doped graphene/CdS nanocomposites with enhanced photocatalytic hydrogen evolution from water under visible light irradiation. The Journal of Physical Chemistry C, 2011. 115(23): p. 11466-11473.

[203] Amanulla, B., et al., Enhanced photodegradation of industrial dye using Ag_3PO_4@ N doped graphene nanocomposite under visible light irradiation. Solid State Sciences, 2020. 105: p. 106258.

[204] Ahmad, M., et al., Effects of porous carrier size on biofilm development, microbial distribution and nitrogen removal in microaerobic bioreactors. Bioresource technology, 2017 234: p. 360-369.

[205] Van Aken, P., et al., The effect of ozonation on the toxicity and biodegradability of 2, 4 Dichlorophenol-containing wastewater. Chemical Engineering Journal, 2015. 280: p. 728-736.

[206] Ormad, M., J. Ovelleiro, and J. Kiwi, Photocatalytic degradation of concentrated solutions of 2, 4-dichlorophenol using low energy light: identification of intermediates. Applied Catalysis B: Environmental, 2001. 32(3): p. 157-166.

[207] Ahmad, M., et al., Synergic adsorption–biodegradation by an advanced carrier for

enhanced removal of high-strength nitrogen and refractory organics. ACS applied materials & interfaces, 2017. 9(15): p. 13188-13200.

[208] Ahmad, M., et al., Porous eleocharis@ MnPE layered hybrid for synergistic adsorption and catalytic biodegradation of toxic Azo dyes from industrial wastewater. Environmental science & technology, 2019. 53(4): p. 2161-2170.

[209] Benzait, Z., P. Chen, and L. Trabzon, Enhanced synthesis method of graphene oxide. Nanoscale Advances, 2021. 3(1): p. 223-230.

[210] Noor, S., et al., Energy harvesting for electrochemical OER and solar photocatalysis via dual functional GO/TiO_2-NiO nanocomposite. Journal of Cleaner Production, 2020. 277: p. 123280.

[211] Sadiq, M.M.J., U.S. Shenoy, and D.K. Bhat, Novel RGO–$ZnWO_4$–Fe_3O_4 nanocomposite as high performance visible light photocatalyst. RSC advances, 2016. 6(66): p. 61821-61829.

[212] Sedki, M., et al., Phytosynthesis of silver–reduced graphene oxide (Ag–RGO) nanocomposite with an enhanced antibacterial effect using Potamogeton pectinatus extract. RSC advances, 2015. 5(22): p. 17358-17365.

[213] Khan, M.E., M.M. Khan, and M.H. Cho, CdS-graphene nanocomposite for efficient visible-light-driven photocatalytic and photoelectrochemical applications. Journal of colloid and interface science, 2016. 482: p. 221-232.

[214] Putri, L.K., et al., Heteroatom nitrogen-and boron-doping as a facile strategy to improve photocatalytic activity of standalone reduced graphene oxide in hydrogen evolution. ACS applied

materials & interfaces, 2017. 9(5): p. 4558-4569.

[215] Jiang, Y., S. Chowdhury, and R. Balasubramanian, New insights into the role of nitrogen bonding configurations in enhancing the photocatalytic activity of nitrogen-doped graphene aerogels. Journal of colloid and interface science, 2019. 534: p. 574-585.

[216] Sajjad, A.K.L., S. Sajjad, and A. Iqbal, ZnO/WO_3 nanostructure as an efficient visible light catalyst. Ceramics International, 2018. 44(8): p. 9364-9371.

[217] Jamila, G.S., et al., Nitrogen doped carbon quantum dots and GO modified WO_3 nanosheets combination as an effective visible photo catalyst. Journal of hazardous materials, 2020. 382: p. 121087.

[218] Wang, Z.-l., et al., Facile, mild and fast thermal-decomposition reduction of graphene oxide in air and its application in high-performance lithium batteries. Chemical Communications, 2012. 48(7): p. 976-978.

[219] Thangavel, S., M. Elayaperumal, and G. Venugopal, Synthesis and properties of tungsten oxide and reduced graphene oxide nanocomposites. Materials Express, 2012. 2(4): p. 327-334.

[220] Darvishi, M. and J. Seyed-Yazdi, Effect of microwave power on created defects in graphene sheet of synthesized TiO_2/graphene nanocomposite with enhanced photocatalytic performance. Surfaces and Interfaces, 2016. 4: p. 1-8.

[221]. Tan, C., et al., High-performance tin oxide-nitrogen doped graphene aerogel hybrids as anode materials for lithium-ion batteries. Journal of Power Sources, 2014. 270: p. 28-33.

[222] Yadav, R. and C. Dixit, Synthesis, characterization and prospective applications of nitrogen-doped graphene: A short review. Journal of Science: Advanced Materials and Devices, 2017. 2(2): p. 141-149.

[223] Kumar, N.A., et al., Plasma-assisted simultaneous reduction and nitrogen doping of graphene oxide nanosheets. Journal of Materials Chemistry A, 2013. 1(14): p. 4431-4435.

[224] Xu, L., M.-L. Yin, and S.F. Liu, Ag_x@ WO_3 core-shell nanostructure for LSP enhanced chemical sensors. Scientific reports, 2014. 4(1): p. 1-7.

[225] Guo, J., et al., Synthesis of WO_3@Graphene composite for enhanced photocatalytic oxygen evolution from water. Rsc Advances, 2012. 2(4): p. 1356-1363.

[226] Li, D., et al., Synthesis of nitrogen doped graphene from graphene oxide within an ammonia flame for high performance supercapacitors. Rsc Advances, 2014. 4(98): p. 55394-55399.

[227] Sajjad, A.K.L., et al., Comparative studies of operational parameters of degradation of azo dyes in visible light by highly efficient WO_x/TiO_2 photocatalyst. Journal of Hazardous Materials, 2010. 177(1-3): p. 781-791.

[228] Zhang, H., et al., Direct Z-scheme photocatalytic removal of ammonia via the narrow band gap MoS2/N-doped graphene hybrid catalyst upon near-infrared irradiation. Applied Surface Science, 2020. 504: p. 144065.

[229] Noor, S., et al., Visible light efficient and photo stable nanostructure of GO/CuO/m-TiO_2 ternary composite. Materials Research Express, 2020. 6(12): p. 1250d8.

[230] Rani, P. and V. Jindal, Designing band gap of graphene by B and N dopant atoms. Rsc

Advances, 2013. 3(3): p. 802-812.

[231] Zheng, F., M. Guo, and M. Zhang, Hydrothermal preparation and optical properties of orientation controlled WO_3 nanorod arrays on ITO substrates. CrystEngComm, 2013. 15(2): p. 277-284.

[232] Jiang, Z., et al., High performance acetylene sensor with heterostructure based on WO_3 nanolamellae/reduced graphene oxide (rGO) nanosheets operating at low temperature. Nanomaterials, 2018. 8(11): p. 909.

[233] Bhargava, R. and S. Khan, Fabrication of WO_3–reduced graphene oxide (WO_3G) nanocomposite for enhanced optical and electrical properties. Journal of Materials Science: Materials in Electronics, 2020. 31(11): p. 8370-8384.

[234] Leghari, S.A.K., et al., WO_3/TiO_2 composite with morphology change via hydrothermal template-free route as an efficient visible light photocatalyst. Chemical Engineering Journal, 2011. 166(3): p. 906-915.

[235] Li, J., et al., Searching for magnetism in pyrrolic N-doped graphene synthesized via hydrothermal reaction. Carbon, 2015. 84: p. 460-468.

[236] Noor, S., et al., Competitive role of nitrogen functionalities of N doped GO and sensitizing effect of Bi_2O_3 QDs on TiO_2 for water remediation. Journal of Environmental Sciences, 2021. 108: p. 107-119.

[237] Ahmad, M., et al., Role of HRT in biological treatment of combined industrial and municipal Waste water. International Journal of Engineering and Technology, 2013. 3: p. 2277-4106.

[238] Dong, S., et al., Recent developments in heterogeneous photocatalytic water treatment using visible light-responsive photocatalysts: a review. Rsc Advances, 2015. 5(19): p. 14610-14630.

[239] Yan, L., et al., Chemistry and physics of a single atomic layer: strategies and challenges for functionalization of graphene and graphene-based materials. Chemical Society Reviews, 2012. 41(1): p. 97-114.

[240] Li, P., et al., Enhanced photocatalytic property of $BiFeO_3$/N-doped graphene composites and mechanism insight. Applied Surface Science, 2017. 396: p. 879-887.

[241] Liu, C., et al., Visible-light driven photocatalyst of CdTe/CdS homologous heterojunction on N-rGO photocatalyst for efficient degradation of 2, 4-dichlorophenol. Journal of the Taiwan Institute of Chemical Engineers, 2018. 93: p. 603-615.

[242] Liu, J., et al., Preparation and photocatalytic properties of N-doped graphene/TiO_2 composites. Journal of Chemistry, 2020. 2020.

[243] Wan, J., et al., Nitrogen doped graphene oxide modified WSe_2 nanorods for visible light photocatalysis. Journal of Alloys and Compounds, 2018. 750: p. 499-506.

[244] Li, H., et al., *Boosting visible-light photocatalytic degradation of indomethacin by an efficient and photostable Ag3PO4/NG/WO3 composites.* Applied Surface Science, 2019. 490: p. 481-491.

[245] Nugraha, M.W., N.H.Z. Abidin, and N.S. Sambudi, *Synthesis of tungsten oxide/amino-functionalized sugarcane bagasse derived-carbon quantum dots (WO3/N-CQDs) composites for methylene blue removal.* Chemosphere, 2021. 277: p. 130300.

[246] Senobari, S. and A. Nezamzadeh-Ejhieh, A novel ternary nano-composite with a high photocatalyitic activity: Characterization, effect of calcination temperature and designing the experiments. Journal of Photochemistry and Photobiology A: Chemistry, 2020. 394: p. 112455.

[247] Zhu, W., et al., Facile fabrication of RGO-WO_3 composites for effective visible light photocatalytic degradation of sulfamethoxazole. Applied Catalysis B: Environmental, 2017. 207: p. 93-102

[248] Tran, D.T., et al., Enhanced photocatalytic degradation of methyl orange using

ZnO/graphene oxide nanocomposites. Research on Chemical Intermediates, 2018. 44(5): p. 3081

3095.

[249] Algethami, F. K., Katouah, H. A., Al-Omar, M. A., Almehizia, A. A., Amr, A. E. G. E., Naglah, A. M., ... & Youssef, H. M. (2021). Facile Synthesis of Magnesium Oxide Nanoparticles for Studying Their Photocatalytic Activities Against Orange G Dye and Biological Activities Against Some Bacterial and Fungal Strains. *Journal of Inorganic and Organometallic Polymers and Materials*, *31*(5), 2150-2160.

[250] Arikal, D., & Kallingal, A. (2021). Photocatalytic degradation of azo and anthraquinone dye using TiO2/MgO nanocomposite immobilized chitosan hydrogels. *Environmental technology*, *42*(15), 2278-2291.

[251] Zeng, W., Yin, Z., Gao, M., Wang, X., Feng, J., Ren, Y., ... & Fan, Z. (2020). In-situ growth of magnesium peroxide on the edge of magnesium oxide nanosheets: Ultrahigh photocatalytic efficiency based on synergistic catalysis. *Journal of colloid and interface science*, *561*, 257-264.

[252] Ratnam, M. V., Karthikeyan, C., Rao, K. N., & Meena, V. (2020). Magnesium oxide nanoparticles for effective photocatalytic degradation of methyl red dye in aqueous solutions: optimization studies using response surface methodology. *Materials Today: Proceedings*, *26*, 2308-2313.

[253] Hai, C., Zhou, Y., Du, Y., Sun, Y., Zeng, J., Shen, Y., ... & Dong, O. (2017). Synthesis of MgO nanocrystals with abundant surface defects via a carbonization method employing CO2 gas as starting material. *Materials Research Bulletin*, *85*, 181-187.

[254]. Zeng, W., Gao, M., Liu, K., Li, C., Cao, N., Zhao, X., ... & Wei, T. (2021). Boosting charge separation and surface defects for superb photocatalytic activity of magnesium oxide/graphene nanosheets. *Applied Surface Science*, *535*, 147658.

[255] Peng, Q., Dai, Y., Liu, K., Luo, X., He, D., Tang, X., & Huang, G. (2020). A novel carbon nanotube–magnesium oxide composite with excellent recyclability to efficiently activate peroxymonosulfate for Rhodamine B degradation. *Journal of Materials Science*, *55*, 11267-11283.

[256] Tang, B., Chen, H., Peng, H., Wang, Z., & Huang, W. (2018). Graphene modified TiO2 composite photocatalysts: Mechanism, progress and perspective. *Nanomaterials*, *8*(2), 105.

[257] Moradi, S., Sobhgol, S. A., Hayati, F., Isari, A. A., Kakavandi, B., Bashardoust, P., & Anvaripour, B. (2020). Performance and reaction mechanism of MgO/ZnO/Graphene ternary nanocomposite in coupling with LED and ultrasound waves for the degradation of sulfamethoxazole and pharmaceutical wastewater. *Separation and Purification Technology*, *251*, 117373.

[258] Lu, K. Q., Quan, Q., Zhang, N., & Xu, Y. J. (2016). Multifarious roles of carbon quantum dots in heterogeneous photocatalysis. *Journal of energy chemistry*, *25*(6), 927-935.

[259] Tajik, S., Dourandish, Z., Zhang, K., Beitollahi, H., Van Le, Q., Jang, H. W., & Shokouhimehr, M. (2020). Carbon and graphene quantum dots: A review on syntheses, characterization, biological and sensing applications for neurotransmitter determination. *RSC Advances*, *10*(26), 15406-15429.

[260] Gholinejad, M., Bahrami, M., & Nájera, C. (2017). A fluorescence active catalyst support comprising carbon quantum dots and magnesium oxide doping for stabilization of palladium nanoparticles: Application as a recoverable catalyst for Suzuki reaction in water. *Molecular Catalysis*, *433*, 12-19.

[261] Yousaf, Z., Sajjad, S., Leghari, S. A. K., Noor, S., Kanwal, A., Bhatti, S. H., ... & El-Bahy, Z. M. (2021). Influence of integrated nitrogen functionalities in nitrogen doped graphene modified WO3 functional visible photocatalyst. *Journal of Environmental Chemical Engineering*, *9*(6), 106746.

[262] Gunathilake, C. A., Ranathunge, G. G. T. A., Dassanayake, R. S., Illesinghe, S. D., Manchanda, A. S., Kalpage, C. S., ... & Karunaratne, D. G. G. P. (2020). Emerging investigator series: synthesis of magnesium oxide nanoparticles fabricated on a graphene oxide nanocomposite for CO 2 sequestration at elevated temperatures. *Environmental Science: Nano*, *7*(4), 1225-1239.

[263] Keyang, H., Ruiyi, L., Zaijun, L., & Yongqiang, Y. (2020). Controllable synthesis of superparamagnetic NiCo-graphene quantum dot-graphene composite with excellent dispersion for high performance magnetic field-controlled electrochemical flow hybrid supercapacitor. *Electrochimica Acta*, *353*, 136524.

[264] Zhao, M., Zhang, J., Xiao, H., Hu, T., Jia, J., & Wu, H. (2019). Facile in situ synthesis of a carbon quantum dot/graphene heterostructure as an efficient metal-free electrocatalyst for overall water splitting. *Chemical Communications*, *55*(11), 1635-1638.

[265] Ahmad, M., Ahmed, E., Hong, Z. L., Xu, J. F., Khalid, N. R., Elhissi, A., & Ahmed, W. (2013). A facile one-step approach to synthesizing ZnO/graphene composites for enhanced degradation of methylene blue under visible light. *Applied Surface Science*, *274*, 273-281.

[266] Cao, J., Hu, Y., Chen, L., Xu, J., & Chen, Z. (2017). Nitrogen-doped carbon quantum dot/graphene hybrid nanocomposite as an efficient catalyst support for the oxygen reduction reaction. *International Journal of Hydrogen Energy*, *42*(5), 2931-2942.

[267] Peng, Q., Dai, Y., Liu, K., Luo, X., He, D., Tang, X., & Huang, G. (2020). A novel carbon nanotube–magnesium oxide composite with excellent recyclability to efficiently activate peroxymonosulfate for Rhodamine B degradation. *Journal of Materials Science*, *55*, 11267-11283

[268]. Selvam, N. C. S., Kumar, R. T., Kennedy, L. J., & Vijaya, J. J. (2011). Comparative study of microwave and conventional methods for the preparation and optical properties of novel MgO-micro and nano-structures. *Journal of Alloys and Compounds*, *509*(41), 9809-9815.

[269] Mageshwari, K., Mali, S. S., Sathyamoorthy, R., & Patil, P. S. (2013). Template-free synthesis of MgO nanoparticles for effective photocatalytic applications. *Powder technology*, *249*, 456-462.

[270] Nga, N. K., Chau, N. T. T., & Viet, P. H. (2020). Preparation and characterization of a chitosan/MgO composite for the effective removal of reactive blue 19 dye from aqueous solution. *Journal of Science: Advanced Materials and Devices*, *5*(1), 65-72.

[271] Ashok, C. H., Rao, K. V., Chakra, C. S., & Rao, K. G. (2016). MgO nanoparticles prepared by microwave-irradiation technique and its seed germination application. *Nano Trends: A Journal of Nanotechnology*, *18*(1), 10-17.

[272] Kumar, A., Kumari, A., Sharma, G., Du, B., Naushad, M., & Stadler, F. J. (2020). Carbon quantum dots and reduced graphene oxide modified self-assembled S@ C3N4/B@ C3N4 metal-free nano-photocatalyst for high performance degradation of chloramphenicol. *Journal of Molecular Liquids*, *300*, 112356.

[273] Ma, X., Li, S., Hessel, V., Lin, L., Meskers, S., & Gallucci, F. (2019). Synthesis of luminescent carbon quantum dots by microplasma process. *Chemical Engineering and Processing-Process Intensification*, *140*, 29-35.

[274] Rahmanian, O., Dinari, M., & Abdolmaleki, M. K. (2018). Carbon quantum dots/layered double hydroxide hybrid for fast and efficient decontamination of Cd (II): The adsorption kinetics and isotherms. *Applied Surface Science*, *428*, 272-279.

[275] Zheng, X., Wang, K., Huang, Z., Liu, Y., Wen, J., & Peng, H. (2019). MgO nanosheets with N-doped carbon coating for the efficient visible-light photocatalysis. *Journal of Industrial and Engineering Chemistry*, *76*, 288-295

[276] Singh, N., Jana, S., Singh, G. P., & Dey, R. K. (2020). Graphene-supported TiO 2: study of promotion of charge carrier in photocatalytic water splitting and methylene blue dye degradation. *Advanced Composites and Hybrid Materials*, *3*(1), 127-140.